Technische Universität München
Fakultät für Physik

Abschlussarbeit im Masterstudiengang Physik

Analysis of the $\pi^-\pi^0\omega(782)$ Final State in COMPASS Data

Philipp Haas

17. September 2021

Abstract

The search for so-called exotic mesons, which do not fit the simple $q\bar{q}$ picture, is a major goal of meson spectroscopy. The $\pi\pi\omega$ final state is a promising channel to search for light exotic mesons, in particular these with spin-exotic quantum numbers of spin, parity, and charge conjugation $J^{PC} = 1^{-+}$ that are forbidden for $q\bar{q}$ states. In this thesis, an event selection for the $\pi\pi\omega$ final state in COMPASS data is developed. At COMPASS, light mesons are produced by diffractive scattering of hadron beams with a momentum of 190 GeV/c off a liquid-hydrogen target. We select events that correspond to the process $\pi^- + p \to \pi^-\pi^0\omega(782) + p$. The $\omega(782)$ is reconstructed via its decay into $\pi^-\pi^0\pi^+$ and the two π^0 are reconstructed by their decay into $\gamma\gamma$. The detection threshold for photons in the electromagnetic calorimeters is optimised to maximise the statistical significance of the π^0 and $\omega(782)$ peaks. This is the first event selection of $\pi\pi\omega$ analyzing the full COMPASS data. Compared to previous experiments, the selected sample of 730 000 events constitutes the by far largest $\pi\pi\omega$ sample to date. Studying the kinematic distributions, we find strong interference effects between different intermediate states. Disentangling these will require a partial-wave analysis. In addition, a Monte Carlo study of the detector acceptance and resolutions is performed using phase-space events. The event selection and the phase-space acceptance both presented in this thesis are the input required for a first partial-wave analysis of the $\pi\pi\omega$ final state of COMPASS.

Zusammenfassung

Die Suche nach sogenannten exotischen Mesonen, welche nicht in das einfache $q\bar{q}$ Bild passen, ist eines der Hauptziele der Mesonen-Spektroskopie. Der $\pi\pi\omega$ Endzustand ist ein vielversprechender Kanal um exotische Mesonen mit spin-exotischen Quantenzahlen Spin, Parität und Ladungskonjugation $J^{PC} = 1^{-+}$, welche für einen $q\bar{q}$ Zustand verboten sind, zu suchen. In dieser Arbeit wird eine Event-Selektion des $\pi\pi\omega$ Endzustands in COMPASS-Daten entwickelt. In COMPASS werden leichte Mesonen durch diffraktive Streuung von Hadronen-Stahlen mit einem Impuls von 190 GeV/c an einem Ziel aus flüssigem Wasserstoff hergestellt. Die Event-Selektion selektriert Events, die dem Prozess $\pi^- + p \rightarrow \pi^-\pi^0\omega(782) + p$ entsprechen. Das $\omega(782)$ wird über seinen Zerfall in $\pi^-\pi^0\pi^+$ rekonstruiert und zwei π^0 werden über ihren Zerfall in $\gamma\gamma$ rekonstruiert. Die Schwelle zur Detektion von Photonen in den elektromagnetischen Kalorimetern wird optimiert um die statistische Signifikanz des π^0 und des $\omega(782)$ Peaks zu maximieren. Dies ist die erste Event-Selektion von $\pi\pi\omega$, welche die kompletten COMPASS Daten enthält. Im Vergleich zu vorherigen Experimenten ist der selektrierte Datensatz mit 730 000 Events der bisher mit Abstand größte $\pi\pi\omega$ Datensatz. Eine Studie der kinematischen Distributionen zeigt starke Inteferenzeffekte zwischen verschienenden Zwischenzuständen auf. Zur Bestimmung der beitragenden Zustände ist eine Partialwellen-Analyse notwendig. Desweiteren wird eine Monte Carlo Untersuchung der Akzeptanz und der Auflösung des Detektors mit Hilfe von Phasenraum-Events durchgeführt. Mit der Event-Selektion und der Phasenraum-Akzeptanz, welche in dieser Arbeit präsentiert wurden, ist eine erste Partialwellen-Analyse des $\pi\pi\omega$ Endzustands in COMPASS möglich.

Contents

Chapter 1

Introduction

Hadrons are composited objects. They consist of quarks bound by gluons, which are the force carriers of the strong interaction. Hadron spectroscopy investigates the excitation spectrum of hadrons in order to better understand the strong interaction at low energies. This follows a similar approach as studying atomic spectra, which has contributed significantly to our understanding of the electromagnetic interaction. In hadron spectroscopy, we measure the masses, widths and decay modes of hadrons in order to gain insight into their interior structure. Due to the phenomenon of color confinement, all hadrons are singlets w.r.t. the color charge of the strong interaction. Hadrons are categorized into two types. Mesons are all hadrons with an integer spin and are therefore bosons. Baryons are all hadrons with odd half-integer spin and are therefore fermions. In the well-established constituent quark model [1, 2], mesons are described as $q\bar{q}$ pairs, whereas baryons are described as qqq states. In the standard model of particle physics, the strong interaction is described by quantum chromodynamics (QCD) [3]. QCD in principle allows further color-singlet states beyond those of the constituent quark model. These so-called "exotic" states may contain additional quarks and gluons that contribute to the total quantum numbers of the state.

Mesons are the simplest states of QCD and therefore attractive for searching for states beyond the quark model. Mesons are further differentiated into light mesons containing only u, d, and s quarks and heavy mesons containing at least one c or b quark. In particular, investigating heavy quarkonium states, i.e. states consisting of a heavy quark and its antiquark ($c\bar{c}$, $b\bar{b}$), provided evidence for the existence of exotic 4-quark mesons, such as the recently discovered state with $cc\bar{c}\bar{c}$ minimal quark content [4]. The large widths of resonances compared to their mass differences in the light meson sector lead to interference effects complicating light-meson spectroscopy. Therefore, despite its long history, the study of the light-meson spectrum is still an active field of research with many open questions. The light-meson spectrum gives insights into the characteristics of QCD at low energy, a regime where QCD cannot be solved using perturbation theory. The only first-principle approaches are numerical

simulations using lattice QCD [5, 6] and effective theories such as the chiral perturbation theory [7], which both currently have limitations.

Exotic mesons come in three types: flavour-exotic, spin-exotic, and crypto-exotic. Flavour-exotic mesons have flavour quantum numbers, such as $|I_3|$ or $|S| > 1$, that are not achievable for $q\bar{q}$ states. In the light-meson sector, there is no evidence for such states. Spin-exotic mesons have a combination of quantum numbers J^{PC} prohibited for $q\bar{q}$, where $J = 0, 1, 2...$ is the meson spin, which emerges from the coupling of the total intrinsic spin $S = 0, 1$ of the $q\bar{q}$ pair with the relative orbital angular momentum $L = 0, 1, 2...$ between the quark and the antiquark. The intrinsic parity $P = \pm 1$ of the meson describes the symmetry of the $q\bar{q}$ wave function under space inversion. Due to the opposite intrinsic parities of q and $\bar{q}$, a $q\bar{q}$ system has $P = (-1)^{L+1}$, where the $(-1)^L$ factor is the parity of a state with orbital angular momentum L. The charge conjugation parity $C = \pm 1$ specifies the symmetry of the wave function under the exchange of quark and antiquark. In case of a $q\bar{q}$ system, this is identical to flipping the sign of all spatial coordinates and inverting the spin wave function. Since the latter gives a factor of $(-1)^S$ for a quark-antiquark system, $C = (-1)^{L+S}$ for such a system. Since C is only a good quantum number in case of neutral states, G-parity is defined as a generalisation of the C-parity under which not only neutral mesons but the whole isospin triplet for non-strange light mesons is an eigenstate. It is defined as a 180° rotation of the charge conjugated state about the y-axis in isospin space. Hence, $G = C(-1)^I$. A common convention is assigning the C quantum number of a neutral state to its charged isospin partners. From the above, it is clear that quark-antiquark systems cannot have the quantum numbers

$$J^{PC} = 0^{--}, 0^{+-}, 1^{-+}, 2^{+-}, 3^{-+}... \quad .$$

Crypto-exotic mesons are states that have quantum numbers of ordinary $q\bar{q}$ states, but an exotic internal structure. Hence, these states cannot be distinguished from $q\bar{q}$ by studying their quantum numbers. Crypto-exotic mesons are expected to appear as supernumerous states in the spectrum since they are not part of the $q\bar{q}$ $\mathrm{SU}(3)_{\mathrm{flavor}}$ nonet and therefore increase the state density within a given J^{PC} sector. Depending on their internal structure, they may also be distinguishable from ordinary $q\bar{q}$ states via their decay pattern.

The COMPASS experiment collected large data samples that allow us to study the light-meson spectrum in great detail. To produce excited mesonic resonances a 190 GeV π^- beam is scattered diffractively off a proton target. In this process, the target proton stays intact and the beam π^- is excited to some resonance X^- via the exchange of a Regge trajectory [8], the Pomeron, as shown in Fig. 1.1. This process allows for a large variety of resonances to be produced, which is limited only by conservation laws of the strong interaction. This means the produced X^- must have isospin $I = 1$ and $G = -1$ parity as the beam π^-. Thus, the X^- are either π_J or a_J-like mesons with spin J.

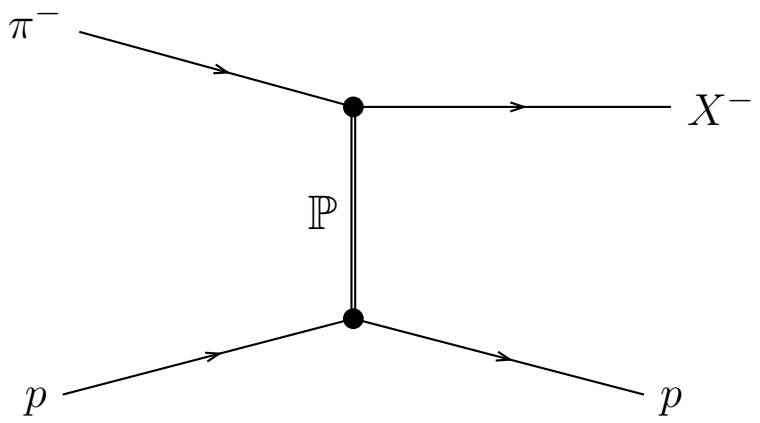

Figure 1.1: Diffractive production of exited mesons by Pomeron exchange.

Lattice QCD predicts the lightest spin-exotic meson to have $J^{PC} = 1^{-+}$ and to be a so-called hybrid meson [9], i.e. a meson where in addition to $q\bar{q}$ also excited gluonic fields contribute to the total quantum numbers. The mass itself cannot be predicted due to computational limits which allow only unphysical pion masses m_π around $400\,\mathrm{MeV}/c^2$. Previous experiments claimed observation of the resonances $\pi_1(1400)$, $\pi_1(1600)$, and $\pi_1(2015)$ in this J^{PC} sector [10, 11, 12]. Analyses based on COMPASS data in the $\pi^-\pi^-\pi^+$ [13], $\eta\pi^-$, and $\eta'\pi^-$ [14] decay channels have confirmed the $\pi_1(1600)$ state and suggested that the $\pi_1(1400)$ claimed by previous experiments is actually the same state [15]. The limitation of stable particles in lattice QCD simulations was overcome to also predict the partial decay widths for different decay channels for the $\pi_1(1600)$ [16]. Fig. 1.2 shows the predicted partical decay widths, where the width for the $b_1(1235)\pi$ decay is dominant and an order of magnitude larger than all other decay channels. Since $b_1(1235)$ decays predominantly to $\omega\pi$, this motivates to analyze the $\omega\pi\pi$ decay channel using data recorded by the COMPASS experiment. Another motivation is the partial-wave analysis of $\omega\pi\pi$ performed by the BNL E852 experiment, which reported the $\pi_1(1600)$ and claimed the excited $\pi_1(2015)$ [12]. An additional benefit of this channel compared to $\pi\pi\pi$ and $\eta^{(\prime)}\pi$ is the access to higher masses because of the higher kinematic threshold. A first study of the reaction $\pi^- + p \to \pi^-\pi^0\omega(782) + p$ using a subset of COMPASS data was performed by M. Ebert in Ref. [17]. The event selection presented here is an extension of the work of C. Dreisbach [18] and exploits the full COMPASS data set. Furthermore, the angular phase-space acceptances for the $\omega\pi\pi$ channel are studied. Therefore, this thesis aims to provide all prerequisites necessary to perform a partial-wave analysis in order to extract $\omega\pi\pi$ resonances.

This thesis is structured in the following way: Chapter 2 explains the experimental setup. Chapter 3 describes the procedure used to select $\pi^- + p \to \pi^-\pi^0\omega + p$ events. The $\omega(782)$ is reconstructed from its decay into $\pi^-\pi^0\pi^+$. The two π^0 particles are reconstructed from four photons candidates. Chapter 4

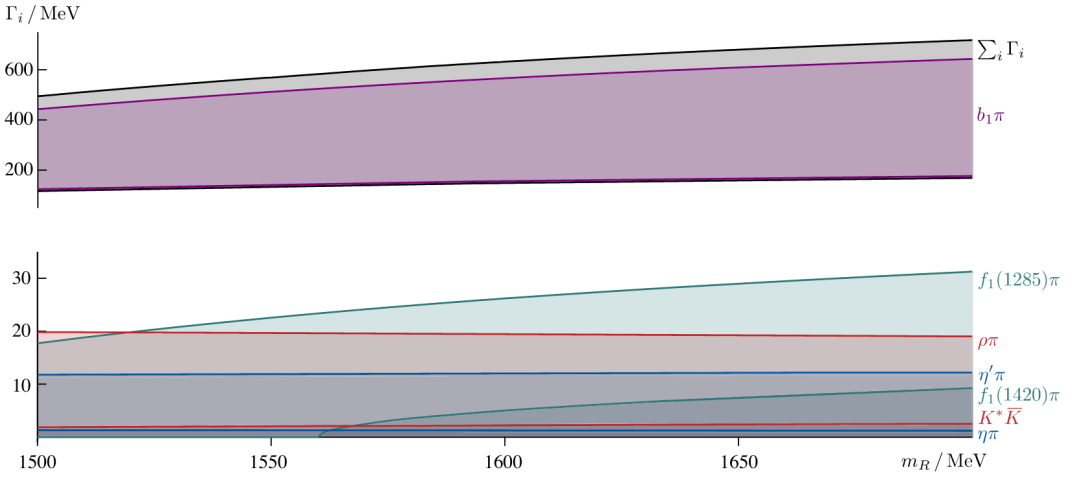

Figure 1.2: Partial widths of the π_1 depending on its mass as predicted by lattice QCD [16].

discusses the properties of the selected data sample and compares it to the sample recorded by the BNL E852 experiment. In this chapter, we also study some angular distributions in the $\pi\pi\omega$ system and the kinematics within the $\omega(782)$ subsystem. Chapter 5 explains the Monte Carlo simulations performed to study the resolutions and acceptances of the detector system. In Chapter 6, we conclude and give an outlook.

Chapter 2

The COMPASS Experiment

The COmmon Muon and Proton Apparatus for Structure and Spectroscopy (COMPASS) experiment is a fixed-target experiment located at the North Area of CERN. The physics program addresses a wide range of open questions in the field of hadron physics. During 2008 and 2009, the data-taking campaign included scattering of a negative hadron beam with a momentum of 190 GeV/c off a liquid-hydrogen target.

2.1 M2 Beam Line

To produce hadron beams for the COMPASS experiment, a proton beam with a momentum of 400 GeV/c coming from the Super Proton Synchrotron (SPS) is guided onto the primary production target T6. Scattering of the protons off this 500 mm long beryllium target produces a secondary hadron beam with a nominal intensity of $5 \cdot 10^6\,\mathrm{s}^{-1}$. Six quadrupoles and three dipoles in the M2 beam line select a momentum band of ±10% around the nominal beam momentum of about 190 GeV/c. When the beam reaches the COMPASS target, it is composed of 96.8% π^-, 2.4% K^- and 0.8% $\bar{p}$. Two CEDAR detectors that are installed 30 m upstream of the COMPASS target identify the species of the beam particle using the Cherenkov effect. Charges moving faster than light in a medium with refractive index n emit Cherenkov radiation [19] under a Cherenkov angle

$$\theta_{\mathrm{Ch}} = \arccos\frac{1}{n\,\beta} = \arccos\frac{\sqrt{p^2c^2 + m^2c^4}}{p\,n\,c} \tag{2.1}$$

with respect to the particle's trajectory. Here, c is the speed of light in vacuum and $\beta > 1/n$ is the velocity in units of c, p the momentum, and m the rest mass of the charged particle. Due to different masses of the particle species, θ_{Ch} depends on the species. The CEDARs measure the Cherenkov angle to determine the species of beam particles with momenta of up to 300 GeV/c.

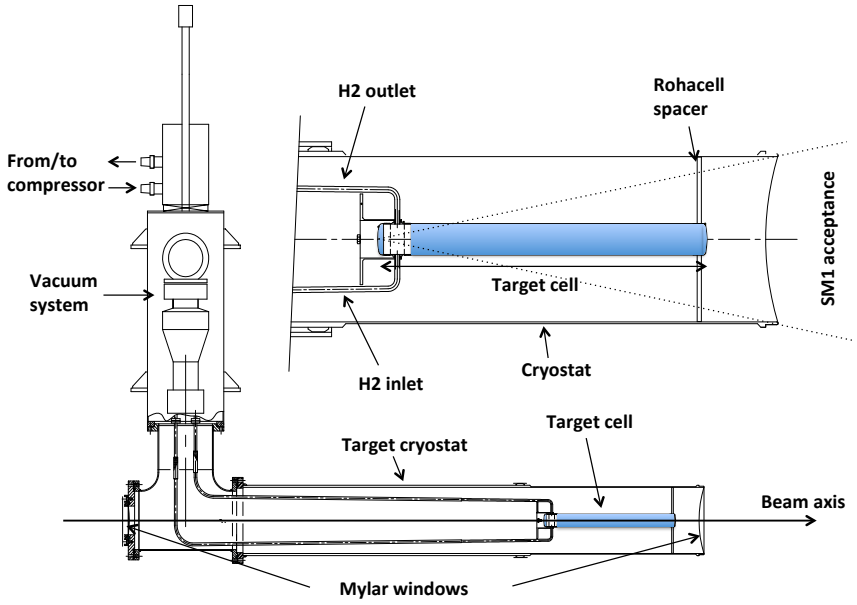

Figure 2.1: Side view on the liquid-hydrogen target system [20].

2.2 Target System

During the 2008 and 2009 hadron-beam data taking either a liquid-hydrogen target or targets made of solid materials (Pb, W, and Ni) were used. For liquid hydrogen, the target shown in Fig. 2.1 has a cylindrical shape with a diameter of 35 mm and a length of 400 mm. The target cylinder is made of Mylar with a wall thickness of 125 μm. A cryostat installed around the target cools the target. It consists of an aluminum tube with a diameter of 185 mm and a wall thickness of 1.8 mm and two Mylar windows with a thickness of 250 μm. The support pipes for the cryostat consist of stainless steal. The cooling liquid is liquid helium.

The Recoil Proton Detector (RPD) detects recoiled protons originating from the target. The detector consists of two scintillator barrels around the target, so-called "rings". The inner ring has a radius of 12 cm and consists of 12 scintillator slabs, i.e. each slap covers an angular range of 30°. The outer ring has a radius of 75 cm and consists of 24 scintillator slabs, where one slab is completely covered by a single inner-ring slab, while the neighboring two outer slabs are each covered by two inner-ring slabs. By measuring the time of flight the momentum of the recoil proton is determined. Background from other particle species is discriminated from protons based on the energy loss. Furthermore, the RPD is part of the trigger system used to trigger for physical events.

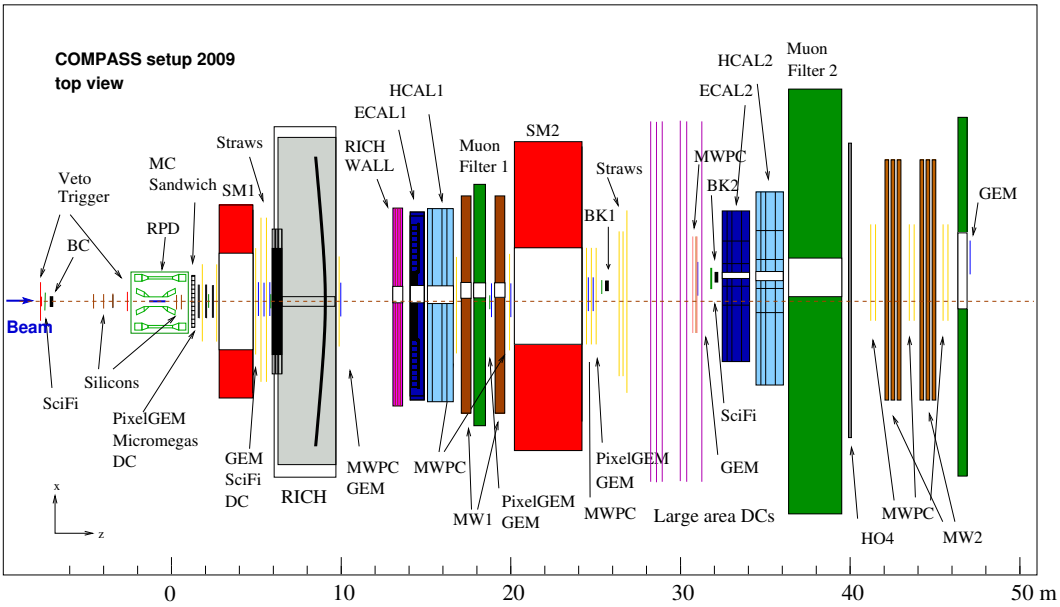

Figure 2.2: COMPASS setup for data taking with hadron beams in 2008 and 2009 [20].

2.3 Tracking Detectors

The momenta of charged particles are measured by a two-stage magnetic spectrometer using two dipole magnets, SM1 with a bending power of about 1 Tm followed by SM2 with a bending power of about 4 Tm (see Fig. 2.2). Several detectors using various technologies track the produced particles that leave the target in forward direction. Scintillating Fiber, Silicon Microstrips, and PixelGEM detectors cover the inner-most region closest to the beam axis. This so-called very-small-angle region reaches up to a radial distance of 2.5 cm–3.0 cm with respect to the beam axis. These detectors can cope with the high rates of incoming particles up to $5 \cdot 10^5\,\mathrm{cm}^{-2}\mathrm{s}^{-1}$. Micromegas and GEM detectors cover the intermediate area, the so-called small angle region, reaching from radial distances of 2.5 cm to 30 cm–40 cm. These detectors can cope with a hit rate of up to $10^4\,\mathrm{cm}^{-2}\mathrm{s}^{-1}$. The outermost detectors, also called large-angle detectors, have to endure lower hit rates and therefore drift chambers, straw tube chambers, and multiwire proportional chambers cover this area.

In order to determine the position of the interaction point precisely, three Silicon Microstrip detectors upstream of the target measure the exact direction of the beam, while two Silicon Microstrip detectors downstream give additional information on the reaction products in forward direction.

2.4 Particle-Identification Detectors

Several detectors placed downstream of the target help to identify the species of particles produced in the collisions. After traversing the tracking detectors and the first dipole magnet SM1, the particles pass the Ring-Imgaging Cherenkov detector RICH-1. It measures the Cherenkov angle (see Eq. (2.1)) to determine the species of the charged particles such as pion, kaon, proton, and electron. The inner region of the RICH consists of Multi-Anode PhotoMultiplier Tubes (PMTs). Multiwire Proportional Chambers with solid-state CsI photocathodes cover the outer region where lower rates of background contribute.

Each of the two spectrometer stages is equipped with an Electromagnetic CALorimeter (ECAL) to measure the energies of electrons and photons, a Hadron CALorimeter (HCAL) to measure the energies of hadrons, and a muon identification system consisting of a muon filter, i.e. an absorber for electrons, photons and hadrons, and a detector to identify muons.

Electromagnetic calorimeters measure the energy of electrons and photons by completely absorbing them. At energies above 1 GeV electrons lose energy predominantely via bremsstrahlung and photons via e^+e^- pair production [21]. For both particle species, the energy loss is approximately proportional to the inverse of the radiation length X_0. The radiation length is a material property describing a distance over which an traversing electron loses in average all but $1/e$ of its initial energy. Since for high atomic numbers Z $1/X_0 \sim Z^2$ as a rough approximation [22], materials with high atomic numbers are well suited as absorbers for electrons and photons. In addition, such materials tend to have a high density and therefore require little volume for total absorption.

Bremsstrahlung and pair production produce secondary photons and electrons. If the energy of the initial particle is large enough the secondary photons and electrons are also high-energetic and undergo pair production and bremsstrahlung, respectively. This leads to a cascade of interactions resulting in an electromagnetic shower. Electromagnetic calorimeter come in two types. The first type are homogeneous calorimeter. They consist of a single material that both produces the showers and converts the showers into a measurable signal. The second type are sampling calorimeters. They consist of passive and active material. The passive medium produces the showers; the active generates a signal.

Each ECAL consists of a matrix of multiple modules. The energy is calibrated with an electron beam. Each module collects several thousand electron hits multiple times within a run to ensure calibrated modules with no time-dependent energy measurements. Incoming photons and electrons produce hits in several modules due to showering. Hits in neighboring modules

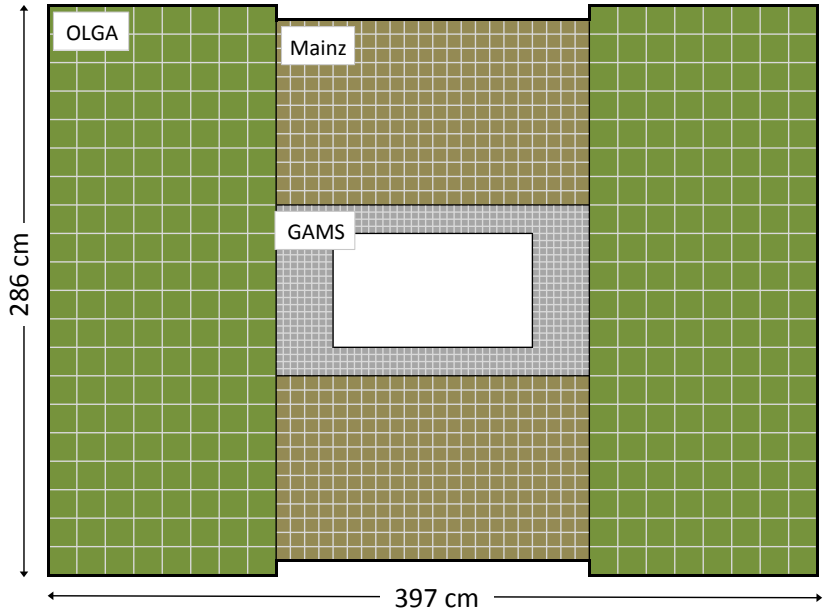

Figure 2.3: Front view of the electromagnetic calorimeter ECAL1 [20]. The labels indicate the different module types.

are grouped into so-called clusters to reconstruct the total energy deposited by the particle.

2.4.1 Electromagnetic Calorimeter 1

ECAL1 is part of the large-angle spectrometer and is made of 1500 modules of three different types. Fig. 2.3 shows the arrangement of the modules. The angular coverage from the center of the target is 37 mrad to 98 mrad horizontally and 21 mrad to 98 mrad vertically. The central hole fits the geometrical acceptance of the second spectrometer stage. All modules are of the homogeneous type and are made of lead glass, i.e. a mixture of PbO and SiO_2. The electromagnetic showers emit Cherenkov photons while traversing the lead glass. One PMT in each module measures the Cherenkov radiation. The obtained signal is then digitized by a sampling analog-to-digital converter (SADC) with a frequency of 80 MHz.

The innermost part consists of a 44×24 matrix of "GAMS" modules with a 28×16 hole in the center. Each GAMS module covers a surface of $3.83 \times 3.83\,\mathrm{cm}^2$ perpendicular to the nominal beam direction and has a thickness of $16.4\,X_0$. Two 22×13 matrices of "MAINZ" modules cover the regions above and below this innermost region. MAINZ modules have a $7.5 \times 7.5\,\mathrm{cm}^2$ surface and a thickness of $23.3\,X_0$. As 2×2 GAMS modules cover more than one MAINZ module, the MAINZ modules are arranged with 1.6 mm vertical gaps. The two gaps closest to the center are filled with iron plates. This prevents

particles from traversing without interaction. The two outermost regions left and right of ECAL1 consist each of a 8×20 matrix of $14.1 \times 14.1\,\mathrm{cm}^2$ "OLGA" modules. The OLGA modules have a total thickness of $18.5\,X_0$.

2.4.2 Electromagnetic Calorimeter 2

ECAL2 measures particles that are produced with small angles. It consists of 3068 modules as shown in Fig. 2.4. Each module has a size of $3.83 \times 3.83\,\mathrm{cm}^2$. The whole ECAL2 covers an area of $2.44 \times 1.83\,\mathrm{m}^2$ corresponding to an angular range up to 39 mrad in horizontal and up to 29 mrad in vertical direction. Therefore, shadows of ECAL1 and HCAL1 cover parts of ECAL2. The innermost part of ECAL2 consits of 888 "Shashlik" modules. In contrast to all other modules, the Shashlik modules are of the sampling type. They consist of 0.8 mm thick passive lead plates and 1.55 mm thick active scintillator plates which measure the energy. Each module consists of 154 alternating layers of both materials. Wavelength-shifting fibers collect the photons produced in the scintillators and guide them to a PMT at the downstream end of the module. Near the center with a horizontal offset and a size of 2×2, a hole in the Shashlik matrix lets non-interacting beam particles pass. The offset with respect to the center is due to the bending of the beam in the magnetic fields of the two bending magnets. The intermediate region of ECAL2 is covered by 848 radiation-hardened versions of the GAMS modules (GAMS-R) and 1332 GAMS modules cover the outermost region. The GAMS modules are the same as the one used in ECAL1. Sampling ADCs digitize the signal of all PMTs in ECAL2 at a frequency of 80 MHz.

2.5 Trigger System

The trigger system used for the data taking with hadron beams focuses on three goals. It ensures that the event has an incoming beam particle, it vetos events with particles outside the acceptance of the spectrometer and it selects specific signatures of the physics processes of interest. For diffractive scattering, the diffractive trigger (DT0) requires a recoil proton. Fig. 2.5 shows an overview of the trigger elements.

A scintillating fiber detector (SciFi1) and the beam counter detect the incoming beam 7 m and 6.5 m, respectively, upstream of the target. The SciFi1 consists of one vertical and one horizontal plane, each read out by six multi-anode PMTs. The beam counter is a scintillator disk with a diameter of 3.2 cm and a thickness of 4 mm connected to one PMT. The beam trigger requires coincidence of the beam counter and the SciFi1. Its time resolution is 450 ± 50 ps.

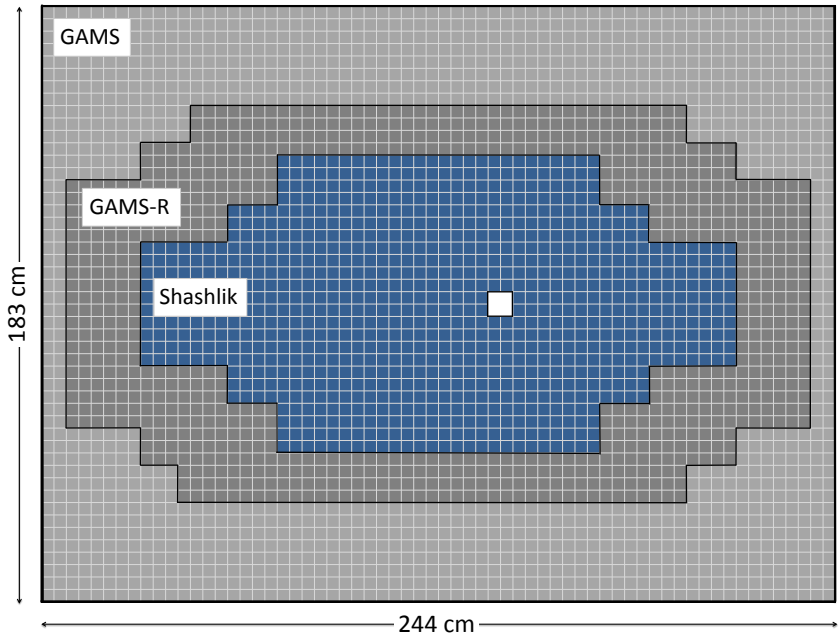

Figure 2.4: Front view of the electromagnetic calorimeter ECAL2 [20]. The labels indicate the different module types.

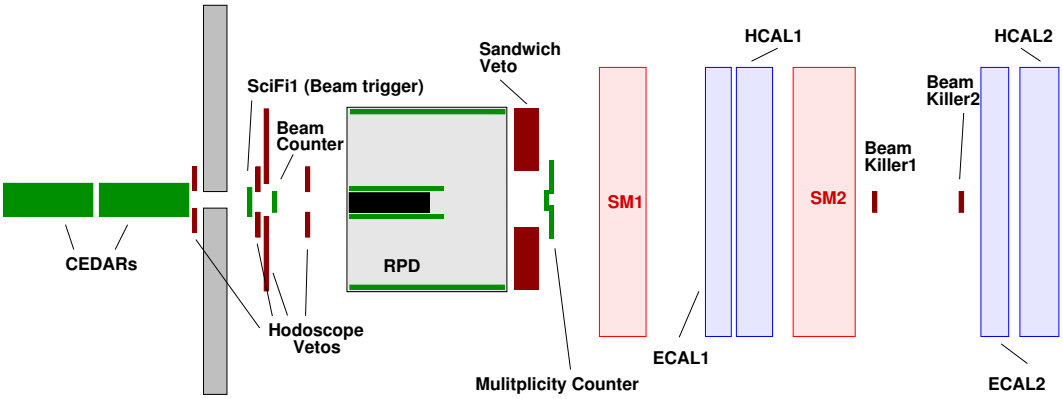

Figure 2.5: Schematic setup of the trigger system of COMPASS [20].

The second part of the trigger system for diffractive processes is the recoil-proton trigger. It uses information from the RPD (see Section 2.2) to select events with a recoiled proton. Only events where a hit in an outer slabs follows a hit of the corresponding inner slab pass it which is shown in Fig. 2.6. The hit slabs must be consistent with a straight particle trajectory coming from the primary vertex and intersecting both slabs. Based on the energy losses in both rings the RPD discriminates traversing electrons and pions from protons and removes them.

A veto trigger rejects events from unwanted background processes. The veto system consists of the sandwich veto detector, the hodoscope veto system, and two beam killers. The beam killers are two scintillating disks installed in front of ECAL2. They have a diameter of 3.5 cm and a thickness of 0.5 cm.

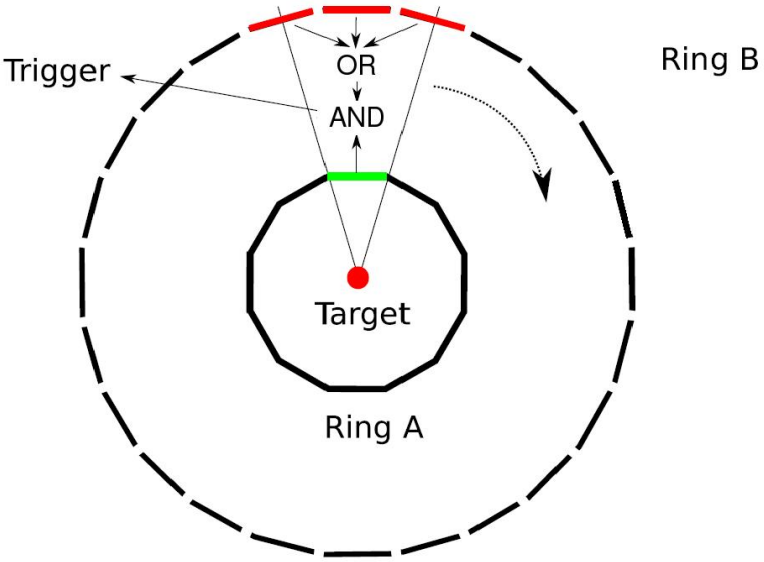

Figure 2.6: Trigger logic for the proton trigger [20].

They are centered at the nominal beam axis and detect non-interacting beam particles up to an angular distance of 0.97 mrad. The sandwich veto detector is located behind the RPD and triggers on particles that are outside the angular acceptance of the spectrometer. It consists of five layers of steel-covered lead plates and scintillators with a dimension of $2 \times 2\,\mathrm{m}^2$ and a central hole matching the acceptance of the spectrometer. The hodoscope trigger system consists of three detectors. The beam-line hodoscope installed 20 m upstream of the target removes diverging beam particles. The other two detectors, Veto1 and Veto2, are positioned 7.5 m and 1.5 m, respectively, upstream of the target. For diffractive processes the recoiled proton is nearly perpendicular to the beam axis and the outgoing particles are boosted in the direction of the beam axis. Therefore, no particles are expected in the intermediate region. Events with particles within this so-called rapidity gap are non-diffractive and originate from excited target states and other background processes and are therefore removed.

Chapter 3

Event Selection

The analysis presented is based on data recorded by the COMPASS experiment using a π^- beam impinging on a liquid-hydrogen target at an energy of about 190 GeV. The data were taken in 2008 and 2009. The process of interest,

$$\pi^- + p \to \pi^-\pi^0\omega(782) + p, \tag{3.1}$$

is shown in Fig. 3.1. The $\omega(782)$ is reconstructed via its decay into $\pi^-\pi^+\pi^0$ resulting in a 5π final state. The two final-state π^0 are reconstructed via their decay into $\gamma\gamma$. Therefore, the actually measured reaction is

$$\pi^- + p \to \pi^-\pi^-\pi^+ + 4\gamma + p. \tag{3.2}$$

Due to diffractive scattering the outgoing charged pions and the four photons leave the target with a small angle. Therefore, the three charged pions are detected by the tracking detectors and the four photons deploy their energy in four ECAL clusters. The recoiled proton leaves the target almost perpendicular and is detected by the RPD.

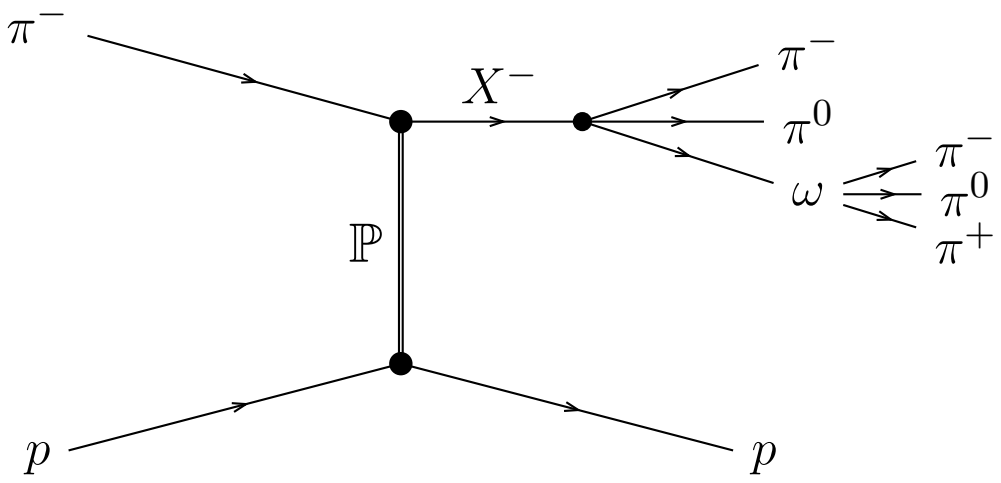

Figure 3.1: Diffractive production of $\pi^-\pi^0\omega$ at COMPASS.

Table 3.1: List of cuts applied in the preselection stage. The second and third columns show the number of events passing the given cut for 2008 and 2009, respectively.

Cut	2008	2009
Total	763 590 775	604 721 548
DT0 trigger	690 252 299	550 206 147
Exactly one primary vertex	658 645 375	519 882 071
$-260\,\text{cm} < z_{\text{vertex}} < 160\,\text{cm}$	656 472 904	518 530 230
Three charged tracks	509 553 291	391 592 431
$\sum_{i=0}^{3} Q_i = -1$	505 674 189	387 842 643
At least one RPD track	453 669 462	342 810 672
> 4 ECAL clusters	307 492 130	247 231 722

The event selection is performed in two stages. The first stage discussed in Section 3.1 preselects events using loose cuts. In the second stage, discussed in Sections 3.2 to 3.9, tighter cuts select candidate events for the signature in Eq. (3.1). Section 3.10 summarises the event selection. Unless stated otherwise, all plots shown in this Chapter show the data with all selection cuts, i.e. those listed in Tables 3.1 and 3.13, applied except for cuts on the variables shown in the plots. All plots show the data of 2008 and 2009 combined except stated otherwise.

3.1 Preselection

Due to the size of the data set recorded by COMPASS a preselection selects for generic signatures shared by several final states to decrease the amount of data processed in the selection of specific final states. The preselection used in this analysis is based on the work of S. Wallner. It searches for candidate events that correspond to the generic process

$$h^-_{\text{beam}} + p \to h^- h^- h^+ + (\geq 4\gamma) + p_{\text{recoil}}, \tag{3.3}$$

where h^-_{beam} is a negatively charged beam particle and $h^\pm$ are charged final-state particles. Table 3.1 lists all applied preselection cuts.

All selected events have to be triggered by the diffractive trigger (DT0) based on the information from the trigger system (see Section 2.5).

The point of intersection of a beam particle and outgoing charged particles is called primary vertex and represents the interaction point of the event. Candidate events must have exactly one primary vertex. The preselection

requires the primary vertex to have a position within the range from −260 cm to 160 cm along the nominal beam axis, i.e. the z-axis. Since the analyzed final state contains exactly three charged particles, only primary vertices with three charged outgoing particles will pass the selection. Furthermore, the total charge of the three particles must be −1 to fulfill charge conservation.

Events selected by the preselection must contain at least one RPD track that agrees with a proton track.

Since the final event signature contains four photons, the preselection requires at least four ECAL clusters. Clusters close to a track of a charged particle are not considered.

About $5.55 \cdot 10^8$ of the $1.37 \cdot 10^9$ recorded events pass the preselection criteria. The data taken in 2008 corresponds to around 55% of the total data set and the ones taken in 2009 account for the remaining 45%. Due to this reduction in events and a different storage format storing only information relevant for the analysis the preselection reduces the required disk space from 6.3 TB to 520 GB.

3.2 Beam Particle and Primary Vertex

To ensure the detection of the correct beam particle, the trigger signal and the beam particle must coincide. Fig. 3.2 shows the distributions of the beam time T_{beam} for both years separately. Both distributions have a peak at about 0 and are fitted with

$$\begin{aligned}\frac{dN}{dT_{\text{beam}}}(T_{\text{beam}}; A^{\text{beam}}, R^{\text{beam}}, \Delta T^{\text{beam}}, \sigma_1^{\text{beam}}, \sigma_2^{\text{beam}}) = \\ A^{\text{beam}} D_{\text{G}}(T_{\text{beam}}; R^{\text{beam}}, \Delta T^{\text{beam}}, \sigma_1^{\text{beam}}, \sigma_2^{\text{beam}}),\end{aligned} \tag{3.4}$$

where D_{G} is the double-Gaussian distribution (see Appendix B.1). The fit range is from −3 ns to 3 ns. Table 3.2 lists the relevant fit parameters. The cut requires the difference between the beam time and the trigger time to be within three times the peak's width around the peak position approximately at 0. The beam time has to be in the range from −2.27 ns to 2.32 ns and from −2.79 ns to 2.55 ns for 2008 and 2009 events, respectively.

Approximately 2.4% of the incoming beam particles are K^-. To suppress this unwanted contribution a cut on the particle identification (PID) information from the CEDAR detectors (see Section 2.1) requires a π^- as beam particle. S. Wallner established the PID method in Refs. [23, 24]. It requires the CEDAR likelihood ratio

$$R = \frac{\mathcal{L}_{\text{CEDAR}}(K^-)}{\mathcal{L}_{\text{CEDAR}}(\pi^-)} < 1 \tag{3.5}$$

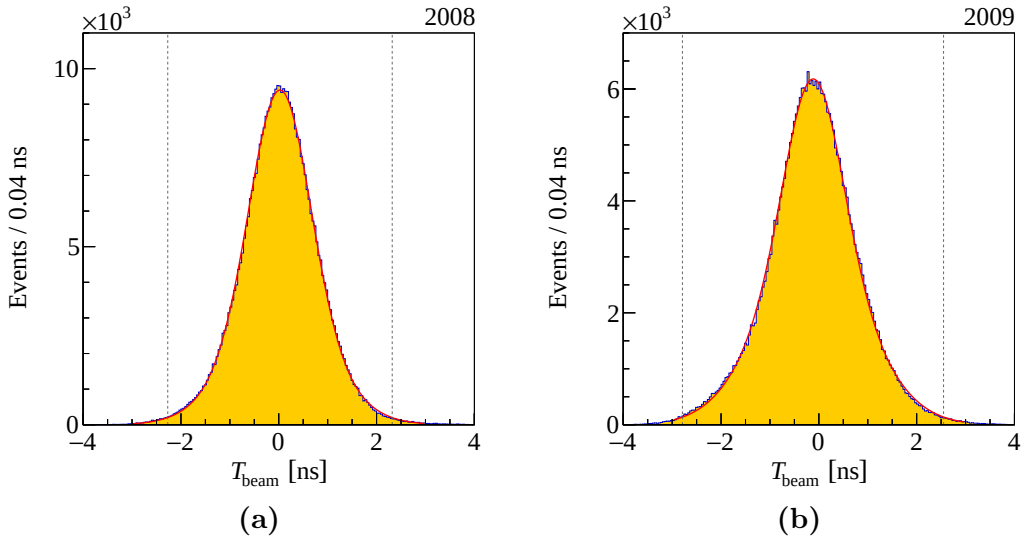

Figure 3.2: Distribution of the beam time for (a) the 2008 and (b) the 2009 data sets. The vertical lines indicate the selected intervals. The red curves show the fit of Eq. (3.4) to both distributions.

Table 3.2: Parameters obtained by fitting Eq. (3.4) to the T_{beam} distribution in Fig. 3.2.

Parameters		2008	2009
R^{beam}		0.417	0.619
ΔT^{beam}	[ns]	0.024	−0.116
σ_1^{beam}	[ns]	0.994	1.082
σ_2^{beam}	[ns]	0.602	0.580
χ^2_{red} (NDF)		2.7 (145)	2.8 (145)
σ^{beam}	[ns]	0.765	0.891

to identify a π^- as beam particle. Here $\mathcal{L}_{\text{CEDAR}}(S)$ is the CEDAR likelihood of the beam particle to be of species S.

We require the primary vertex to lie within the cylindrical volume of the liquid-hydrogen target. This means, the z-position of the vertex must be from −66 cm to −29 cm and the radial distance R_{vertex} from the z-axis must be smaller than 1.55 cm. Fig. 3.3 shows the distribution of both observables. The distribution of z_{vertex} is not uniform. Particles produced near the upstream end of the target are more likely to scatter within the target leading to a lower acceptance. Therefore, the distribution has a slope for increasing z_{vertex}. The

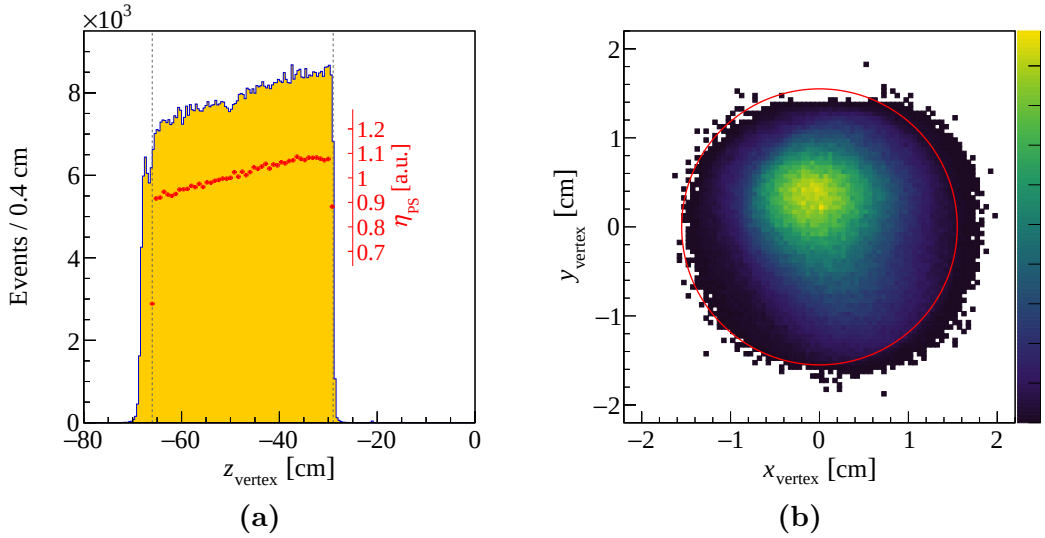

Figure 3.3: Distribution of (a) the z-position and (b) the radial position of the primary vertex from the beam axis. The vertical lines in (a) and the circle in (b) indicate the selected regions. The red distribution in (a) shows the relative acceptance η_{PS} (see Section 5.2).

phase-space acceptance η_{PS}[a] (red points) shows similar features. The dip around $z_{\mathrm{vertex}} = 50\,\mathrm{cm}$ occurs due to laser connectors used for calibrating the RPD. Since these connectors are not simulated, the effect is not visible in η_{PS}. The distribution of xy of the vertex shows the convolution of the distribution of liquid hydrogen within the target and the beam distribution. The target is not completely filled with liquid hydrogen which leads to a lack of events at high y-positions. The asymmetry of the xy-distribution is due to the spread of the incoming beam.

3.3 Final-State Kaon Veto

Fig. 3.4a shows the Cherenkov angle θ_{Ch} measured by the RICH-1 detector against the magnitude p_{particle} of the particle's momentum for all charged particles in the selected events. Due to the different masses of the particle species they have different velocities for a given momentum and will hence accumulate along bands given by Eq. (2.1). The white dashed lines illustrate the expected locations of the bands for pions, kaons, protons, and $e^{\pm}$. As expected

[a] To estimate the acceptance based on simulation we generate five pions in phase-space without simulating the $\omega(782)$ resonance (see Chapter 5) and do not simulate the $X \to \pi\pi\omega \to 5\pi$ decay. Therefore, this simulation is unable to estimate the absolute acceptance of the detector for the $\pi^-\pi^0\omega$ channel but it gives access to study the relative acceptance η_{PS} of the spectrometer for the kinematics of the 5π final state. This allows us to study uniformity of acceptance in kinematic variables.

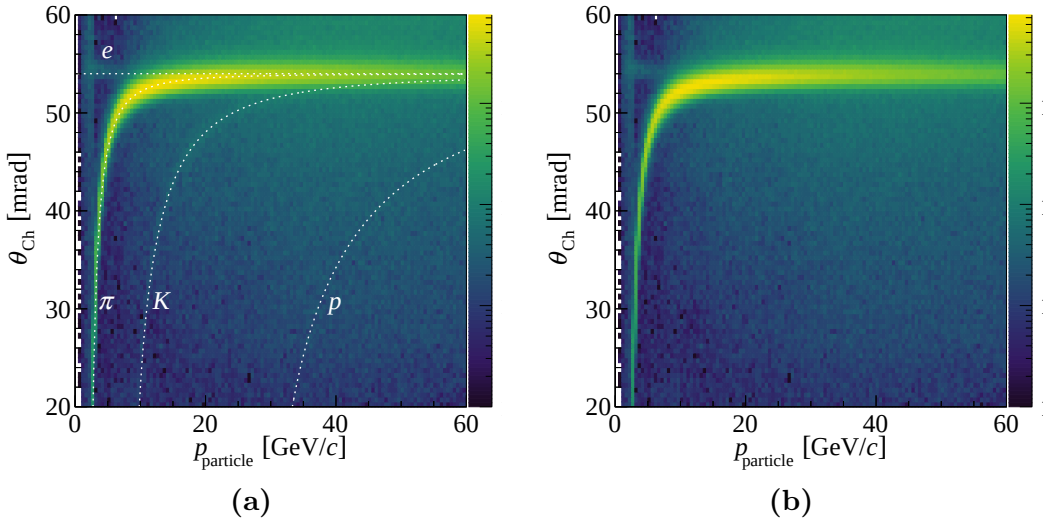

Figure 3.4: Distribution of the Cherenkov angle against the momentum for all charged particles (a) before and (b) after applying the kaon veto. The dashed white lines in (a) indicate the predicted behavior for the labeled particle species. Note the logarithmic color scale.

before PID, the by far largest contribution comes from pions but also small contaminations by kaons and $e^{\pm}$ contribute to the dataset, while the plot shows no noteworthy contamination by protons. To remove the kaon background a veto is applied based on the RICH likelihoods of pions, kaons, protons, and background. The method was introduced by S. Wallner in Appendix B.2 of Ref. [25]. If the RICH likelihood ratio

$$\mathcal{R} = \frac{\mathcal{L}_{\mathrm{RICH}}(K)}{\max\limits_{S\in\{\pi,p,\mathrm{BG}\}} \mathcal{L}_{\mathrm{RICH}}(S)} \tag{3.6}$$

of a charged particle is greater than 1.15 the particle is identified as kaon. Here $\mathcal{L}_{\mathrm{RICH}}(S)$ is the RICH likelihood of a particle to be of species S. The PID is only possible within a range of p_{particle} for each species. To calculate the likelihood of a pion the magnitude of its momentum is required to be within the range from 3 GeV/c to 60 GeV/c; for kaons within 10 GeV/c to 60 GeV/c; and for protons within 18 GeV/c to 100 GeV/c. If at least one of the charged particles is identified as kaon, the event is discarded. Fig. 3.4b shows the distribution of Cherenkov angle vs. momentum after applying this kaon veto. No significant kaon contribution is visible after the cut. In principle, a similar veto is possible for $e^{\pm}$. However, such an $e^{\pm}$ veto would only be sensitive for momenta below 10 GeV/c and would therefore have a negligible effect. Therefore, no $e^{\pm}$ veto is applied.

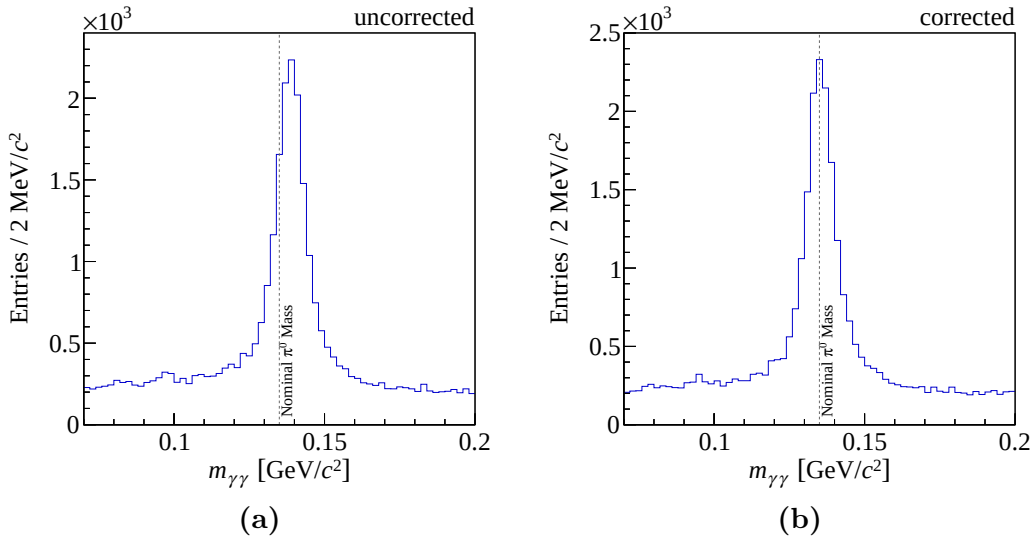

Figure 3.5: $m_{\gamma\gamma}$ distributions (a) before and (b) after the energy post-correction for events in run 69913. The vertical line indicates the nominal π^0 mass. The applied cuts are discussed in Section 3.5.

3.4 Photon Reconstruction

Photons are reconstructed based on the energy they deposited in an ECAL cluster and assuming that their direction is given by the vector from the primary vertex position to the cluster position. Despite the energy calibration with an electron beam during run time, S. Uhl found a time dependence of the π^0 peak in the invariant mass spectrum of two photons [26]. The peak is shifted to the nominal π^0 mass by applying post-correction factors to the energy. The factors are common for each ECAL and each run provided by S. Gerassimov [27]. Fig. 3.5 illustrates this post-correction based on events in run 69913. The $m_{\gamma\gamma}$ distribution before the post-correction in Fig. 3.5a peaks at masses around $4\,\mathrm{MeV}/c^2$ higher than the nominal π^0 mass. Fig. 3.5b shows the same distribution after multiplying the energies of ECAL1 and ECAL2 clusters by 0.9855 and 0.9726, respectively. Due to this post-correction the peak is shifted to the nominal π^0 mass.

During the 2008 and 2009 data taking periods HCAL1 obstructed parts of ECAL2. Hits in these regions of ECAL2 are excluded since the corresponding particles suffered a large energy loss by traversing the HCAL1. To this end, we require the y-position of clusters in ECAL2 to lie in the range from $-17 \cdot 3.83\,\mathrm{cm}$ to $16 \cdot 3.83\,\mathrm{cm}$ (see Section 4.3 in Ref. [28]).

In Sections 3.4.2 and 3.4.3 energy thresholds optimised by the method introduced in Section 3.4.1 remove low energy clusters due to large background contributions. Section 3.4.4 discusses cluster time corrections and cuts on the

cluster time to remove off-time clusters. After all requirements each event must contain exactly four γ candidates to pass the selection.

3.4.1 Cut-Parameter Optimization

For some of the cuts applied in this analysis the cut values are statistically optimized. The figure of merit for this optimization is the statistical significance of the signal, which is given by

$$\sigma_{\text{stat}} = \frac{N_{\text{S}}}{\sqrt{N_{\text{B}} + N_{\text{S}}}}. \tag{3.7}$$

Here, N_{S} and N_{B} are the number of signal and background events, respectively. To estimate N_{S} and N_{B}, either the fitted π^0 peak in the $m_{\gamma\gamma}$ spectrum described in Section 3.5, or the fitted $\omega(782)$ peak in the $m_{\pi^-\pi^0\pi^+}$ spectrum as described in Section 3.6 is considered. By varying only the investigated cut parameter, its optimal value is determined by maximizing the statistical significance.

3.4.2 ECAL1 Energy Threshold

Fig. 3.6 shows σ_{stat} (see Eq. (3.7)) for the π^0 and $\omega(782)$ peaks as well as the number of selected events as a function of the ECAL1 cluster-energy threshold for the 2008 and 2009 data sets. While the π^0 peak suggests a threshold value of 0.6 GeV, the $\omega(782)$ peak has an optimum at lower values. Since ECAL1 threshold values below 0.6 GeV lead to increased noise contamination, we set the ECAL1 threshold to 0.6 GeV. This is the same value that S. Uhl used for the $\pi^-\pi^0\pi^0$ channel (see Section 3.2.1 in Ref. [26]).

3.4.3 ECAL2 Energy Threshold

Fig. 3.7 shows σ_{stat} (see Eq. (3.7)) for the π^0 and $\omega(782)$ peaks as well as the number of selected events as a function of the ECAL2 cluster-energy threshold for the 2008 and 2009 data sets. For both years and both peaks the significance has a broad maximum starting at about 1.8 GeV and therefore the ECAL2 threshold is set to this value. This value is somewhat larger than the 1.2 GeV used by S. Uhl for the $\pi^-\pi^0\pi^0$ channel (see Section 3.2.1 in Ref. [26]).

3.4.4 Cluster Time Correction and Cluster Time Cut

The information on the cluster time is exploited using the approach developed in Section 2.4.1 in Ref. [26]. Gaussians are fitted to the cluster time distributions in

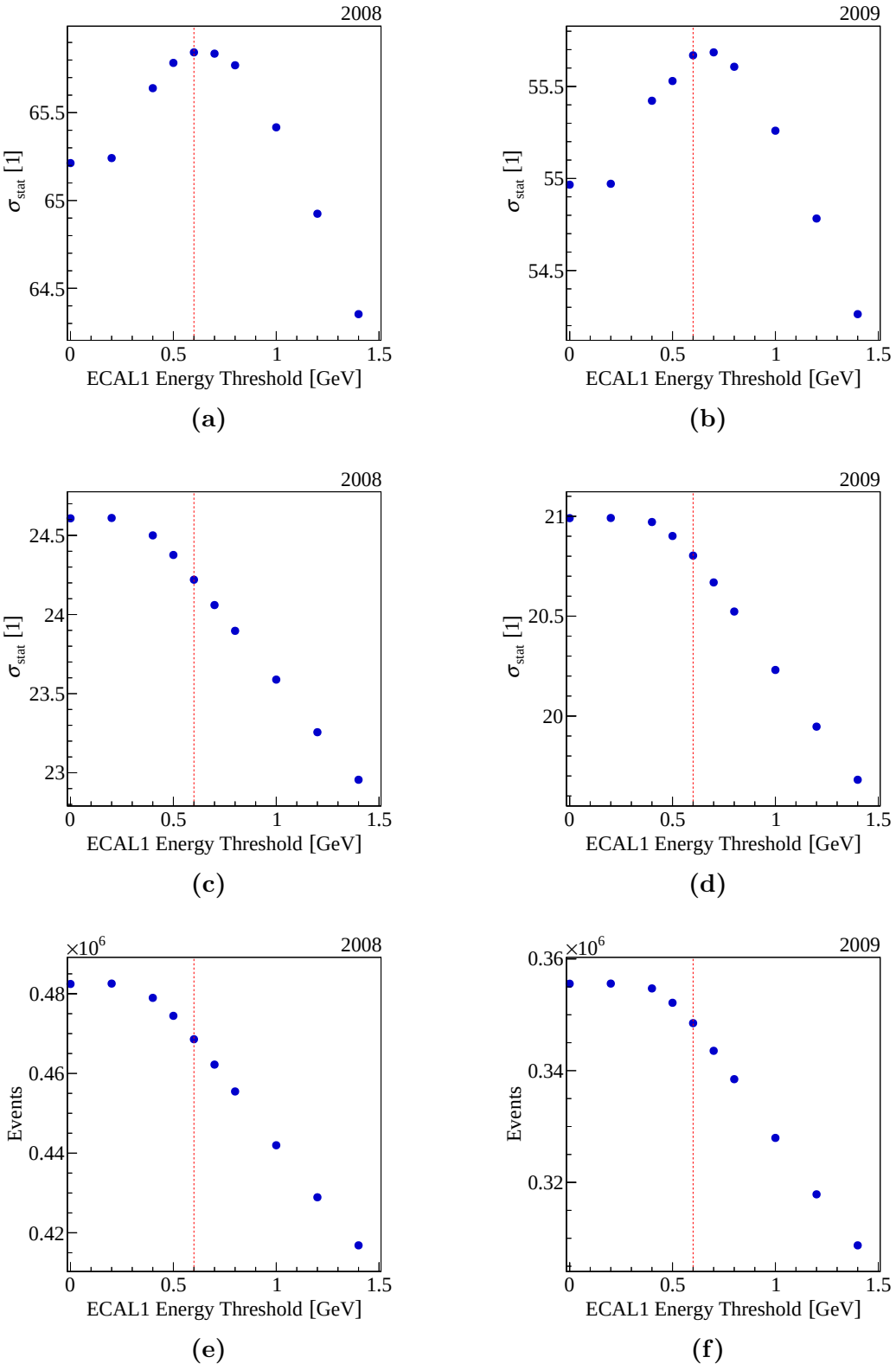

Figure 3.6: Statistical significances as a function of the cluster-energy threshold applied to ECAL1 clusters for (a) and (b) the π^0 peak and (c) and (d) the $\omega(782)$ peak. The number of selected events is shown in (e) and (f). The left column shows the 2008 data, the right one the 2009 data. The chosen threshold value is indicated by the red vertical line.

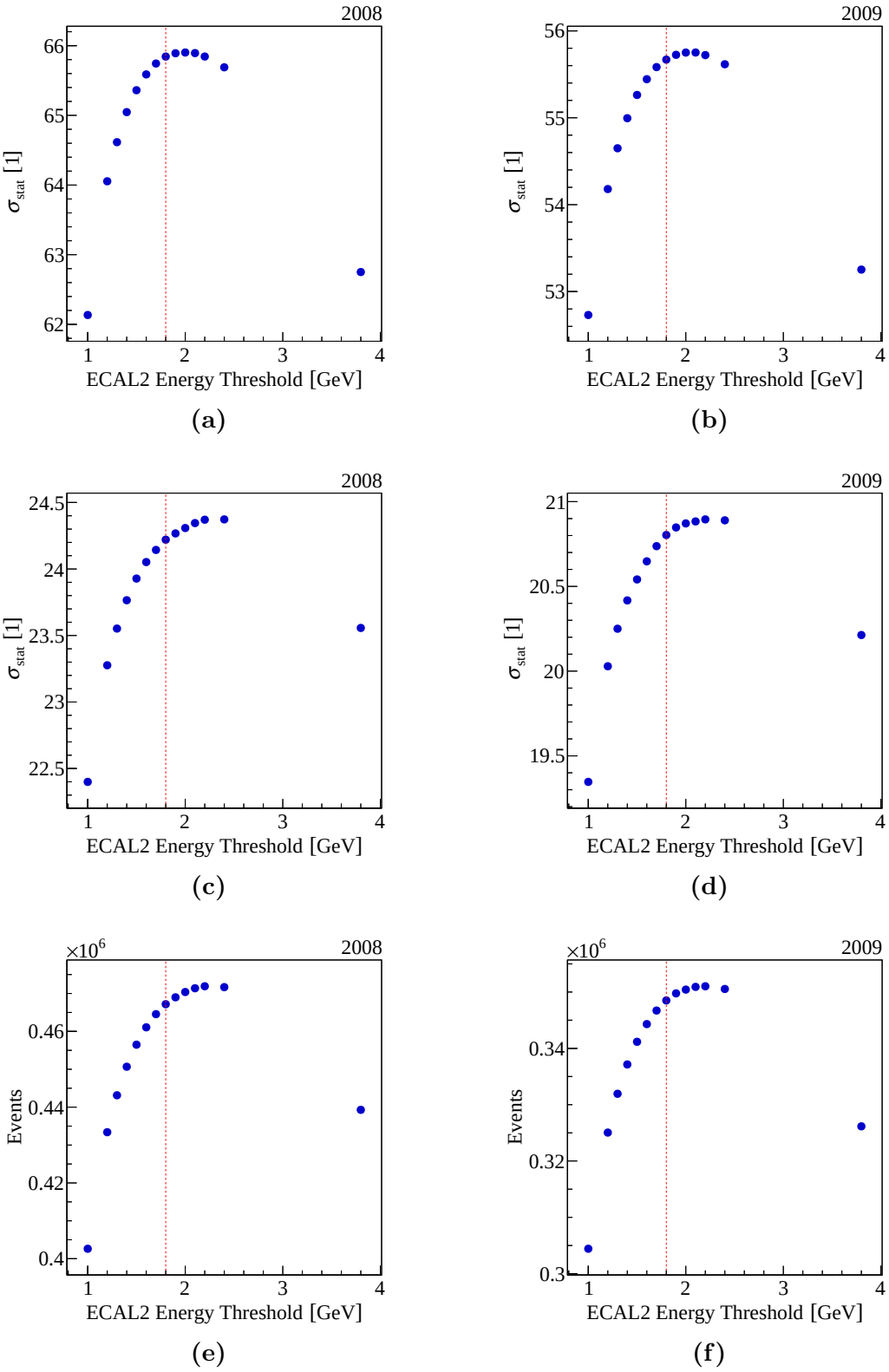

Figure 3.7: Statistical significances as a function of the cluster-energy threshold applied to ECAL2 clusters for (a) and (b) the π^0 peak and (c) and (d) the $\omega(782)$ peak. The number of selected events is shown in (e) and (f). The left column shows the 2008 data, the right one the 2009 data. The chosen threshold value is indicated by the red vertical line.

Table 3.3: Parameters obtained by fitting Eqs. (3.8) and (3.9) to the red data points shown in Fig. 3.8.

Parameters		2008		2009	
		ECAL1	ECAL2	ECAL1	ECAL2
C_{-3}^T	$[\mathrm{ns}\,(\mathrm{GeV}/c^2)^3]$	—	0.003 51	—	0.0506
C_{-2}^T	$[\mathrm{ns}\,(\mathrm{GeV}/c^2)^2]$	−0.009 62	−0.120	−0.0150	−0.320
C_{-1}^T	$[\mathrm{ns}\,\mathrm{GeV}/c^2]$	0.102	0.612	0.135	0.542
C_0^T	[ns]	0.700	0.287	−0.668	−0.874
C_1^T	$[\mathrm{ns}/(\mathrm{GeV}/c^2)^1]$	−0.0278	0.0160	−0.0249	0.004 02
C_2^T	$[\mathrm{ns}/(\mathrm{GeV}/c^2)^2]$	0.000 474	-8.44×10^{-5}	0.000 511	-2.49×10^{-5}
C_3^T	$[\mathrm{ns}/(\mathrm{GeV}/c^2)^3]$	—	1.18×10^{-7}	—	6.61×10^{-8}

0.5 GeV wide slices of the cluster energy. This is shown in Fig. 3.8. The means (red points in Fig. 3.8) are not consistent with 0 and a energy-dependent post-correction is applied. For ECAL1 the means of the Gaussians are empirically parametrized by the function

$$T_{\mathrm{cluster}}^{\mathrm{ECAL1}}(E;\{C_i^T\}) = \frac{C_{-2}^T}{E^2} + \frac{C_{-1}^T}{E} + C_0^T + C_1^T E + C_2^T E^2, \tag{3.8}$$

and for ECAL2 by the function

$$T_{\mathrm{cluster}}^{\mathrm{ECAL2}}(E;\{C_i^T\}) = \frac{C_{-3}^T}{E^3} + \frac{C_{-2}^T}{E^2} + \frac{C_{-1}^T}{E} + C_0^T + C_1^T E + C_2^T E^2 + C_3^T E^3. \tag{3.9}$$

These functions are fitted to the 2008 and 2009 data individually. Table 3.3 lists the obtained parameters. The parametrizations obtained for 2008 data are similar to the ones used in Ref. [26]. Fig. 3.9 shows the resulting distribution of the cluster times vs. the cluster energy after subtracting the corresponding parametrization from each cluster time. Thereby the mean cluster time is shifted to a value consistent with 0.

The energy dependence of the cluster time resolution, i.e. the widths of the Gaussians fitted in energy slices, is empirically parametrized by the function

$$\sigma_{T,\mathrm{cluster}}(E) = \frac{C_{-1}^\sigma}{E} + C_0^\sigma + C_1^\sigma E. \tag{3.10}$$

Table 3.4 lists the parameter values obtained by fitting Eq. (3.10) to the widths of the Gaussians fitted in each slice of the cluster energy in Fig. 3.8 (blue points in Fig. 3.10). For a good cluster candidate, the corrected cluster time must lie within $\pm 3\sigma_{T,\mathrm{cluster}}$ to remove off-time clusters. Unlike for the time, the parametrizations of the cluster time resolutions obtained for 2008 data are around 10% lower than the ones used in Ref. [26]. The origin of this small difference is not clear. Both analyses use a similar method and the different selected final state should not have an impact on this dependence.

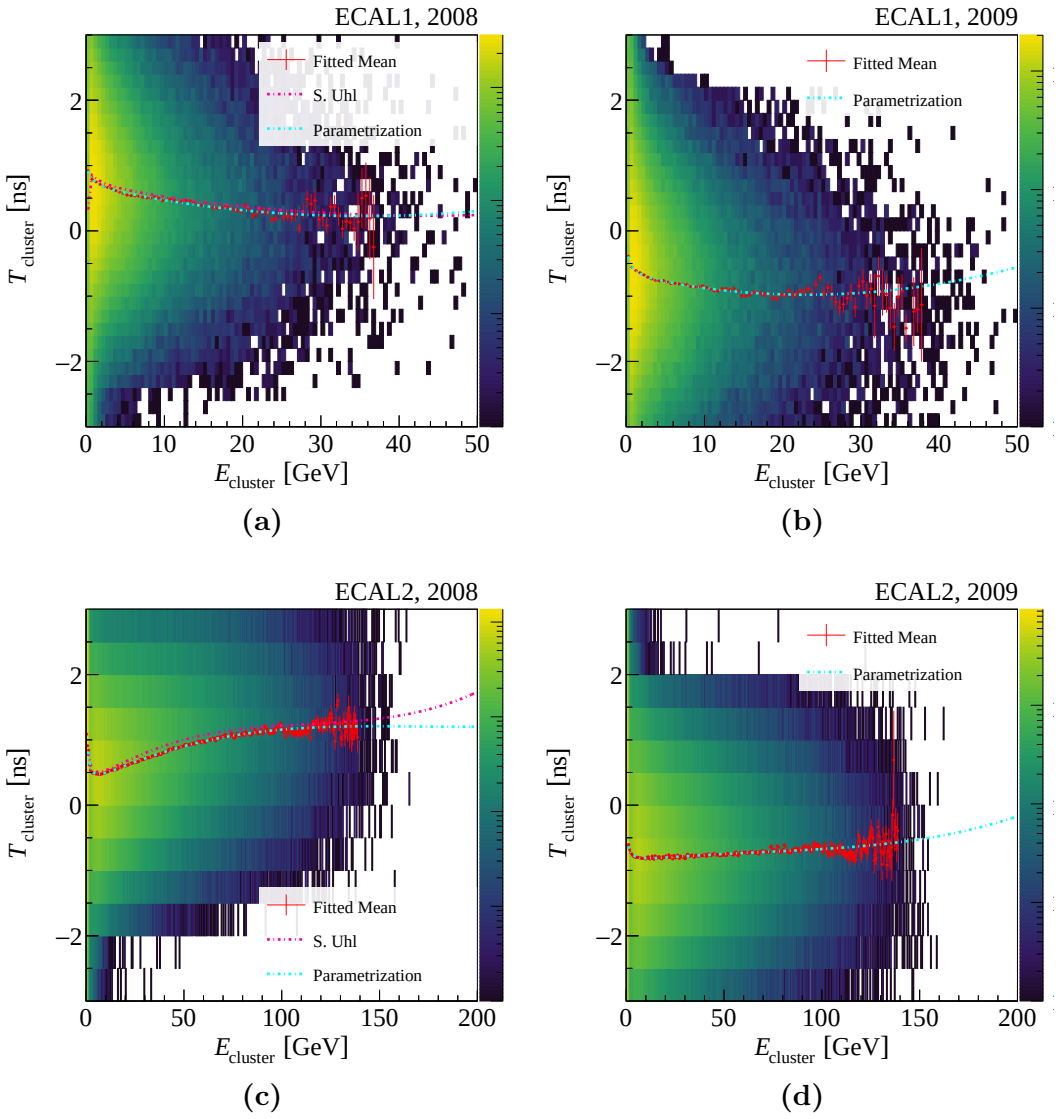

Figure 3.8: Distribution of the measured ECAL cluster times vs. the cluster energy. (a) and (b) show the distributions for ECAL1 for 2008 and 2009, respectively, and (c) and (d) show the same for ECAL2. The red points show the mean values obtained by fitting a Gaussian to each energy slice, the cyan curve represents the result of a fit of Eqs. (3.8) and (3.9) to the mean values for ECAL1 and ECAL2, respectively, and the magenta curves show the results of a similar fit performed on the 2008 data for the $\pi^-\pi^0\pi^0$ final state in Ref. [26]. Note the logarithmic color scale.

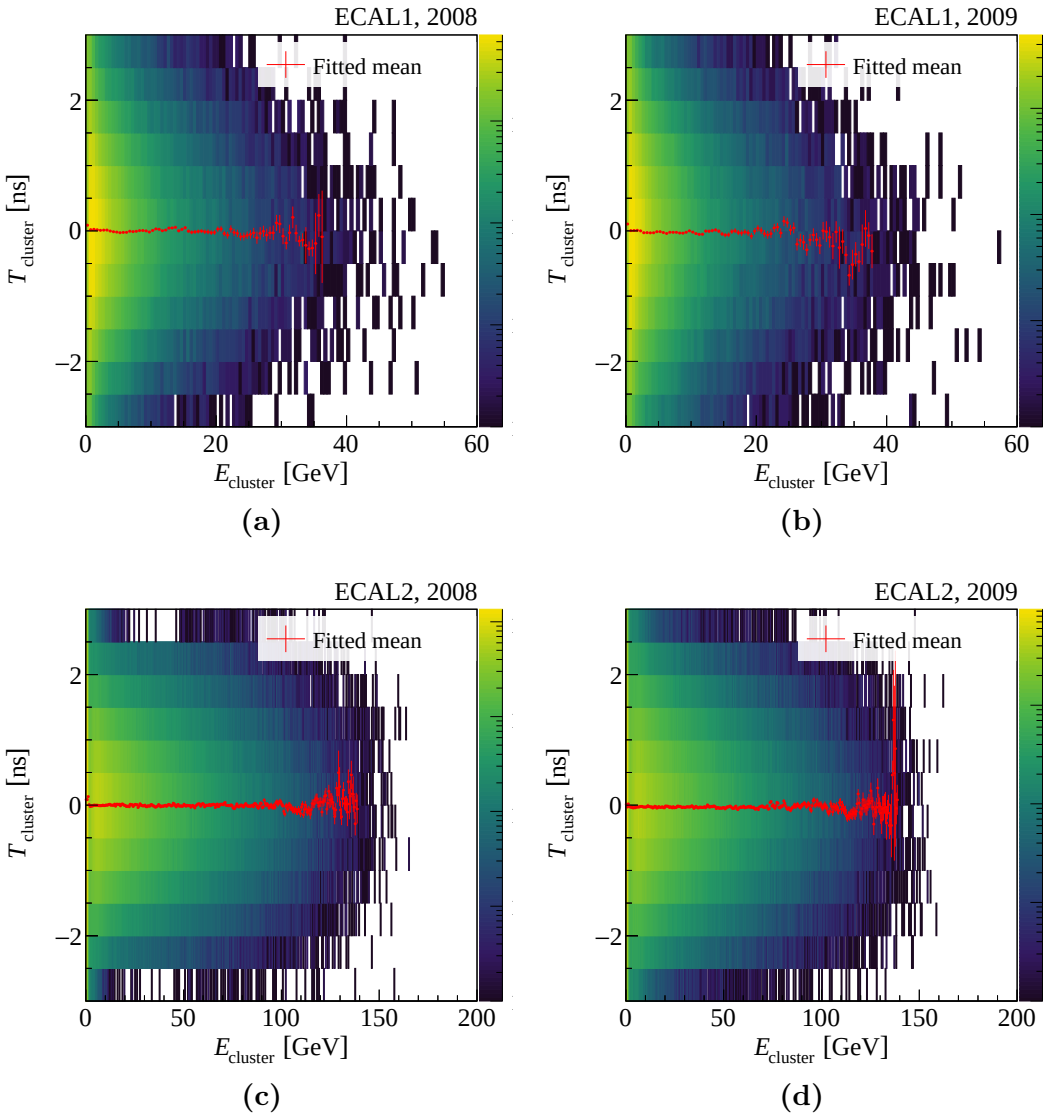

Figure 3.9: Distribution of the corrected ECAL cluster times vs. the cluster energy. (a) and (b) show the distributions for ECAL1 for 2008 and 2009, respectively, and (c) and (d) show the same for ECAL2. The red points show the mean values obtained by fitting a Gaussian to each energy slice. Note the logarithmic color scale.

Table 3.4: Parameters used obtained by fitting Eq. (3.10) to the blue data points in Fig. 3.10.

		2008		2009	
Parameters		ECAL1	ECAL2	ECAL1	ECAL2
C_{-1}^{σ}	$[\text{ns}\,\text{GeV}/c^2]$	0.345	0.640	0.362	0.542
C_{0}^{σ}	[ns]	0.908	0.760	0.810	0.826
C_{1}^{σ}	$[\text{ns}\,(\text{GeV}/c^2)^{-1}]$	0.001 69	0.001 39	0.000 931	0.000 506

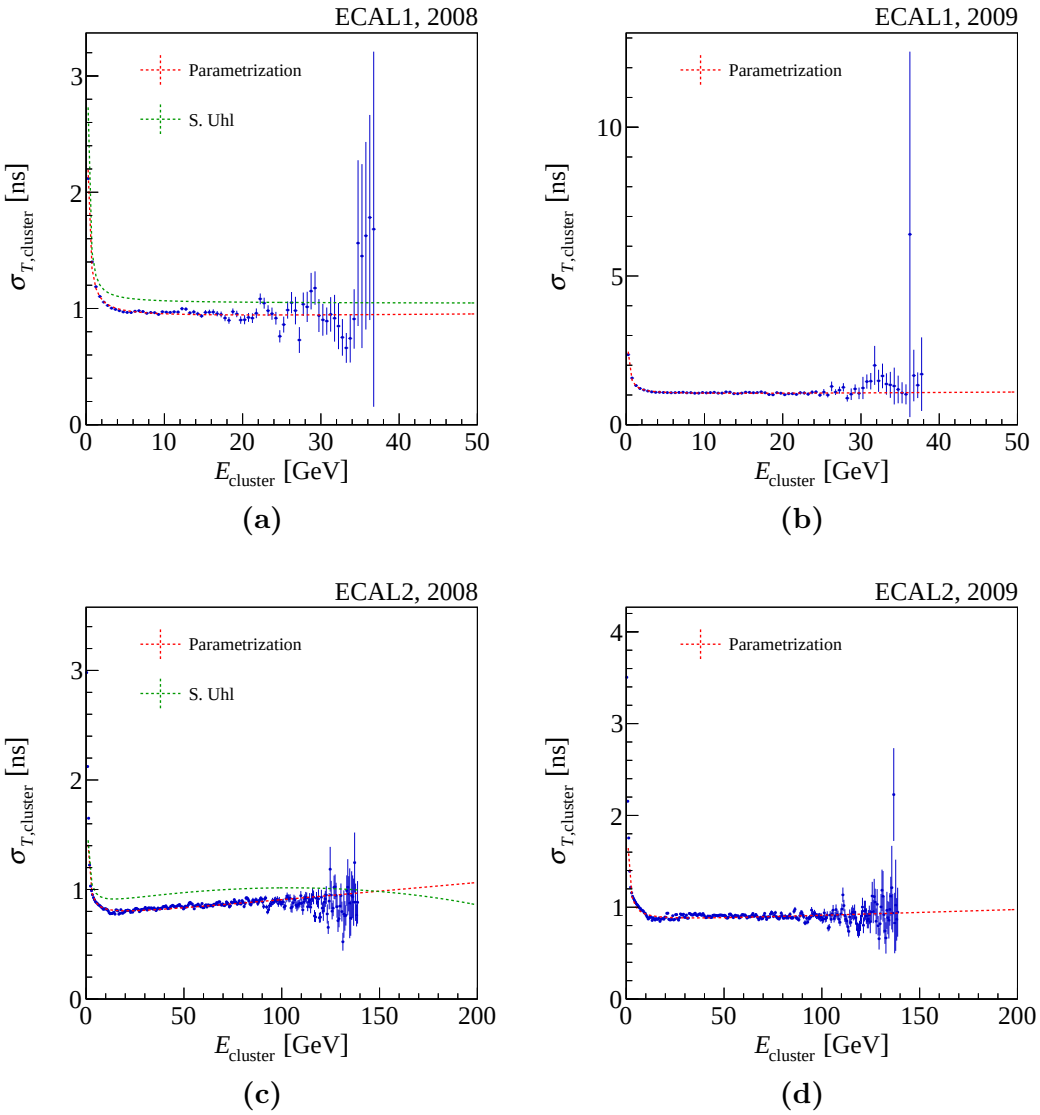

Figure 3.10: Cluster time resolutions as a function of the cluster energy for (a) ECAL1 2008, (b) ECAL1 2009 (c) ECAL2 2008, and (d) ECAL2 2009, as obtained from Gaussian fits to the cluster time distribution in slices of the cluster energy (blue points). The red curve shows the result of a fit of Eq. (3.10) to the resolutions. The curve in green shows the fit of Ref. [26] for the $\pi^-\pi^0\pi^0$ final state for 2008 data with a different parametrization.

3.5 π^0 Reconstruction

A candidate event needs to pass two steps in order to reconstruct two π^0 candidates from the four photon candidates. First, the four photons are combined to two π^0 (see Section 3.5.1) and then a kinematic fit shifts the invariant masses of both π^0 to the nominal π^0 mass (see Section 3.5.2). Since not all cuts presented in Table 3.13 are necessary for π^0 investigations, the cuts written in blue are not used for the studies of $m_{\gamma\gamma}$.

3.5.1 π^0 Pair Selection

The reconstruction of a π^0 from two photons is based on the same approach as the analysis of $\pi^-\pi^0\pi^0$ in Section 2.4.3 in Ref. [26]. Since each photon is detected either by ECAL1 or ECAL2, three different photon-pair cases of combining two photons into a pair arise:

1. "ECAL1 pair": both photons are detected in ECAL1.
2. "ECAL2 pair": both photons are detected in ECAL2.
3. "Mixed ECAL pair": one of the photons is detected in ECAL1 and the other in ECAL2.

Fig. 3.11 shows the $m_{\gamma\gamma}$ distributions for all photon-pair cases j for 2008; Fig. 3.12 for 2009. The measured distributions are fitted by the sum of a double-Gaussian distribution D_G (see Eq. (B.1)) for the π^0 peak and a polynomial of third degree representing background, i.e.

$$\begin{aligned}\frac{dN}{dm}(m; A_\pi, R_\pi, m_{\pi^0,\mathrm{mean}}, \sigma_{1,\mathrm{mass}}, \sigma_{2,\mathrm{mass}}, \{B_i^\pi\}) = \\ A_\pi D_\mathrm{G}(m; R_\pi, m_{\pi^0,\mathrm{mean}}, \sigma_{1,\mathrm{mass}}, \sigma_{2,\mathrm{mass}}) + \sum_{i=0}^{3} B_i^\pi m^i.\end{aligned} \tag{3.11}$$

The fit range is from $0.07\,\mathrm{GeV}/c^2$ to $0.2\,\mathrm{GeV}/c^2$. The mean m_{π^0} of the π^0 peak is used as the reconstructed mass of π^0 in the combination case j and denoted as $m_{\pi^0}^j$. The width σ^j of the π^0 peak, i.e. the mass resolution, in the photon-pair case j is obtained by Eq. (B.3). Tables 3.5 and 3.6 list the parameters obtained from this fit for 2008 and 2009 data, respectively. The widths obtained from 2008 data are larger than the widths estimated in Ref. [26] due to systematic differences. Ref. [26] uses a single Gaussian as π^0 peak, which describes the center of the peak well but underestimates the contributions further away from the center. Fitting a double-Gaussian describes the entries in the tails more precisely and therefore results in a wider π^0 peak with larger width. The χ^2_red value is significantly larger than 1 and especially large for

Table 3.5: Fit parameters obtained by fitting the π^0 peaks in the $m_{\gamma\gamma}$ distribution in 2008 data shown in Fig. 3.11. The yields are calculated using 3σ intervals around the peak. The π^0 peak widths obtained by S. Uhl for the $\pi^-\pi^0\pi^0$ channel in Ref. [26] are listed for comparison.

Parameters		ECAL1	ECAL2	mixed ECAL
$m_{\pi^0,\text{mean}}$	[MeV/c^2]	135.09	135.39	136.56
R_π		0.50	0.63	0.54
$\sigma_{1,\text{mass}}$	[MeV/c^2]	7.60	3.49	7.05
$\sigma_{2,\text{mass}}$	[MeV/c^2]	13.91	8.91	13.92
χ^2_{red} (NDF)		7.6 (56)	24 (56)	4.6 (56)
σ_{mass}	[MeV/c^2]	10.75	5.51	10.24
σ_{mass}(Uhl)	[MeV/c^2]	8.85	3.88	8.32
Signal yield		410 919	2 971 396	646 702
Background yield		285 751	1 054 007	619 475

ECAL2 photon-pair cases. This indicates a small systematic difference between data and fit function, which is only visible due to low statistical uncertainties. For each case j, an individual mass window is used based on a $3\sigma^j$ cut around the fitted π^0 peak in the corresponding $m_{\gamma\gamma}$ spectrum.

To decide whether an event contains a $\pi^0\pi^0$ candidate, all three possible disjoint combinations of four photons into two $\gamma\gamma$ pairs, i.e. combinations in which all four photons are used to construct two $\gamma\gamma$ pairs, are considered. Fig. 3.13 shows the invariant masses of the two disjoint $\gamma\gamma$ pairs for all possible combinations. In each $m_{\gamma\gamma}$ a band is visible around the nominal π^0 mass with a peak at the intersection of both bands containing a $\pi^0\pi^0$ pair[b]. To select a $\pi^0\pi^0$ pair in each event, we apply an elliptic cut in the ($m_{\gamma_1\gamma_2}$-$m_{\gamma_3\gamma_4}$) plane in Fig. 3.13, i.e. we require exactly one disjoint combination of two photon pairs a and b that represent two π^0 candidates that fulfill

$$\left(\frac{m_{\gamma_1\gamma_2} - m^a_{\pi^0}}{3\sigma^a}\right)^2 + \left(\frac{m_{\gamma_3\gamma_4} - m^b_{\pi^0}}{3\sigma^b}\right)^2 \leq 1. \tag{3.12}$$

The values of $m^j_{\pi^0}$ and σ^j depend on the photon-pair case and are given in Table 3.7. About 2% of the events fulfill Eq. (3.12) with more than one disjoint combination of two photon pairs. They are discarded.

[b] Small contributions of $\eta\pi^0$ from other final-states are visible in the π^0 bands. Selecting exactly two π^0 candidates discards these events from the selected data sample.

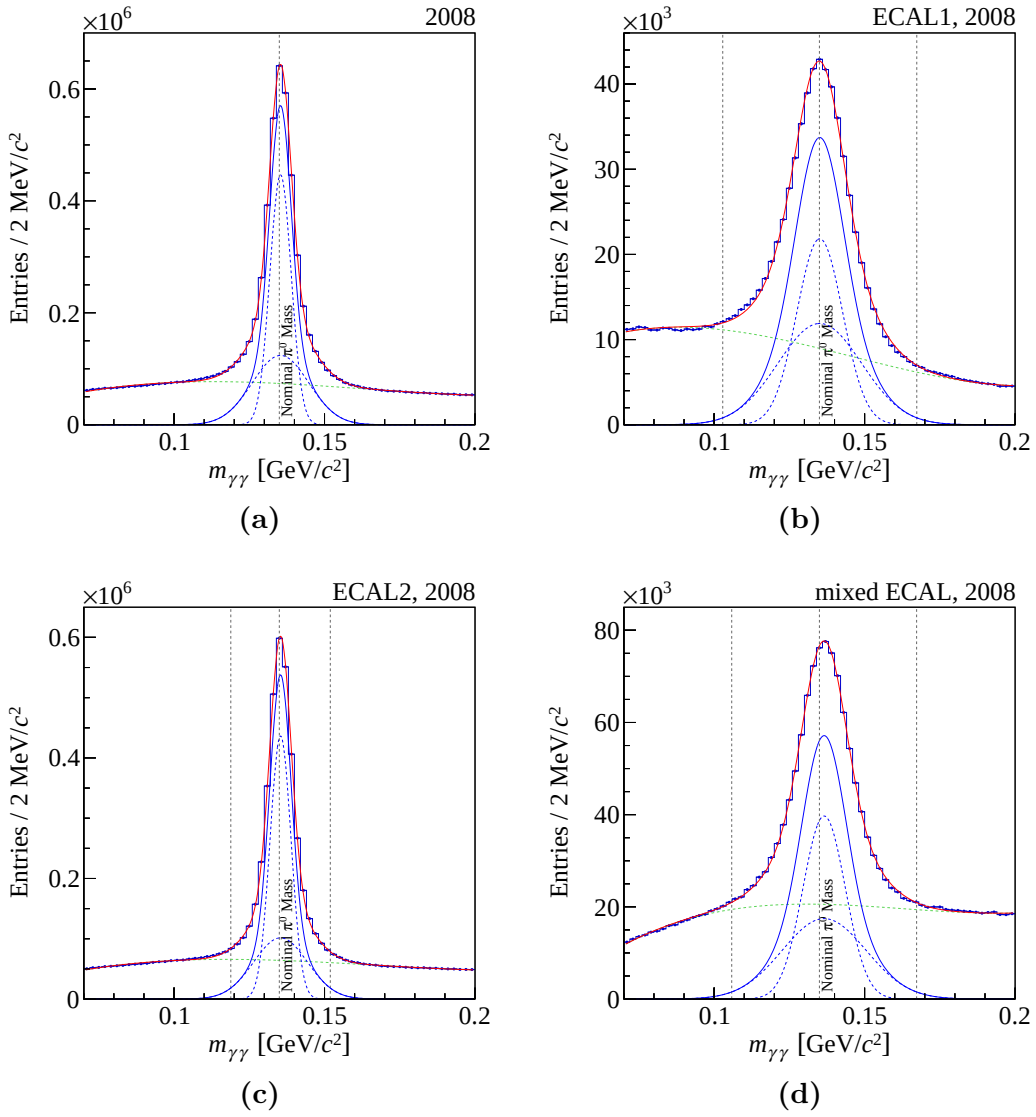

Figure 3.11: $m_{\gamma\gamma}$ distributions for (a) all photon pairs, (b) ECAL1 photon pairs, (c) ECAL2 photon pairs, and (d) mixed ECAL photon pairs for data taken in 2008. The blue solid curve represents the signal component, which is the sum of two Gaussians represented by the blue dashed curves. The green dashed curve represents the background component. The red curve represents the result of fitting Eq. (3.11) to the $m_{\gamma\gamma}$ distribution. The central vertical line indicates the nominal π^0 mass, while the outer two vertical lines indicate the selected $m_{\gamma\gamma}$ window.

Table 3.6: Fit parameters obtained by fitting the π^0 peaks in the $m_{\gamma\gamma}$ distribution in 2009 data shown in Fig. 3.12. The yields are calculated using 3σ intervals around the peak.

Parameters		2009 ECAL1	2009 ECAL2	2009 mixed ECAL
$m_{\pi^0,\text{mean}}$	[MeV/c^2]	134.02	135.40	135.85
R_π		0.30	0.59	0.52
$\sigma_{1,\text{mass}}$	[MeV/c^2]	6.86	3.44	7.25
$\sigma_{2,\text{mass}}$	[MeV/c^2]	11.20	8.87	13.53
χ^2_{red} (NDF)		13 (56)	30 (56)	9.0 (56)
σ_{mass}	[MeV/c^2]	9.89	5.66	10.26
Signal yield		311 566	2 126 030	470 775
Background yield		210 210	778 321	451 140

Table 3.7: Cut parameters used for the photon-pair selection. The values are derived from the fit parameters in Tables 3.5 and 3.6.

	2008		2009	
	$m^j_{\pi^0}$ [MeV/c^2]	$3\sigma^j$ [MeV/c^2]	$m^j_{\pi^0}$ [MeV/c^2]	$3\sigma^j$ [MeV/c^2]
ECAL1	135.1	32.3	134.0	29.7
ECAL2	135.4	16.5	135.4	17.0
mixed ECALs	136.6	30.8	135.9	30.8

3.5.2 Kinematic π^0 Fit

Since the two selected π^0 are truly propagating particles, their four-momenta should have a mass equal to the nominal π^0 mass. We use this constraint by applying it in a kinematic fit introduced by T. Schlüter in Ref. [29] in order to obtain better estimates for the π^0 four-momenta. This fit is done independently for both π^0. From the measurement a set of physical observables $\vec{\eta} = (x_1, y_1, E_1, x_2, y_2, E_2)$ is given. Here $x_i = X_i/\sqrt{X_i^2 + Y_i^2 + Z_i^2}$ and $y_i = Y_i/\sqrt{X_i^2 + Y_i^2 + Z_i^2}$ with the measured spatial position (X_i, Y_i, Z_i) and the energy E_i of photon i. The uncertainties of the energy of clusters in ECAL1 and of the spatial position are taken from the reconstruction software, while for clusters measured in ECAL2 we estimate the uncertainties of the energies by parametrizing the relative resolution $\Delta E_{\text{cluster}}/E_{\text{cluster}}$ of the cluster energy taken from the reconstruction software as a function of the cluster energy. This is shown in Fig. 3.14. Gaussians are fitted to the relative resolutions of the cluster energy in 2 GeV wide slices of the cluster energy. The means (red points)

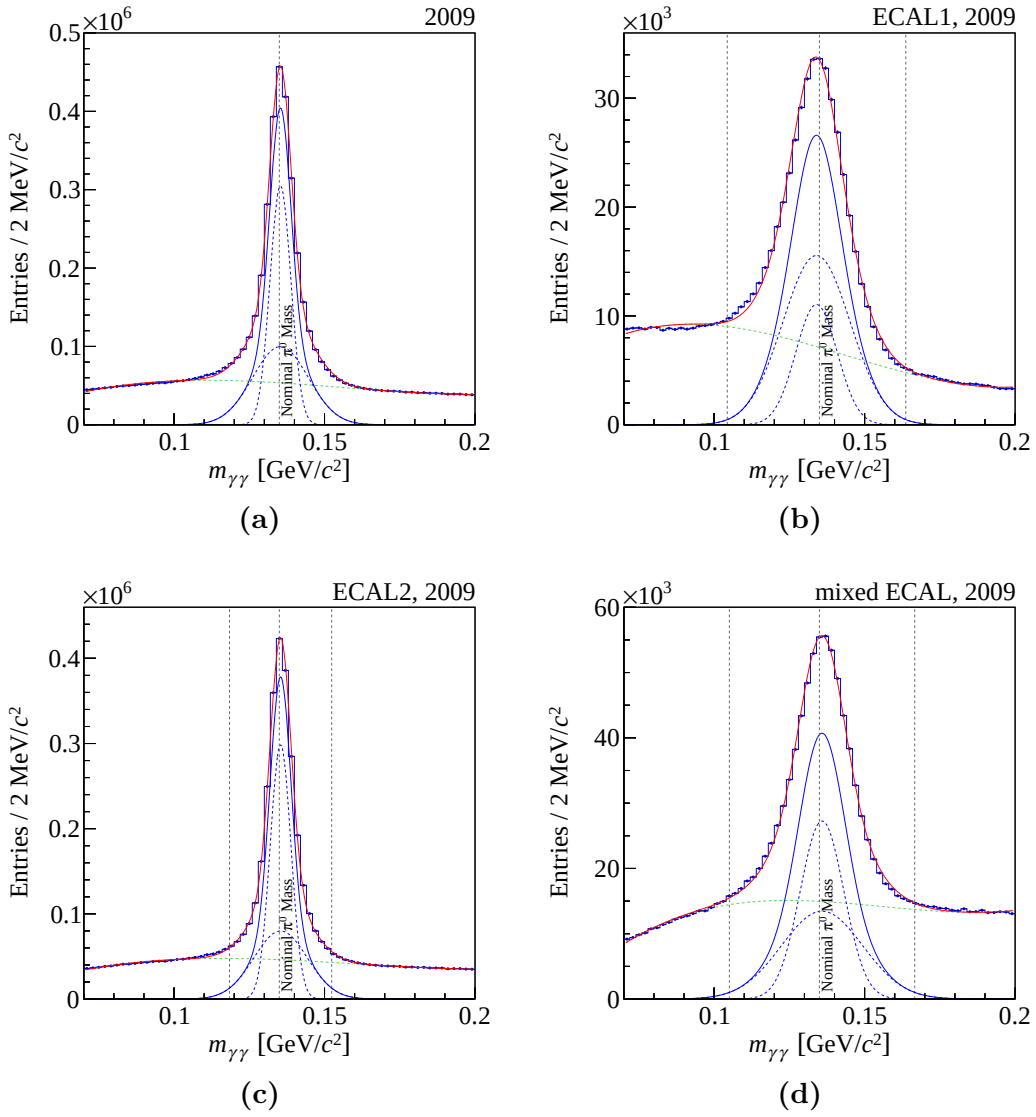

Figure 3.12: Similar to Fig. 3.11 but showing the $m_{\gamma\gamma}$ distributions for 2009.

are parametrized by the function

$$\frac{\Delta E}{E} = \sqrt{C_0^E + \frac{C_1^E}{E} + \frac{C_2^E}{E^2}}. \tag{3.13}$$

Fitting the function for 2008 and 2009 data individually results in fits compatible with the parametrization obtained by D. Spühlbeck [30]. Therefore, the parameters of D. Spühlbeck listed in Table 3.8 are used for the energy uncertainties of ECAL2 clusters for both years.

The kinematic fit modifies $\vec{\eta}$ by adding a shift $\vec{\epsilon}$ to obtain a set of observables

$$\vec{\eta}' = \vec{\eta} + \vec{\epsilon}, \tag{3.14}$$

that minimises

$$\chi^2(\vec{\epsilon}) = \vec{\epsilon}^{\,T}\mathbf{V}^{-1}\vec{\epsilon} \tag{3.15}$$

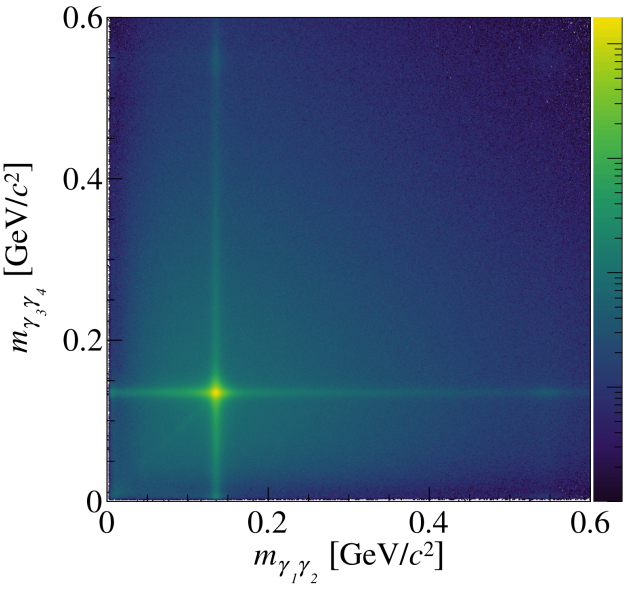

Figure 3.13: Distribution of the invariant masses of the two disjoint $\gamma\gamma$ pairs for all three combinations per event. Note the logarithmic color scale.

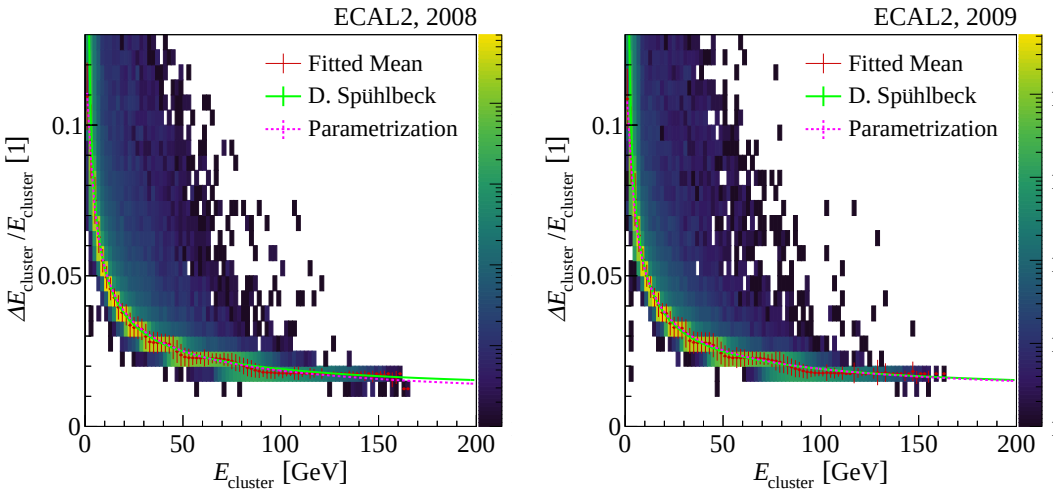

Figure 3.14: Distribution of the cluster energy resolutions vs. the cluster energies for clusters measured in ECAL2 for (a) 2008 and (b) 2009. Note the logarithmic color scale. The red data points are the mean values obtained by fitting a Gaussian to each energy slice. The pink curve fits Eq. (3.13) to this means. The green curve shows the result of a similar fit obtained by D. Spühlbeck.

Table 3.8: Parameters of Eq. (3.13) obtained by D. Spühlbeck [30].

C_0^E	C_1^E	C_2^E
$2.518569 \cdot 10^{-2}$	$1.401856 \cdot 10^{-2}$	$1.1025 \cdot 10^{-6}$

under the physical constraint

$$F(\vec{\eta}\,') = E_1 E_2 (1 - x_1 x_2 - y_1 y_2 - z_1 z_2) - m_{\pi^0}^2 = 0. \tag{3.16}$$

Here $\mathbf{V}$ is the covariance matrix of the measured values $\vec{\eta}$. This corresponds to finding a set of values $\vec{\eta}\,'$ that satisfy the π^0-mass constraint and are most compatible with the measured observables $\vec{\eta}$ assuming Gaussian-distributed uncertainties represented by $\mathbf{V}$. Since the constraint is nonlinear, the equations cannot be solved in closed form but the solution is solved with a numerical method. Changes are iteratively applied up until the relative deviation from the physical constraint in Eq. (3.16), i.e. $F(\vec{\eta}\,')/m_{\pi^0}^2$, is smaller than a precision goal.

To determine the optimum value of the precision goal the statistical significance of the $\omega(782)$ peak is optimised based on the method described in Section 3.4.1. Fig. 3.15 shows σ_{stat} and the numbers of selected events as a function of the precision-goal threshold for the 2008 and 2009 data sets. For both years, the significance starts to drop for values below 10^{-10} and therefore we set the precision goal to 10^{-10}.

Studying the distribution of the pull $\wp_i$ for each observable i in $\vec{\eta}\,'$ tells us how well the fit works. It is defined as

$$\wp_i = \frac{\epsilon_i}{\sigma_{\epsilon_i}}, \tag{3.17}$$

where ϵ_i is the total shift of the observable and σ_{ϵ_i} is the uncertainty of ϵ_i. If the above-mentioned assumptions are valid, all pulls are expected to be distributed according to a Standard Gaussian with a mean of 0 and a width of 1. Fig. 3.16 shows the distributions of the pulls of the fits for all variables. We fit the pulls with a Gaussian in the range from -2 to 2. Although the fit parameters are compatible with Standard Gaussians with a mean of 0, we observe clear deviations of the pull distributions from the Gaussian shape. For the regions close to 0 the pulls slightly overshoot the Gaussian. The tails of the pull significantly overshoot the Gaussian. Therefore, there seems to be no systematic bias but an underestimation of the statistical uncertainties for the kinematic fits with pulls in the non-Gaussian tails.

Another quantity that helps us to estimate the quality of the kinematic fit is the distribution of the P-values of all fits. The P-value measures the probability that a χ^2 value higher than the observed one occurs in the fit if the experiment is repeated [31]. Fig. 3.17 shows the obtained P-value distribution for the fits. If our assumptions that the uncertainties are Gaussian distributed and that we observe true π^0 decays are valid, the P-value distribution is expected to be uniform. We observe deviations from the expected uniform distribution in two regions. There is a significant enhancement for P-values close to 0. This corresponds to the non-Gaussian tails in the pull distributions in Fig. 3.16 and

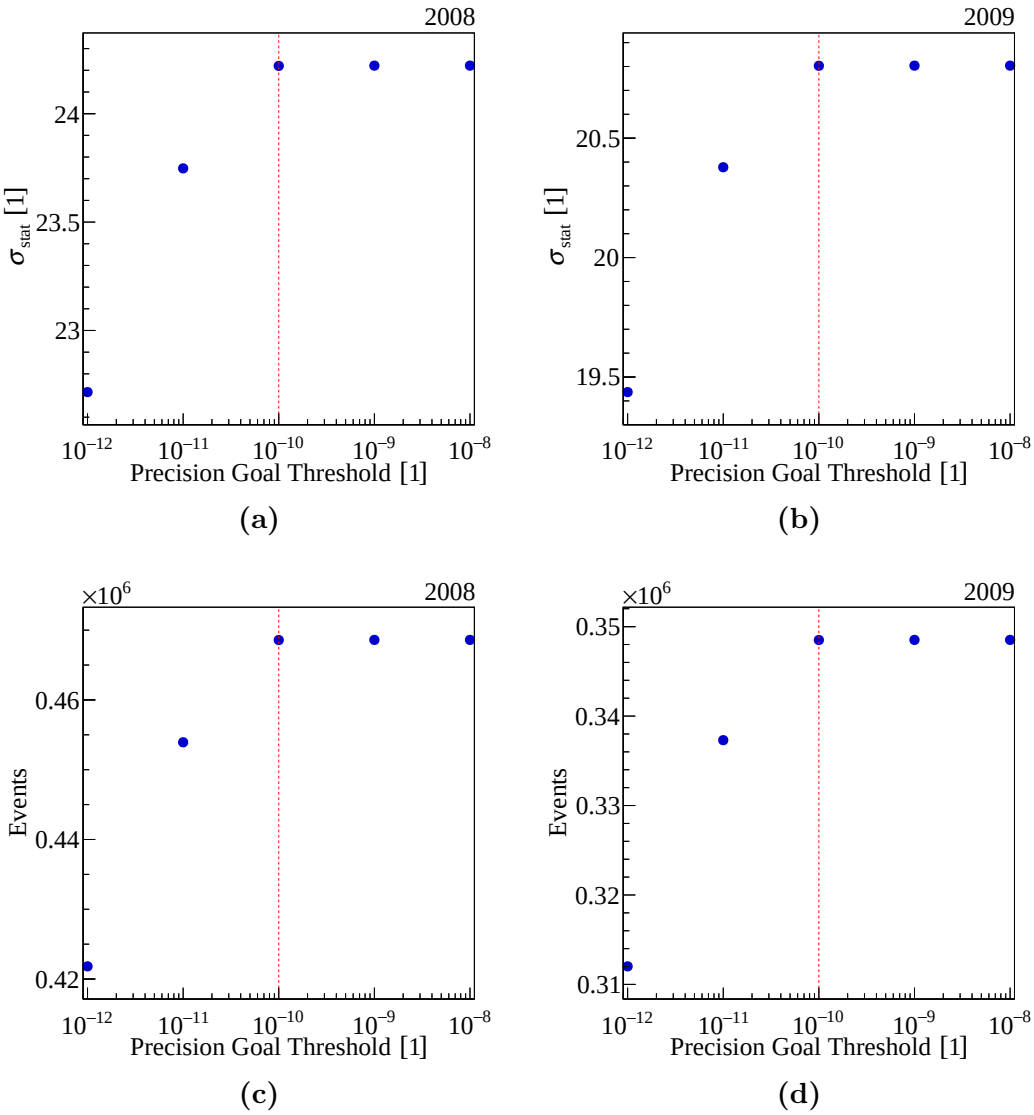

Figure 3.15: Statistical significances of (a) and (b) the $\omega(782)$ peak as a function of the cluster-energy threshold applied to ECAL1 clusters. The number of selected events is shown in (c) and (d)). The left column shows 2008 data and the right one 2009 data. The chosen threshold value is indicated by the red vertical line.

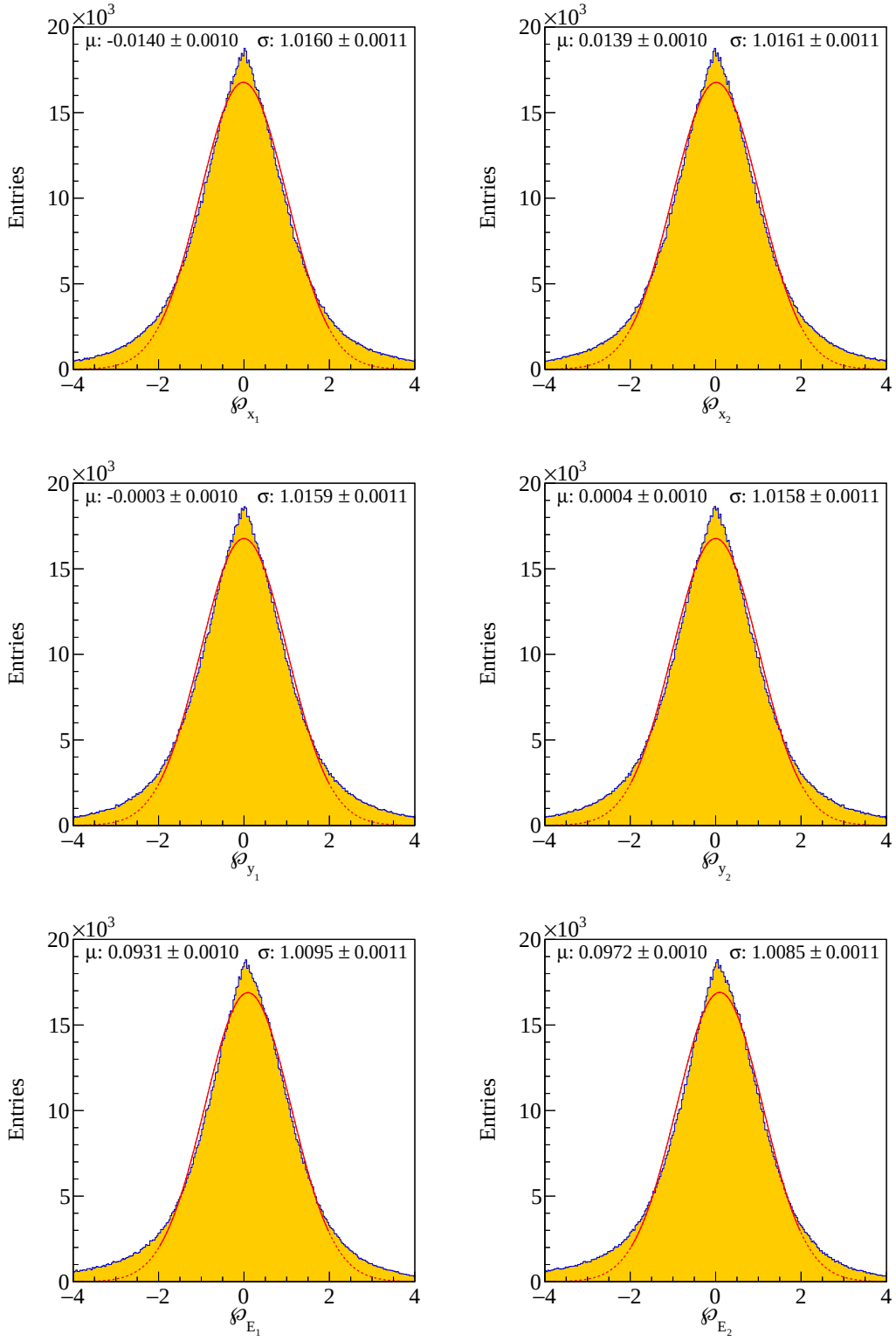

Figure 3.16: Distributions of the pulls $\wp_i$ defined in Eq. (3.17) for the kinematic fit. The left and the right column correspond to the values of the first and second π^0, respectively. The red curves represent the result of fitting a Gaussian to the distribution; μ gives the mean and σ the width of the Gaussian.

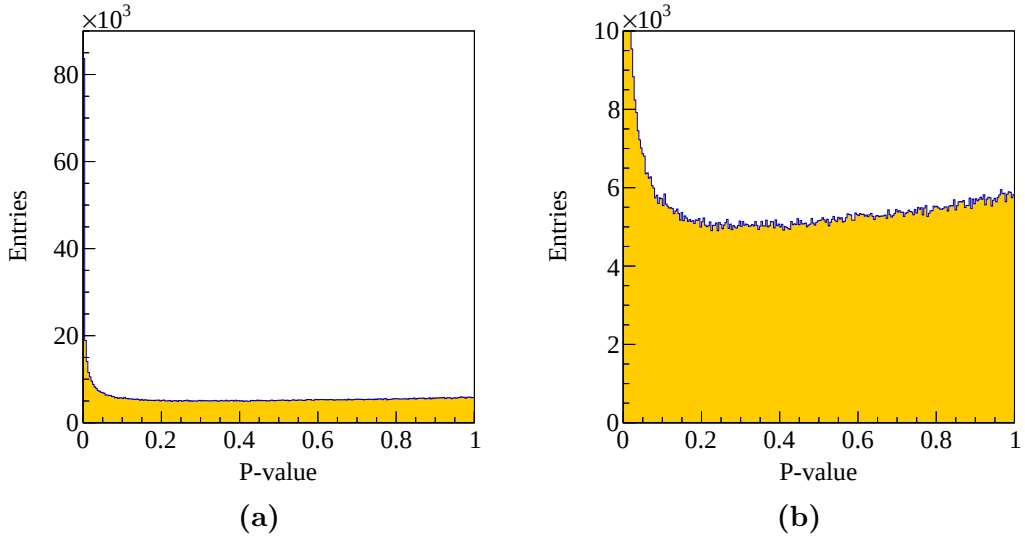

Figure 3.17: Distribution of the P-value of the kinematic fits. (a) shows the full range, while (b) is a zoomed view to show the rising trend for increasing P-values in the high p-Value region above about 0.2.

is a hint that we underestimate the uncertainties in these fits. We also observe a slight increase towards high P-values, which corresponds to the overshoot of the pulls in the regions around their means.

3.6 $\omega(782)$ Selection

After the kinematic fit of the two π^0, the four-momenta of all five final-state pions are known and a $\pi^-\pi^0\pi^+$ subsystem is selected as $\omega(782)$. As discussed in Appendix B.2, the measured $\omega(782)$ peak is characterised by the decay width and the resolution of COMPASS. Fig. 3.18 shows the $m_{\pi^-\pi^0\pi^+}$ distribution fitted by the sum of several functions for the $\omega(782)$ peak and a polynomial of second degree as background. The fit range is from $0.68\,\mathrm{GeV}/c^2$ to $0.88\,\mathrm{GeV}/c^2$. In Figs. 3.18a and 3.18b we fit a Voigt V (see Eq. (B.7)) and a relativistic Voigt V_{rel} (see Eq. (B.8)) distribution as $\omega(782)$ peak component, respectively. While the Voigt and the relativistic Voigt assume a Gaussian resolution, the simulation of the resolution of COMPASS, which will be discussed in Section 5.1, favors a double-Gaussian distribution (see Eq. (B.1)) as resolution function. Therefore, Fig. 3.18c shows the fit with $D_{\mathrm{DG}}^{\mathrm{BW}}$ (see Eq. (B.13)), which is similar to a Voigt distribution but with a double-Gaussian resolution function, and Fig. 3.18d shows the fit with $D_{\mathrm{DG}}^{\mathrm{BW,rel}}$ (see Eq. (B.14)), which is similar to a relativistic Voigt distribution but with a double-Gaussian resolution function. The ratio R_D of the two Gaussians and the ratio $\sigma_{1,\mathrm{D}}/\sigma_{2,\mathrm{D}}$ between the two widths of the Gaussians are fixed for both $D_{\mathrm{DG}}^{\mathrm{BW}}$ and $D_{\mathrm{DG}}^{\mathrm{BW,rel}}$ by the simulated values listed in Table 5.3. Table 3.9 lists the obtained relevant fit values for

Table 3.9: Fit parameters obtained by the fits of the $m_{\pi^-\pi^0\pi^+}$ distribution for 2008 data shown in Fig. 3.18.

Parameters		V	V_{rel}	$D_{\text{DG}}^{\text{BW}}$	$D_{\text{DG}}^{\text{BW,rel}}$
m_0	[MeV/c^2]	784.18	784.74	784.68	784.74
σ	[MeV/c^2]	3.63	3.72	3.97	4.22
Γ_0	[MeV/c^2]	14.23	14.05	13.50	13.06
χ^2_{red}	(NDF)	5.0 (93)	6.7 (93)	4.9 (93)	6.6 (93)

the four different fits. The fits describe the data fairly well, but due to the high statistical precision small systematic differences are visible resulting in χ^2_{red} values higher than 1. Despite the high mass of $\omega(782)$, the relativistic fits perform worse than their non-relativistic counterparts, while the resolution function has only small influence on χ^2_{red}. The mass m_0 of $\omega(782)$ differs by less than 1 MeV/c^2 for the different fits but is about 2 MeV/c^2 higher than the nominal $\omega(782)$ mass. Fig. 3.19 shows the $m_{\pi^-\pi^0\pi^+}$ distribution in the $\mu + p \to \mu\omega + p$ reaction taken with the COMPASS spectrometer analysed in Ref. [32]. Despite the different production mechanism, the analysis measures a somewhat similar mass position, which is higher than the nominal $\omega(782)$ mass. This indicates that the higher $\omega(782)$ mass is a systematic effect of the spectrometer. σ and Γ_0 differ significantly depending on the resolution function. For the double-Gaussian resolution function motivated by simulation Γ_0 is smaller and closer to the nominal value of 8.68 MeV/c^2 [21]. However, the value is still off by about 5 MeV/c^2. This indicates a systematic cause. Therefore, even the double-Gaussian describes the resolution of the detector insufficiently, which leads to a broadening of Γ_0. Fixing Γ_0 to the nominal value worsens the fit significantly. For instance, fixing Γ_0 for the Voigt fit increases χ^2_{red} from 5.0 to 15. The χ^2_{red} values of V and $D_{\text{DG}}^{\text{BW}}$ are almost equal, therefore we use the simpler Voigt distribution V to fit the $\omega(782)$ peak in the following. Since we use the fit to obtain the total peak width, the higher Γ_0 value has negligible impact.

Fig. 3.20 shows the discussed fit of the $m_{\pi^-\pi^0\pi^+}$ distribution with the Voigt distribution V as signal component for the $\omega(782)$ peak, i.e.

$$\frac{dN}{dm}(m; A_\omega, \sigma, m_0, \Gamma_0^{\text{nr}}, \{B_i^\omega\}) = A_\omega V(m; \sigma, m_0, \Gamma_0^{\text{nr}}) + \sum_{i=0}^{2} B_i^\omega m^i, \qquad (3.18)$$

for both 2008 and 2009 data. Table 3.10 lists the relevant parameters obtained from this fit. For 2008 data m_0 is around 0.6 MeV larger and the total width Γ_V is close to 1 MeV/c^2 smaller compared to 2009 data. We require each event to contain exactly one $\pi^-\pi^0\pi^+$ combination that has an invariant mass $m_{\pi^-\pi^0\pi^+}$ in the range $|m_{\pi\pi\pi} - m_\omega| < 3\sigma_\omega$. Here, m_ω is the position and σ_ω is the width

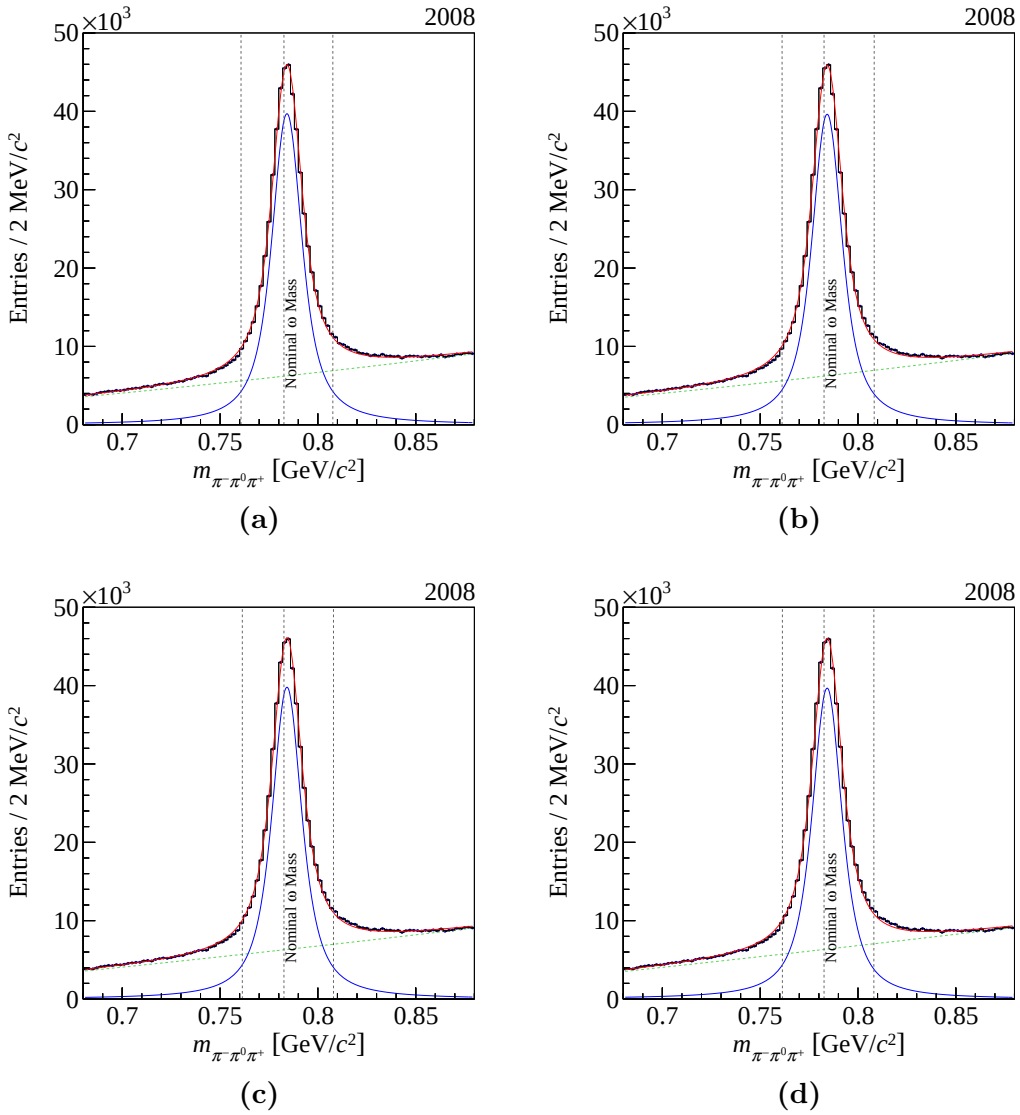

Figure 3.18: $m_{\pi^-\pi^0\pi^+}$ distribution for the 2008 data set. The blue solid curve is the Voigt distribution V in (a), the relativistic Voigt distribution V_{rel} in (b), $D_{\text{DG}}^{\text{BW}}$ (see Eq. (B.13)) in (c), and $D_{\text{DG}}^{\text{BW,rel}}$ (see Eq. (B.14)) in (d). It represents the signal component of $\omega(782)$ in the distribution. The green dashed line shows the polynomial background. The curve in red is the sum of signal and background. The central vertical line indicates the nominal $\omega(782)$ mass, while the outer two vertical lines show the fitted $\omega(782)$ mass $\pm 3\sigma$ of the fitted peak.

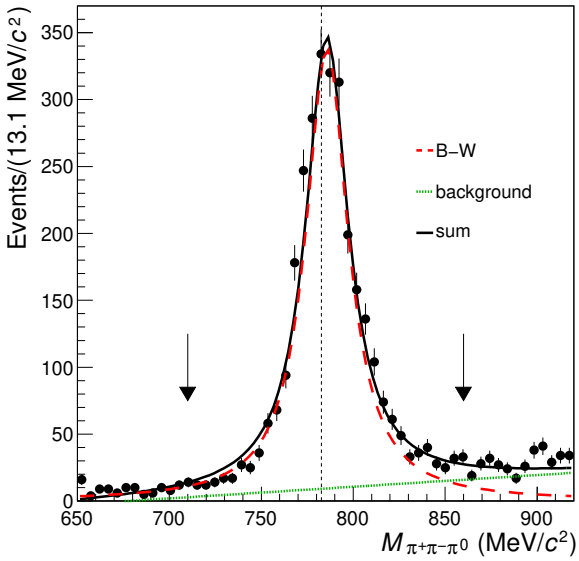

Figure 3.19: $m_{\pi^-\pi^0\pi^+}$ distribution analysed in COMPASS muoproduction [32]. The black curve shows the fitted function. It is the sum of a Breit-Wigner (see Eq. (B.4)) as the signal component (shown as dashed red curve) and a linear polynomial as background component (shown as dotted green curve).

of the $\omega(782)$ peak estimated from the fits. The values of m_ω and σ_ω are listed in Table 3.11 for 2008 and 2009 individually.

3.7 Energy and Momentum Conservation

Events with additional particles that escaped detection may also fulfill our selection cuts. Therefore, we apply cuts on momentum and energy conservation to ensure the selection of exclusive events. Exclusive means that the kinematic properties of all outgoing particles in the event are measured. Momentum conservation requires the momentum $\vec{p}_X$ of the X^- and the momentum $\vec{p}_{\text{recoil}}$ of the recoil proton to be back-to-back in the plane transverse to the beam, i.e. the azimuthal difference

$$\Delta\phi_{\text{RPD}} \equiv \Delta\phi\left(\vec{p}_X^{\,\perp}, \vec{p}_{p_{\text{recoil}}}^{\,\perp}\right) - 180^\circ \tag{3.19}$$

between the projections of $\vec{p}_X$ and $\vec{p}_{\text{recoil}}$ in the plane transverse to the beam direction should be cerntered at 0. The distribution is shown in Fig. 3.21a. We require $\Delta\phi_{\text{RPD}}$ within $\pm\sigma_{\Delta\phi}$, the RPD resolution [33]. The resolution depends on the relative orientation of the hit slabs in ring A and B as shown in Fig. 2.6. If the central slab in ring B is hit $\sigma_{\Delta\phi} = 8.432^\circ$, otherwise $\sigma_{\Delta\phi} = 5.377^\circ$. We require the event to have exactly one measured proton track in the RPD in order to ensure a well-defined recoil proton.

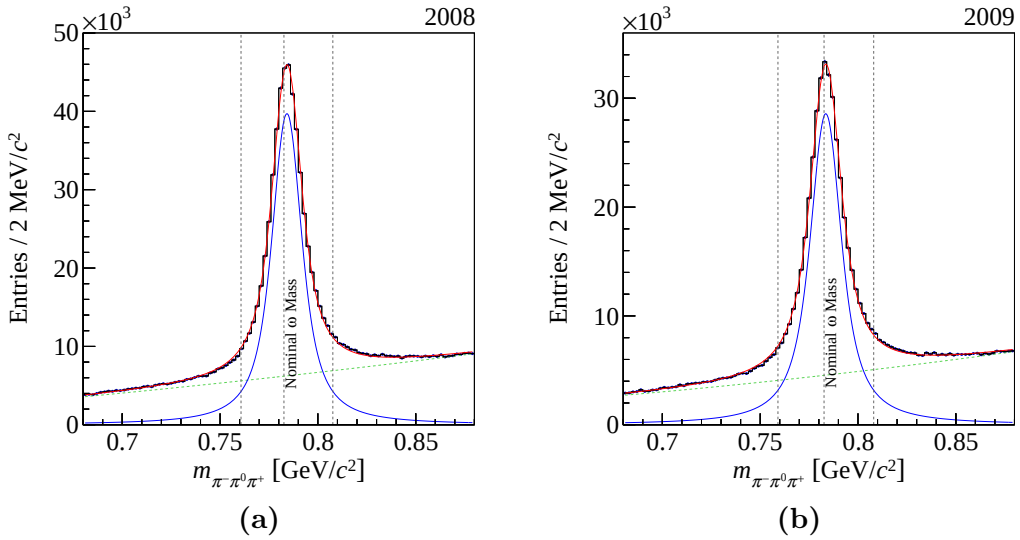

Figure 3.20: $m_{\pi^-\pi^0\pi^+}$ distributions for (a) the 2008 and (b) the 2009 data set. The blue solid curve is the Voigt distribution used as signal. The green dashed line shows the polynomial background. The curve in red is the sum of signal and background (Eq. (3.18)). The central vertical line indicates the nominal $\omega(782)$ mass, while the outer two vertical lines show the selected mass window.

Table 3.10: Fit parameters obtained by fitting Eq. (3.18) to the $m_{\pi^-\pi^0\omega}$ distribution. Γ_V^{rel} and σ_V^{rel} are defined in Appendix B.2. The yields are calculated from in the $\pm 3\sigma_V$ interval around m_0.

Parameters		2008	2009
m_0	[MeV/c^2]	784.18	783.56
σ	[MeV/c^2]	3.63	3.49
Γ_0	[MeV/c^2]	14.23	15.48
χ^2_{red}	(NDF)	5.0 (93)	3.5 (93)
Γ_V^{rel}	[MeV/c^2]	18.42	19.21
σ_V^{rel}	[MeV/c^2]	7.82	8.16
Signal yield		428 202	322 853
Background yield		146 566	111 658

Table 3.11: Cut parameters used for the $\omega(782)$ selection. The values are derived from the fit parameters in Table 3.10.

2008		2009	
m_ω [MeV/c^2]	$3\sigma_\omega$ [MeV/c^2]	m_ω [MeV/c^2]	$3\sigma_\omega$ [MeV/c^2]
784.2	23.5	783.6	24.6

Table 3.12: Parameters obtained by fitting Eq. (3.21) to the E_{beam} distribution in Figs. 3.21b and 3.21c. σ_E is estimated by Eq. (B.3).

R_E	E_0 [GeV]	$\sigma_{1,E}$ [GeV]	$\sigma_{2,E}$ [GeV]	χ^2_{red} (NDF)	σ_E [GeV]
0.045	191.226	3.610	1.960	3.0 (70)	2.034

The spectrometer does not measure the energy E_{beam} of the beam particles, but by applying energy conservation E_{beam} can be calculated from the four-momenta of the final-state particles and the measured inclination of the beam particle in the lab frame. The derivation is given in Appendix A. The E_{beam} distribution is shown in Figs. 3.21b and 3.21c. We fit this distribution with the sum of a double-Gaussian (see Eq. (B.1)), which represents exclusive events, on top of the empirical function

$$\begin{aligned} f_{\text{BG}}(E_{\text{beam}}; a_{1,E}, a_{2,E}, b_E, c_E, \mu_E) = \\ c_E \left[a_{1,E} + \frac{a_{2,E}}{(E_{\text{beam}} - \mu_E)^3} + \frac{1}{(E_{\text{beam}} - \mu_E)^2} \right]^{-1} \\ \times \left\{ \frac{\pi}{2} - \arctan\left[b_E (E_{\text{beam}} - \mu_E) \right] \right\}, \end{aligned} \tag{3.20}$$

which represents the non-exclusive background, i.e.

$$\begin{aligned} \frac{dN}{E_{\text{beam}}}(E_{\text{beam}}; A_E, R_E, E_0, \sigma_{1,E}, \sigma_{2,E}, a_{1,E}, a_{2,E}, b_E, c_E, \mu_E) = \\ A_E D_{\text{G}}(E_{\text{beam}}; R_E, E_0, \sigma_{1,E}, \sigma_{2,E}) \\ + f_{\text{BG}}(E_{\text{beam}}; a_{1,E}, a_{2,E}, b_E, c_E, \mu_E) \end{aligned} \tag{3.21}$$

The fit range is from 150 GeV to 230 GeV. Table 3.12 lists the relevant parameters of the peak obtained by the fit. To ensure energy conservation, E_{beam} must be within $3\sigma_E$ around E_0, i.e. in the range from 185.1 GeV to 197.3 GeV.

3.8 Time Stability

The stability of the π^0 and $\omega(782)$ peak parameters over time are investigated in this chapter. Runs are used as a measure of time[c]. Section 3.8.1 and Section 3.8.2 discuss the time stability of π^0 and $\omega(782)$, respectively, by fitting the peak for every run individually. In Section 3.8.3 cuts on the fit parameters are applied to remove runs with deviating or highly uncertain parameter values. Table D.1 gives a list of all removed runs for both years. The number of

[c] Runs are numbered consecutive in time. Each run is about 2 hours long.

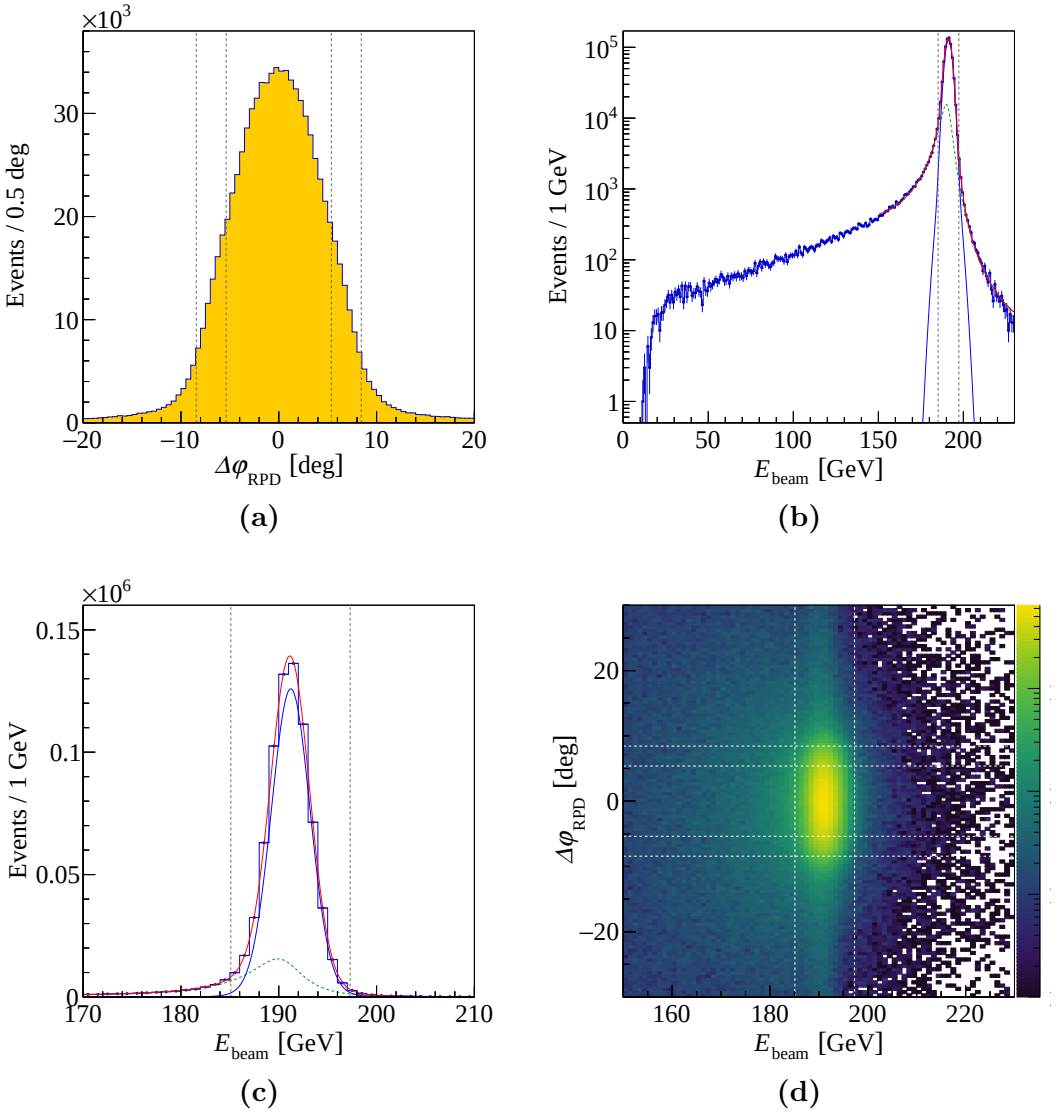

Figure 3.21: (a) shows the $\Delta\phi_{\mathrm{RPD}}$ distribution as defined in Eq. (3.19). (b) and (c) show the E_{beam} distribution in the full range and a zoomed view on the peak region, respectively. The red curve represents the result of fitting Eq. (3.21) to the E_{beam} distribution. The blue solid curve represents the signal component and the green dashed curve shows the background function given by Eq. (3.20). (d) shows the correlation of both quantities. Note the logarithmic color scale. The black and white dashed lines indicate the applied cuts.

excluded events is small. For the 2008 data, 12 303 events are excluded which corresponds to 2.8% of the selected events in 2008 data. For the 2009 data, 4985 events are excluded corresponding to 1.6% of the selected events in 2009 data.

3.8.1 π^0 Time Stability

To investigate the time stability of the reconstructed π^0 mass and π^0 peak width, the π^0 peak in the $m_{\gamma\gamma}$ distribution is fitted for ECAL1 and ECAL2 photon pairs individually. Since single runs contain much less data, we use a simpler fit function as compared to the one used in Section 3.5. Here, we use the sum of a single Gaussian $\mathcal{N}$ for the π^0 signal and a background polynomial of third degree as a fit function, i.e.

$$\frac{dN}{dm}(m; A_\pi, m_{\pi^0}, \sigma_{\pi^0}, \{B_i^\pi\}) = A_\pi \mathcal{N}(m; m_{\pi^0}, \sigma_{\pi^0}) + \sum_{i=0}^{3} B_i^\pi m^i, \tag{3.22}$$

which is fitted in the $m_{\gamma\gamma}$ range from $0.07\,\mathrm{GeV}/c^2$ to $0.2\,\mathrm{GeV}/c^2$. The reconstructed positions and widths of the Gaussian peaks are shown in Figs. 3.22 and 3.23 for ECAL1 photon pairs and in Figs. 3.24 and 3.25 for ECAL2 photon pairs for 2008 and 2009 runs, respectively. Runs, where the fit does not converge (green points), are excluded. For the 2008 data, the parameters for ECAL1 and ECAL2 photon pairs are stable over time with reconstructed π^0 masses less than $1\,\mathrm{GeV}/c^2$ above the nominal mass. The 2009 data were taken in three data-taking periods (W25, W27, and W37), were the runs of each period is grouped into a block in Figs. 3.23 and 3.25. For ECAL1 photon pairs, the peak positions are shifted by approximately $1\,\mathrm{MeV}/c^2$ to smaller values for the last period, while the other periods are close to the nominal π^0 mass. For ECAL2 photon pairs the mass is stable and shifted by less than $1\,\mathrm{MeV}/c^2$ to higher masses, but the widths vary by around $1\,\mathrm{MeV}/c^2$ for the different periods, where the widths were largest during the first and smallest during the last period. This is a systematic effect, which is not corrected, leading to a broadening of the π^0 peak for 2009 data.

3.8.2 $\omega(782)$ Time Stability

To study the stability of the reconstructed $\omega(782)$ over time, we fit Eq. (3.18) in the fit range from $0.68\,\mathrm{GeV}/c^2$ to $0.88\,\mathrm{GeV}/c^2$ to the $m_{\pi^-\pi^0\pi^-}$ distribution. Since single runs contain much less data, we fix the decay width Γ_0^{nr} to the nominal value $8.68\,\mathrm{MeV}/c^2$. Figs. 3.26 and 3.27 show the obtained $\omega(782)$ masses m_ω and widths σ_ω as a function of the run number for the 2008 and 2009 data set, respectively. σ_ω is estimated using Eq. (B.9) and Eq. (B.12).

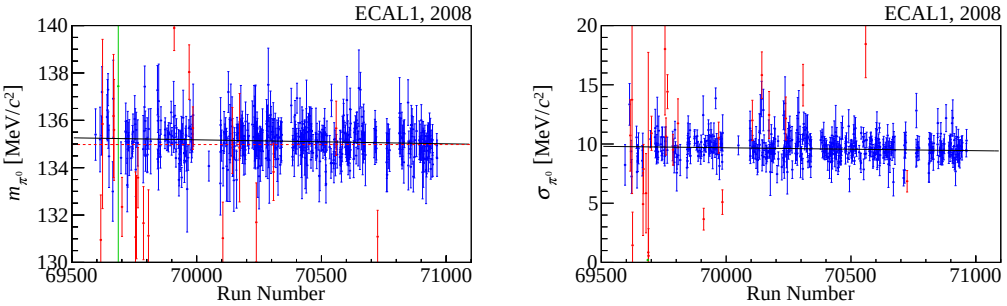

(a) **(b)**

Figure 3.22: (a) Reconstructed π^0 mass and (b) π^0 peak width as a function of the run number for ECAL1 photon pairs for the 2008 data set. The dashed red line indicates the nominal π^0 mass, while the black line is a linear fit to the blue data points, which represent the good runs. The red data points are the runs with deviating fit parameters and the green data points indicate runs, where the fit is not converging. Both cases are tagged as bad runs.

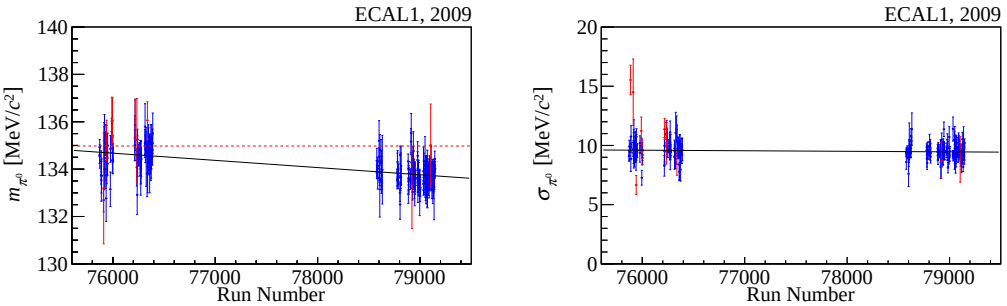

(a) **(b)**

Figure 3.23: Similar to Fig. 3.22 but for the 2009 data set.

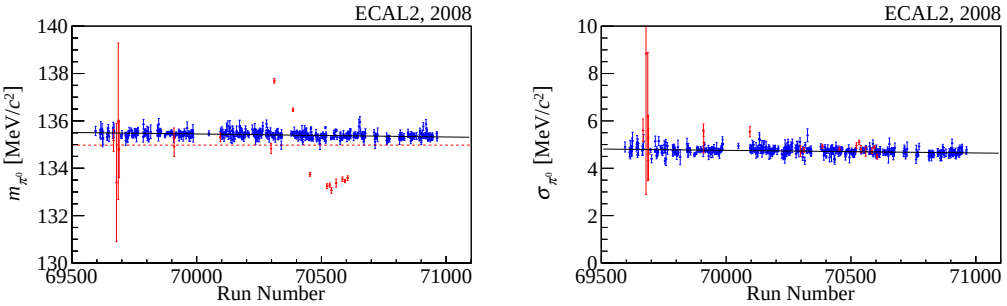

(a) **(b)**

Figure 3.24: Similar to Fig. 3.22 but for ECAL2 photon pairs for the 2008 data set.

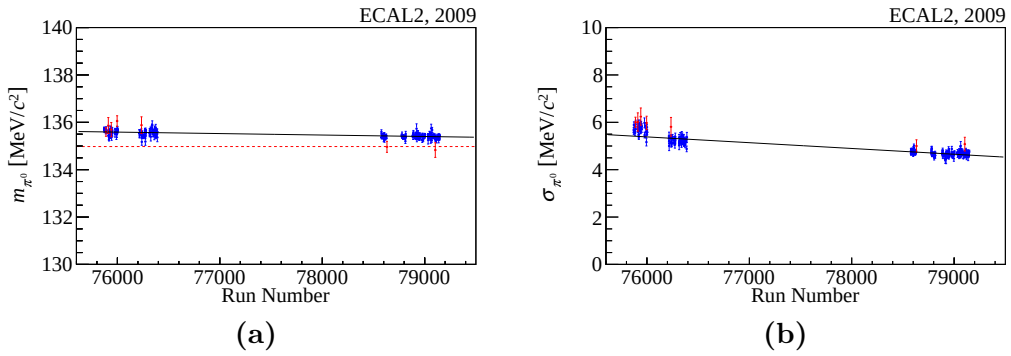

Figure 3.25: Similar to Fig. 3.22 but for ECAL2 photon pairs for the 2009 data set.

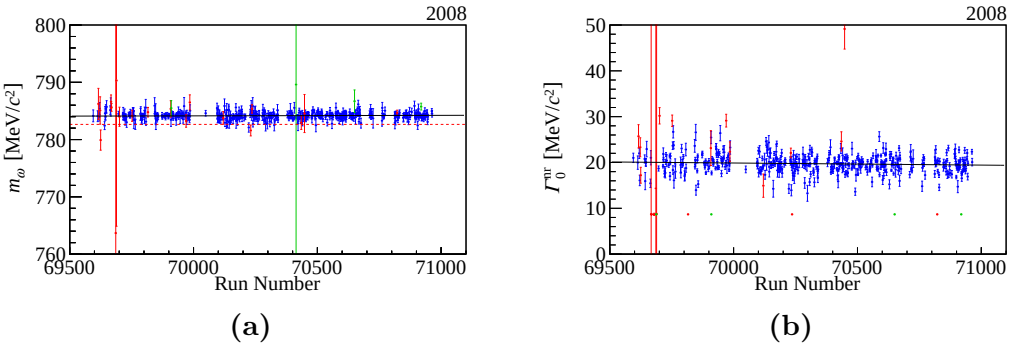

Figure 3.26: (a) $\omega(782)$ mass and (b) $\omega(782)$ peak width as a function of the run number for the 2008 data set. The dashed red line indicates the nominal $\omega(782)$ mass, while the black line is a linear fit to the blue data points, which represent the good runs. The red data points indicate the runs with deviating fit parameters and the green data points are runs, where the fit is not converging. Both cases are tagged as bad runs.

Runs, where the fit does not converge (green points), are excluded. For the 2008 data, both mass and width are stable. However, the measured $\omega(782)$ mass is 1.5 MeV/c^2 higher than the nominal value. For the 2009 data, the $\omega(782)$ mass behaves similarly, but the $\omega(782)$ peak width is different for the periods of data taking. The last two periods of runs yield a peak width compatible with 2008, while the first period has a width approximately 15 MeV/c^2 higher. This is a similar behaviour as observed for the π^0 peak in Section 3.8.1, which also broadens the $\omega(782)$ peak for 2009 data.

3.8.3 Fit Parameter Cuts

Figs. 3.28 and 3.29 show the distributions of the π^0 and $\omega(782)$ mass parameters and their corresponding uncertainties for the runs in 2008 and 2009, respectively.

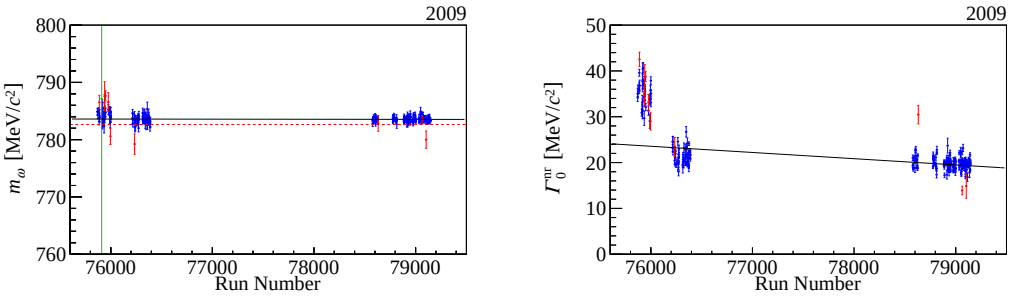

Figure 3.27: Similar to Fig. 3.26 but for the 2009 data set.

Figs. 3.30 and 3.31 show the distributions of the π^0 and $\omega(782)$ width parameters and their corresponding uncertainties for the runs in 2008 and 2009, respectively. Runs, for which at least one parameter lies outside the peak region indicated by the vertical dashed lines are excluded. We choose the ranges of these regions by separating the peak region from deviating entries.

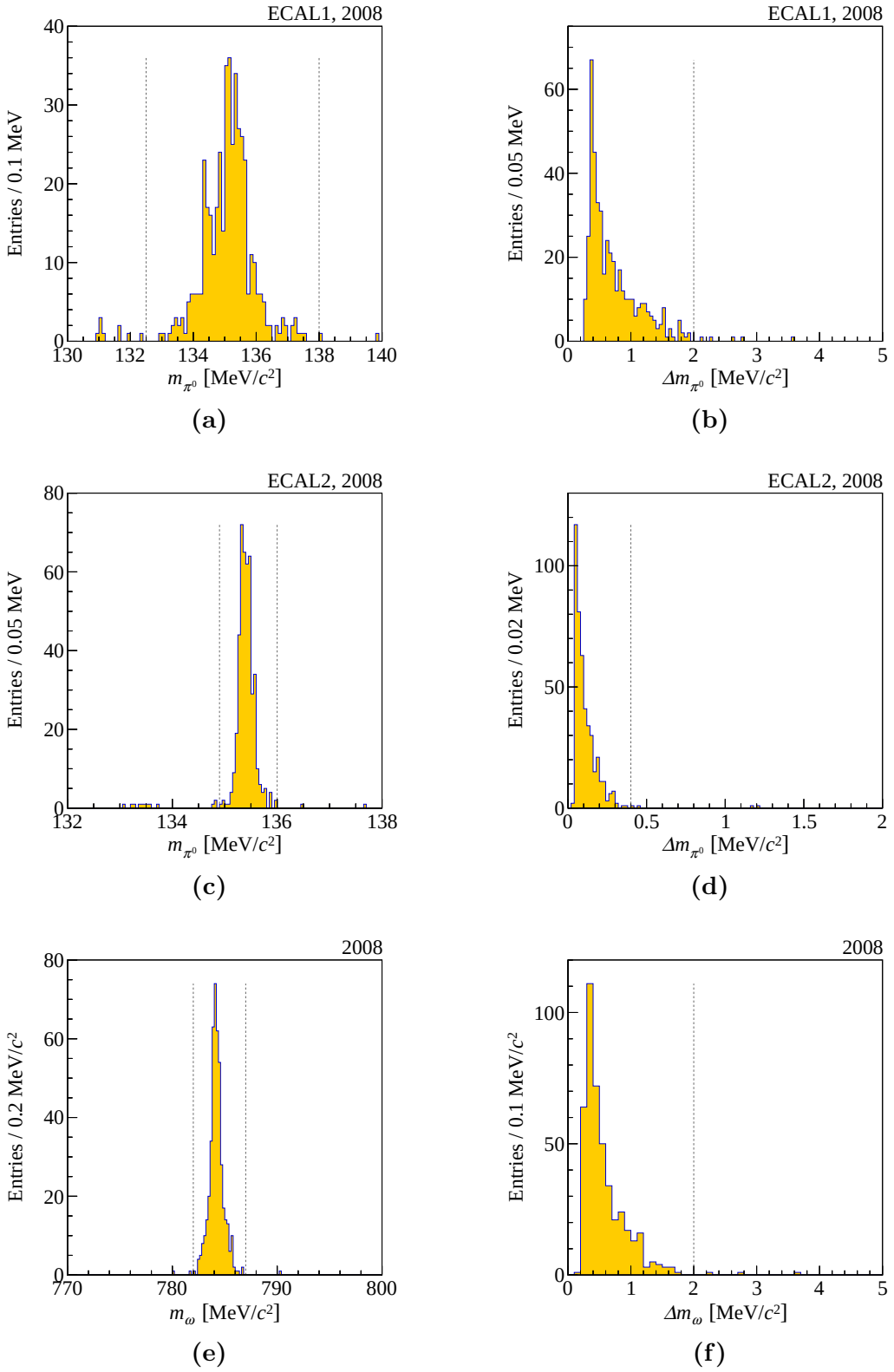

Figure 3.28: Distributions of (a) and (c) the mass and (b) and (d) the mass uncertainty of the π^0 fit for the ECAL1, and the ECAL2 photon-pair cases in the first and second row, respectively. Distributions of (e) the mass and (f) the mass uncertainty of the $\omega(782)$ fit. Each run in 2008 is fitted separately. The dashed lines indicate the applied cuts.

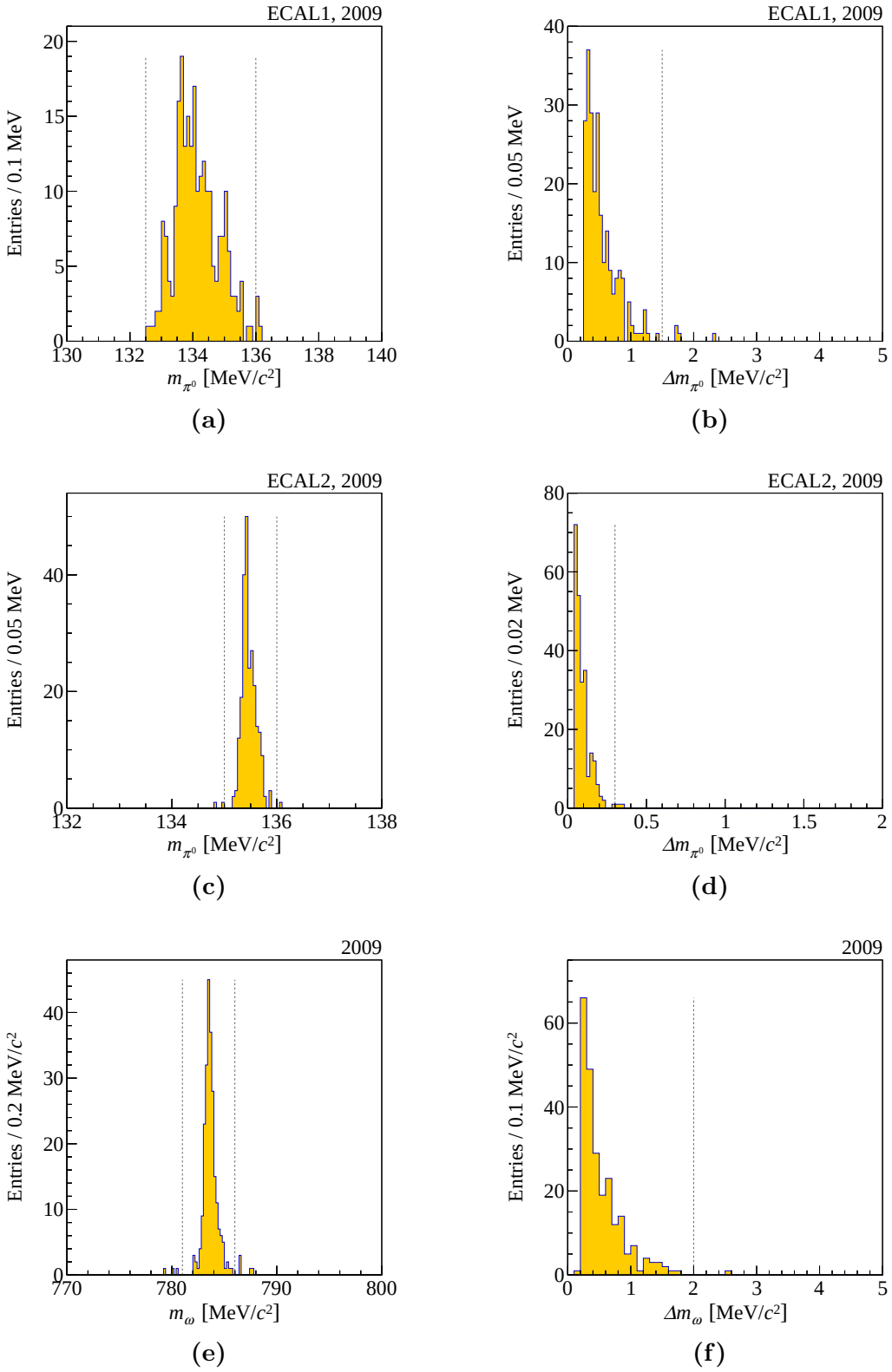

Figure 3.29: Similar to Fig. 3.28 but for runs in 2009.

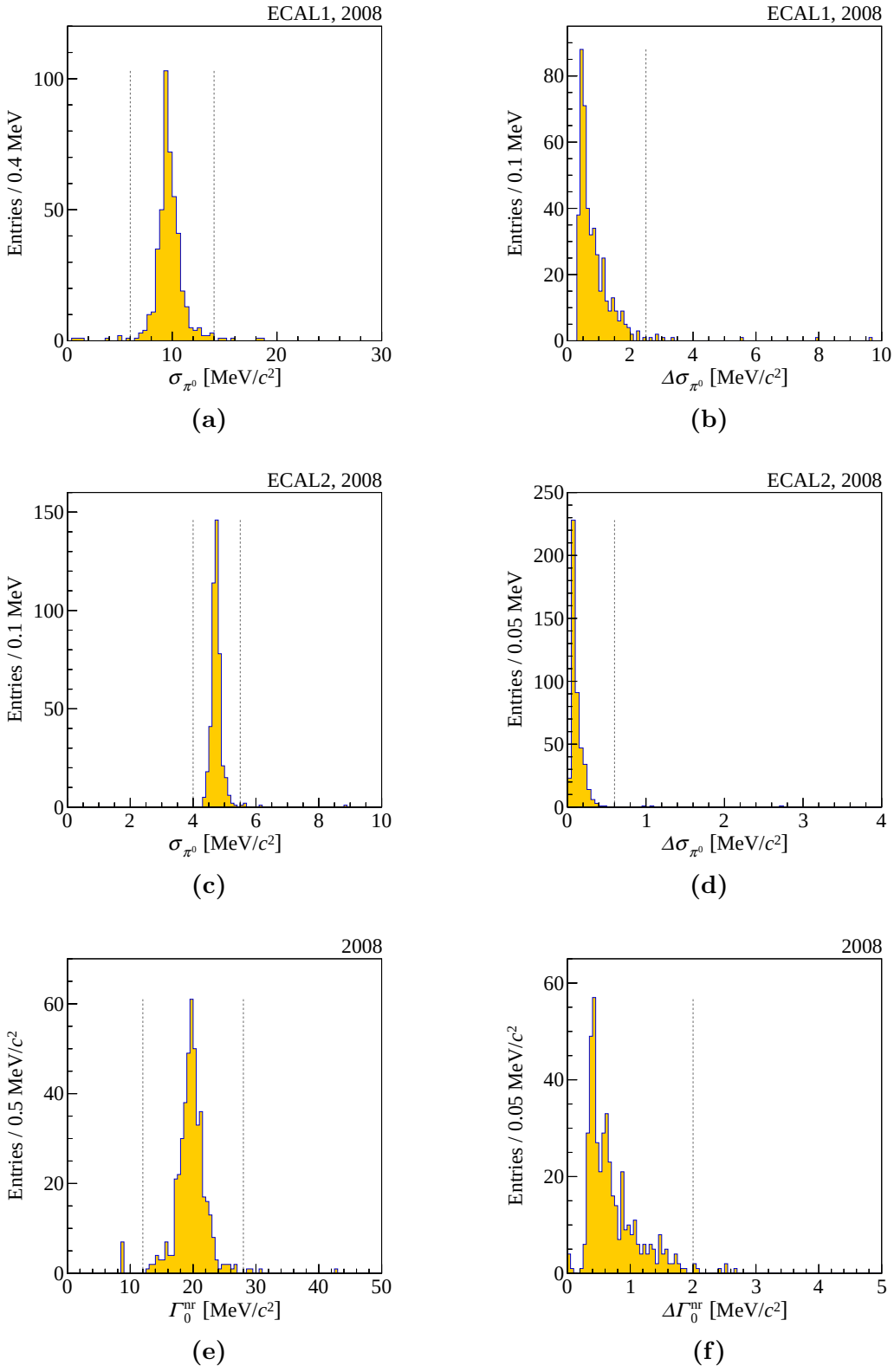

Figure 3.30: Distributions of (a) and (c) the widths and (b) and (d) the width uncertainties of the π^0 fit for the ECAL1, and the ECAL2 photon-pair cases in the first and second row, respectively. Distributions of (e) the width and (f) the width uncertainty of the $\omega(782)$ fit. Each run in 2008 is fitted separately. The dashed lines indicate the applied cuts.

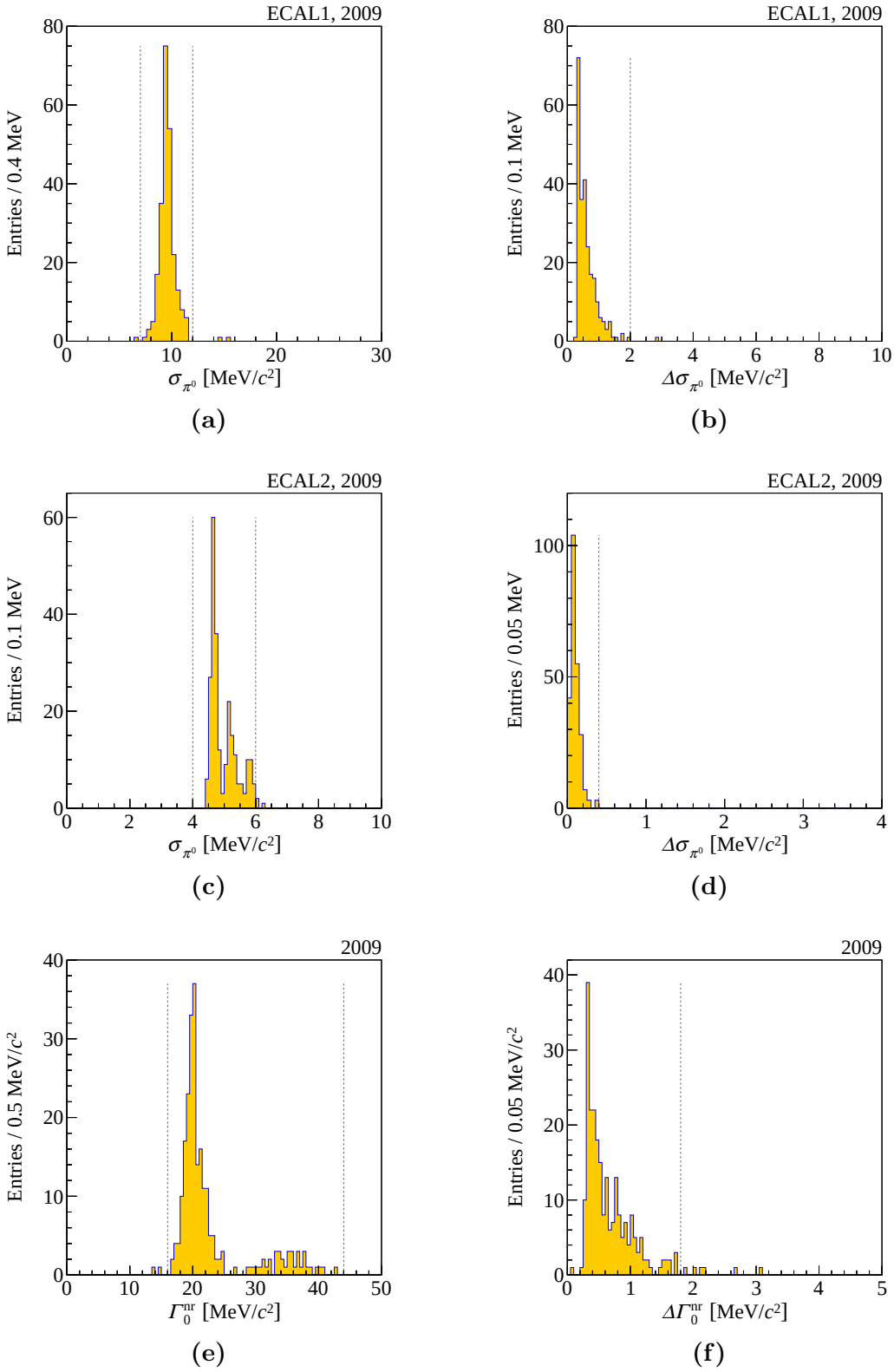

Figure 3.31: Similar to Fig. 3.30 but for runs in 2009.

3.9 Analyzed Kinematic Range

3.9.1 Squared Four-Momentum Transfer

An important kinematic variable that describes the scattering process is the squared four-momentum t that is transferred from the beam particle to the recoil particle. For a precise measurement of this the quantity we use the four-momentum difference between the beam pion and the produced intermediate state X^{-}[d], i.e.

$$t = (p_{\text{beam}} - p_X)^2 = m_\pi^2 + m_X^2 - E_{\text{beam}}E_X + 2|\vec{p}_{\text{beam}}||\vec{p}_X|\cos\theta, \tag{3.23}$$

where $\vec{p}_X$ is the sum of the four-momenta of all final-state particles and θ is the angle between $\vec{p}_{\text{beam}}$ and $\vec{p}_X$. We only consider $t < 0$ for the scattering reaction. The minimal magnitude of the squared four-momentum transfer in the center-of-mass system is

$$|t|_{\text{min}} = 2(E_{\text{beam}}^{\text{CM}}E_X^{\text{CM}} + \vec{p}_{\text{beam}}^{\text{CM}}\vec{p}_X^{\text{CM}}) - m_\pi^2 - m_X^2, \tag{3.24}$$

which is the squared four-momentum transfer that is at least needed to create a state X with $m_X > m_\pi$. Using Eq. (3.24) we define the reduced squared four-momentum transfer

$$t' = |t| - |t|_{\text{min}}, \tag{3.25}$$

which is positive definit. Fig. 3.32 shows the measured t' distribution. The acceptance of the RPD is only sensitive for $|t| > 0.07\,(\text{GeV}/c)^2$. Therefore, we require $t' > 0.1\,(\text{GeV}/c)^2$ to ensure a close to constant acceptance. For $t' \gtrsim 0.1\,(\text{GeV}/c)^2$, the t' distribution decreases approximately exponentially. As a consequence there are only few events for $t' > 1.0\,(\text{GeV}/c)^2$, which we exclude from the analysis. We fit the sum of two exponential functions, i.e.

$$\frac{dN}{dt'}(t'; b_1, r, b_2) = A(e^{-b_1 t'} + re^{-b_2 t'}), \tag{3.26}$$

to the distribution in Fig. 3.32 and obtain slope values of $b_1 = 3.56\,(\text{GeV}/c)^{-2}$ and $b_2 = 7.04\,(\text{GeV}/c)^{-2}$ using a fit range from $0.1\,(\text{GeV}/c)^2$ to $1.0\,(\text{GeV}/c)^2$.

3.9.2 Total Mass of the $\pi^-\pi^0\omega(782)$ System

Fig. 3.33 shows the distribution of the total invariant mass $m_{\pi^-\pi^0\omega}$ of the $\pi^-\pi^0\omega(782)$ system. The spectrum starts at around $1.2\,\text{GeV}/c^2$ and has a long tail that reaches masses beyond $5\,\text{GeV}/c^2$. We observe a clear peak in the mass

[d] We do not use the measured momentum of the scattered proton as the resolution of the RPD is inferior compared to the forward spectrometer.

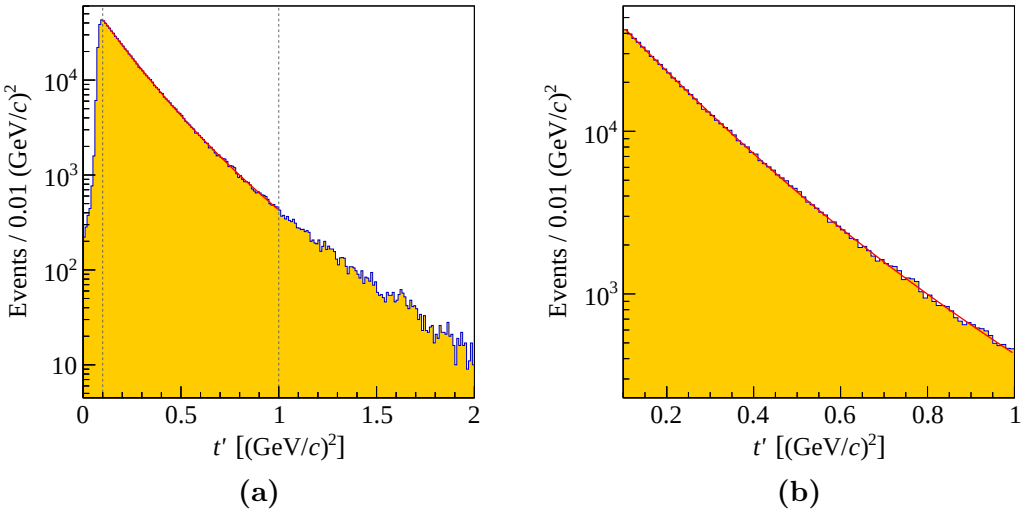

Figure 3.32: Distribution of the reduced four-momentum transfer t' for (a) a wide range and (b) the selected region of interest. The dashed lines in (a) indicate the applied cut.

region of the $a_2(1320)$. Around $1.9\,\mathrm{GeV}/c^2$ a broad peak appears that could be caused by several known resonances. Since the presented event selection will serve as input for the partial-wave analysis, we select events with $m_{\pi^-\pi^0\omega}$ up to $3.5\,\mathrm{GeV}/c^2$. For masses beyond this limit no resonances are expected. The phase-space acceptance η_{PS}[a] shows a smooth function with a significant rise towards higher masses. This may slightly shift the observed peaks towards higher masses.

3.10 Summary

The event selection presented in this chapter yields a clean data sample of 730 000 exclusive events for the diffractive process $\pi^- + p \to \pi^-\pi^0\omega(782) + p$ shown in Fig. 3.1. Table 3.13 lists the number of events passing the cuts that are applied in the final selection. Fig. 3.34 shows the number of events passing the cuts including the preselection listed in Table 3.1.

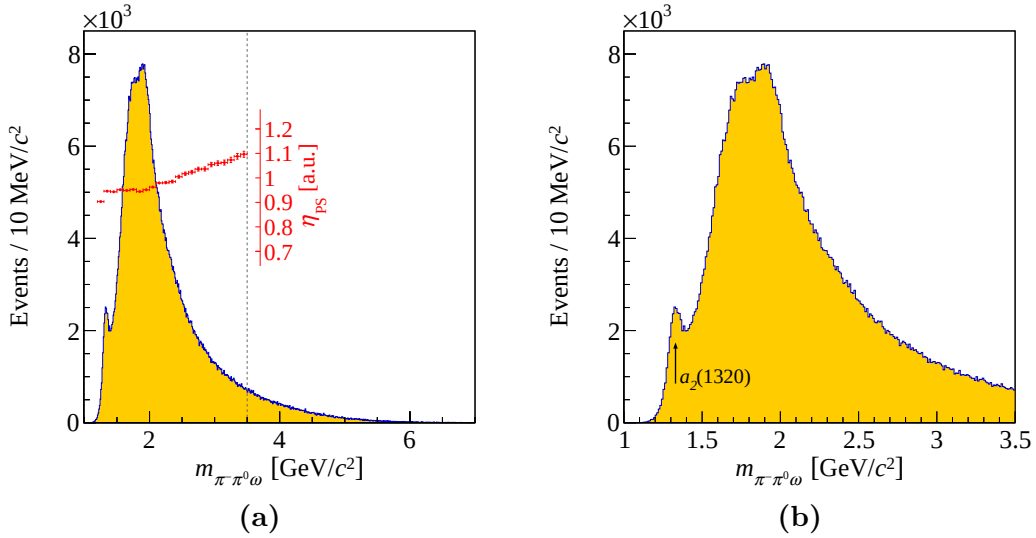

Figure 3.33: Distribution of the invariant mass of the $\pi^-\pi^0\omega$ system for (a) a wide range and (b) for the selected region of interest. The dashed line in (a) indicates the applied cut.

Table 3.13: List of Cuts applied in the final event selection with the corresponding number of events passing the given cut for 2008 and 2009, respectively. The cuts written in blue are not enabled in studies of $m_{\gamma\gamma}$.

Cuts	Section	2008	2009
Preselected events (see Table 3.1)	3.1	307 492 130	247 231 722
$-66\,\text{cm} < z_{\text{vertex}} < -29\,\text{cm}$	3.2	286 186 023	229 725 418
$R_{\text{vertex}} < 1.55\,\text{cm}$	3.2	284 507 679	226 152 520
T_{beam} within $3\sigma_T$	3.2	274 781 439	221 228 152
CEDAR Beam ID is pion	3.2	265 110 533	210 773 740
RICH kaon veto	3.3	248 184 863	198 405 389
Exactly four photons	3.4	40 463 242	30 620 472
Exactly one π^0 pair	3.5	6 858 355	5 240 801
Exactly one $\omega(782)$ candidate	3.6	1 189 477	938 194
Exactly one RPD proton track	3.7	1 002 807	757 195
RPD planarity	3.7	604 491	444 029
E_{beam} within $3\sigma_E$	3.7	545 043	399 586
Good run	3.8	529 061	393 273
$0.1\,(\text{GeV}/c)^2 < t' < 1.0\,(\text{GeV}/c)^2$	3.9.1	453 143	335 828
$1.0\,\text{GeV}/c^2 < m_{\pi^-\pi^0\omega} < 3.5\,\text{GeV}/c^2$	3.9.2	420 710	312 683

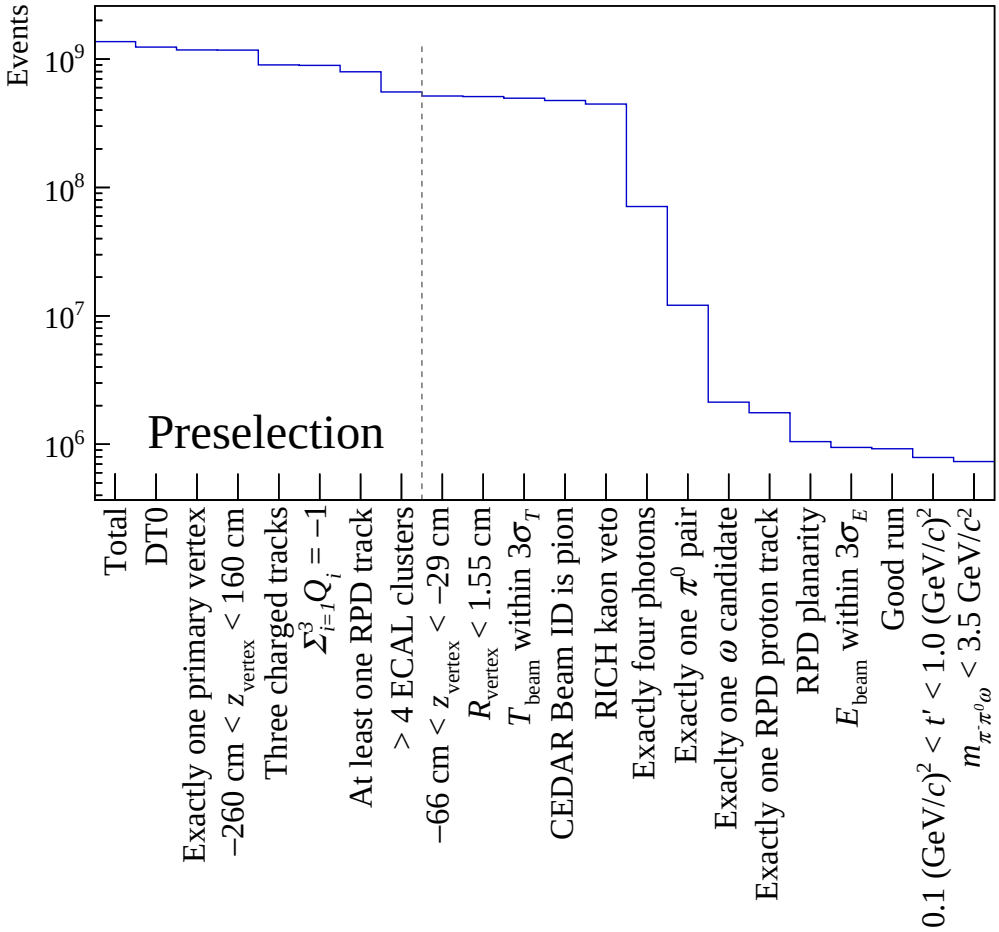

Figure 3.34: Number of events passing the applied cuts for the total data sample.

Chapter 4

Selected $\pi^-\pi^0\omega(782)$ Sample

The $\pi^-\pi^0\omega(782)$ sample selected in Chapter 3 makes a partial-wave analysis possible to fully study the intermediate states within this channel. A partial-wave analysis is beyond the scope of this thesis, however this chapter presents a study of the sample based on kinematic distributions. In Section 4.1 the invariant mass distributions of subsystems is studied. Section 4.2 investigates the $m_{\pi^-\pi^0\omega}$ distribution in correlation to phase-space variables. In Section 4.3 the $\omega(782)$ decay is further studied. For all distributions in this chapter all cuts listed in Tables 3.1 and 3.13 are applied.

4.1 Invariant Mass Distributions of Subsystems

In the $m_{\pi\pi\omega}$ distribution discussed in Section 3.9.2 only the $a_2(1320)$ is visible, while the remaining distribution cannot be directly untangled in distinct resonances. However, we expect not only resoncances in the three-body system, but also in the two-body subsystems. The two $\pi\omega$ subsystems are isospin symmetric with $I^G = 1^+$ quantum numbers. Therefore, we expect b and ρ resonances in two similar distributions, which only differ due to acceptance effects. The PDG [21] lists the $b_1(1235)$ and $\rho(1450)$, $\rho(1700)$ and $\rho_3(1690)$ as established states for b and ρ mesons, respectively. Figs. 4.1a and 4.1b show the measured mass spectra for the $\pi\omega$ subsystems. As expected, both distributions are similar and show a broad peak containing the $b_1(1235)$ resonance. The ρ resonances are not visible as clear peaks, but in the region of $\rho(1700)$ and $\rho_3(1690)$ the distributions decrease slower, which might be caused by contributions of $\rho(1700)$ and $\rho_3(1690)$.

For the bachelor $\pi^-\pi^0$ subsystem, i.e. the subsystem of the two pions that are not part of the $\pi^-\pi^0\pi^+$ combination selected as the $\omega(782)$ candidate, the G-parity is equal to $+1$. The Clebsch-Gordan coefficients [34] of the isospin coupling for $|\pi^-\rangle = |1,-1\rangle$ and $|\pi^0\rangle = |1,0\rangle$ only allow $I = 1, 2$. Since $I = 2$ is not allowed for a $q\bar{q}$ system, i.e. a non-exotic meson, we expect to see only $I = 1$

states. Since $G = (-1)^{L+S+I}$ and the spin $S = 0$ for two spinless particles, only odd L are allowed as relative orbital angular momentum between the two pions. In summary, we expect only to see states with quantum numbers $I^G J^P = 1^+(\text{odd})^-$, which corresponds to the ρ meson sector. Fig. 4.1c shows the mass distribution of the bachelor $\pi^-\pi^0$ subsystem, which contains a clear $\rho(770)$ peak. Around $1.7\text{GeV}/c^2$ a small enhancement appears, which may contain contributions of $\rho(1700)$ and $\rho_3(1690)$.

In Figs. 4.1a to 4.1c the phase-space acceptances η_{PS}[a] are smooth without discontinuous jumps. However, all acceptances increase significantly towards higher masses. This may result in small shifts of the peaks observed in the distributions towards higher masses. Furthermore, the acceptances in $m_{\pi^-\omega}$ and $m_{\pi^0\omega}$ differ at low invariant masses. While the acceptance in $m_{\pi^-\omega}$ increases for decreasing $m_{\pi^-\omega}$ values below about $1.1\,\text{GeV}/c^2$, the acceptance in $m_{\pi^0\omega}$ further decreases.

Next, we look at the invariant masses of the four possible $\pi^-\pi^0\pi^+$ combinations before selecting an $\omega(782)$ candidate from the $\pi^-\pi^-\pi^0\pi^0\pi^+$ final state, i.e. the $\omega(782)$ cut is not applied. We expect a clear $\omega(782)$ peak. Fig. 4.1d shows the $m_{\pi^-\pi^0\pi^+}$ distribution. The spectrum has a smooth, broad background component reaching from about $0.5\,\text{GeV}/c^2$ to invariant masses beyond $2.0\,\text{GeV}/c^2$. On top of it we observe the expected sharp $\omega(782)$ peak at a mass little below $800\,\text{MeV}/c^2$. At about $550\,\text{MeV}/c^2$, a small enhancement indicates contributions from misidentified final states containing η like $\eta\pi^-$ or $\eta\pi^0\pi^0\pi^-$. This is most likely caused by missing or additional photons leading to misidentified π^0. At about $1.3\,\text{GeV}/c^2$, an enhancement indicates contributions of the $a_2(1320)$ from the $\pi^-\pi^0 a_2(1320)$ channel.

For the $\pi^-\pi^-\pi^0\pi^0\pi^+$ final state further two-body systems exist. For all of these $\pi\pi$ systems two different pion-combination cases are possible. While at least one pion is part of the $\pi^-\pi^0\pi^+$ system selected as the $\omega(782)$ candidate, the second pion is either a bachelor pion or part of the $\omega(782)$ candidate. For the $\pi\pi$ subsystems of the $\omega(782)$ $I = 1$. Since the lowest lying $I = 1$ $\pi\pi$ state is $\rho(770)$, only the low mass tail contributes to a $\rho\pi$ resonance within $\omega(782)$ and therefore we expect no visible $\pi\pi$ resonances for pions within $\omega(782)$. Furthermore, due to isospin symmetry we expect similar $m_{\pi\pi}$ distributions for all three combinations. Fig. 4.2c shows the measured $m_{\pi\pi}$ distributions, which agree with the expectation. For the $\pi\pi$ combination of a bachelor pion with a pion within the $\omega(782)$ candidate we expect no resonances assuming no final-state interaction for signal events. However, for background events resonances are possible. Resonances in $\pi^-\pi^-$ are only possible for flavour-exotic mesons, which have not been observed, and therefore we expect no resonances in background contributions for this combination. For the $\pi^0\pi^0$ state only f mesons are allowed. Since their contributions are only small, we expect no visible resonance in background contributions. For the remaining

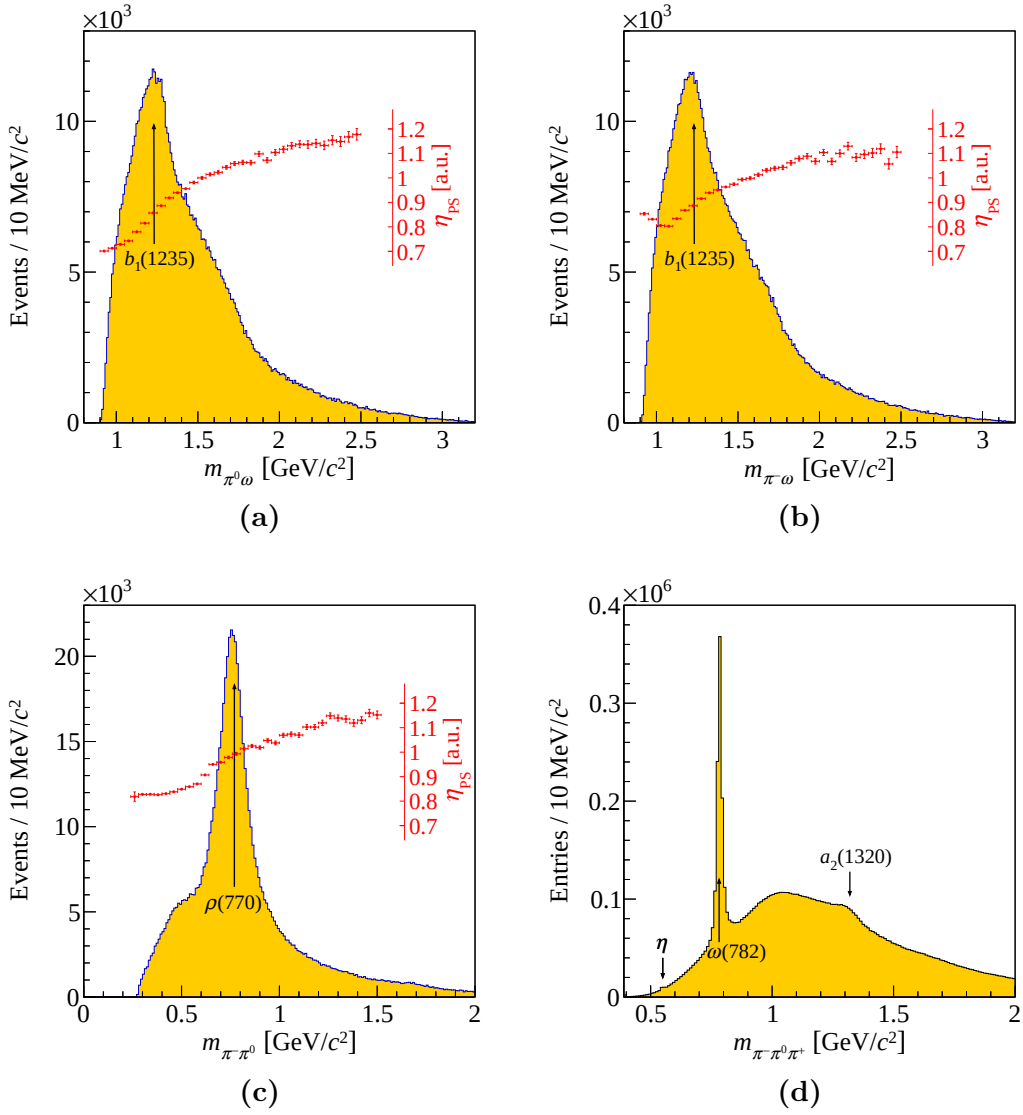

Figure 4.1: Distributions of subsystem masses in the $\pi^-\pi^0\omega$ system. (a) to (c) show the invariant masses of the $\pi^0\omega$, the $\pi^-\omega$, and the $\pi^-\pi^0$ subsystem in $\pi^-\pi^0\omega$, respectively. The red data points represent the relative phase-space acceptances. (d) shows the invariant mass distribution of all $\pi^-\pi^0\pi^+$ combinations (4 entries per event) before the $\omega(782)$ selection, i.e. without the $\omega(782)$ cut (see Section 3.6).

combinations $\pi^-\pi^0$, $\pi^-\pi^+$, and $\pi^0\pi^+$ a possible background resonance is the $\rho(770)$. Figs. 4.2a and 4.2b show $m_{\pi\pi}$ for all combinations. As expected, $\pi^-\pi^-$ and $\pi^0\pi^0$ show no resonances and have a similar distribution. Small differences in the shape may result from acceptance effects for $\pi^0\pi^0$. For the other combinations a enhancement around $750\,\mathrm{MeV}/c^2$ is visible, which suggests a $\rho(770)$ resonance in the background events.

Fig. 4.3 shows Dalitz plots for three different ranges of $m_{\pi^-\pi^0\omega}$. Dalitz plots are commonly used to analyze the kinematics of three-body decays [35]. They show the correlation of the squared invariant masses of two two-particle subsystems. Since the squared invariant mass of the third two-particle subsystem is related by four-momentum conservation, it appears in these plots on the diagonal. If no two-body resonances are part of the three-body decay, we expect a flat distribution with diffuse edges due to the finite $m_{\pi^-\pi^0\omega}$ range. For all $m_{\pi^-\pi^0\omega}$ ranges the Dalitz plots show a horizontal band at $m_{\pi^-\pi^0} \approx 600\,(\mathrm{GeV}/c^2)^2$ corresponding to the $\rho(770)$. Fig. 4.3b and especially Fig. 4.3c show in addition a vertical and a diagonal band for the $\pi^0\omega$ and $\pi^-\omega$ subsystems, respectively. These originate mostly from the $b_1(1235)$, which is also seen in Figs. 4.1a and 4.1b.

To check the features and the quality of the obtained data set for the reaction $\pi^0 + p \to \pi^-\pi^0\omega + p$, we compare it in Fig. 4.4 to the data sample of 145 148 events gathered by the BNL E852 experiment at a lower beam momentum of $18\,\mathrm{GeV}/c$ [12]. The E852 analysis does not reject events with multiple $\omega(782)$ candidates like it is done in this analysis. Instead, for those events the $\omega(782)$ candidate is selected randomly. For the COMPASS and E852 data sets around 15% and 26% of the events, respectively, have more than one $\omega(782)$ candidate. Since E852 applied a cut selecting events with $m_{\pi^-\pi^0\omega}$ below $2.3\,\mathrm{GeV}/c^2$, the same cut is also applied to the COMPASS data to enhance the comparability. Due to the different beam energy and the different event selection, we expect only qualitative agreement. Furthermore, the acceptances of the two experimental setups differ and the shown distributions are not corrected for acceptance effects. The $a_2(1320)$ peak in the $m_{\pi^-\pi^0\omega}$ distribution (see Fig. 4.4a) is slightly shifted to higher masses in the E852 data, while the broad maximum around $1.9\,\mathrm{GeV}/c^2$ is shifted by about $200\,\mathrm{MeV}/c^2$ to lower masses. The latter could be an acceptance effect. For the $\pi^0\omega$ system shown in Fig. 4.4b, both data exhibit a similar $b_1(1235)$ peak at similar mass. However, the peak is more pronounced in the COMPASS data. Fig. 4.4c shows the $m_{\pi^-\pi^0}$ distribution. A clear $\rho(770)$ peak is visible for both experiments. However, the peak in the E852 data is shifted slightly to lower masses and less pronounced. In the $m_{\pi^-\pi^0\pi^+}$ distribution of all four possible $\pi^-\pi^0\pi^+$ combinations in the $\pi^-\pi^-\pi^0\pi^0\pi^+$ final state before the $\omega(782)$ selection, which is shown in Fig. 4.4d, both analyses find a clear $\omega(782)$ peak. However, for the COMPASS data the signal to background ratio is significantly higher. Compared to Fig. 4.1d, the bump of $a_2(1320)$ is less pronounced in the COMPASS data after introducing the cut on $m_{\pi^-\pi^0\omega}$.

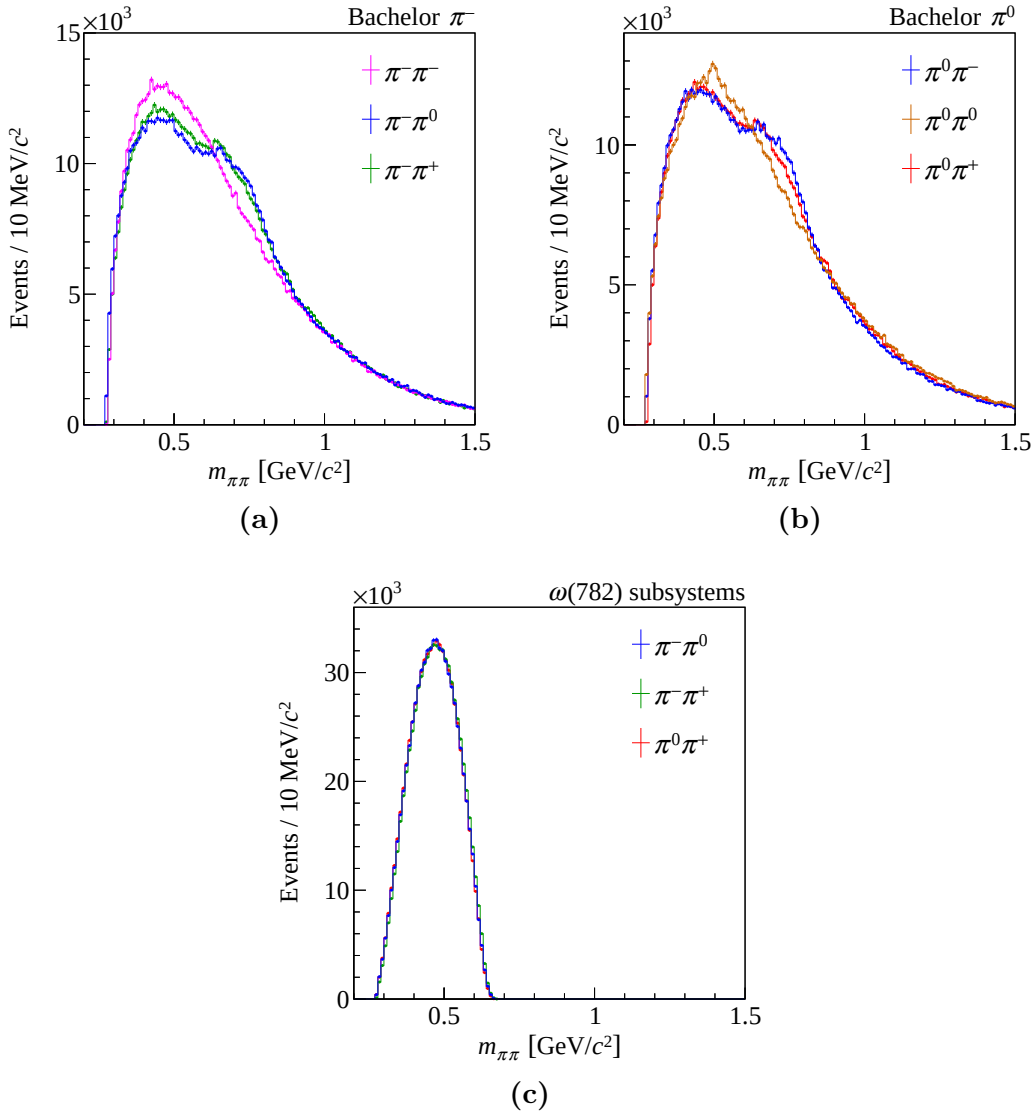

Figure 4.2: Distributions of the invariant masses of two-pion subsystems in the $\pi^-\pi^-\pi^0\pi^0\pi^+$ final state. (a) and (b) show the invariant mass distributions for all combinations of bachelor π^- and π^0, respectively, with one of the three pions in the selected $\omega(782)$ candidate. (c) shows the invariant mass distributions of two-pion combinations within the $\pi^-\pi^0\pi^+$ subsystem of the selected $\omega(782)$ candidate.

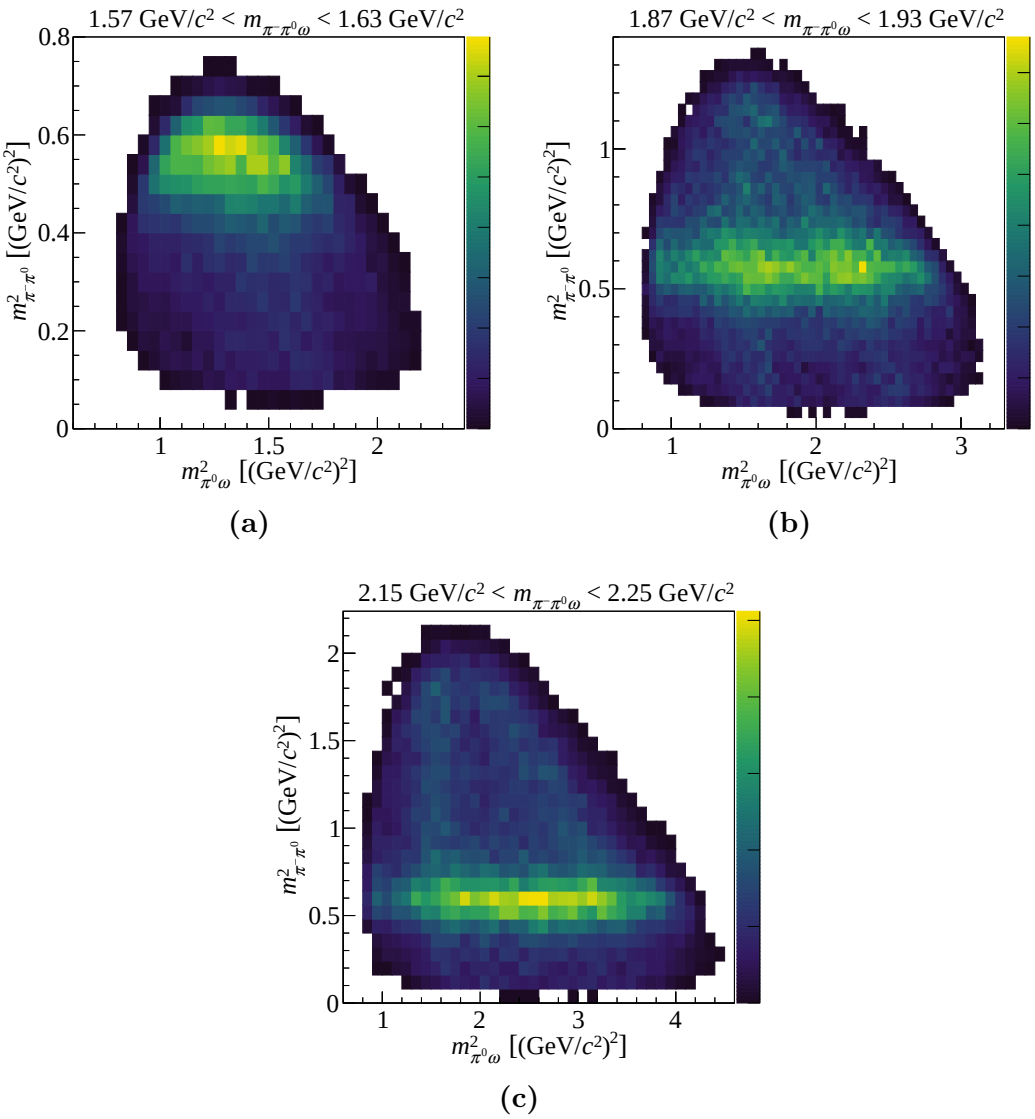

Figure 4.3: Dalitz plots for the $\pi^-\pi^0\omega$ final state for three $m_{\pi^-\pi^0\omega}$ regions ((a) $1.57\,\mathrm{GeV}/c^2 < m_{\pi^-\pi^0\omega} < 1.63\,\mathrm{GeV}/c^2$, (b) $1.87\,\mathrm{GeV}/c^2 < m_{\pi^-\pi^0\omega} < 1.93\,\mathrm{GeV}/c^2$, and (c) $2.15\,\mathrm{GeV}/c^2 < m_{\pi^-\pi^0\omega} < 2.25\,\mathrm{GeV}/c^2$).

Therefore, an intermediate state X^- decaying into $\pi^-\pi^0 a_2(1320)$ must have a mass close to or above $2.3\,\mathrm{GeV}/c^2$. All COMPASS distributions have higher precision than corresponding E852 distributions due to the about 5.1 times larger data sample.

4.2 Angular Distributions

Studying angular distributions of the $\pi^-\pi^0\omega$ system gives insight into the quantum numbers of the contributing decay amplitudes of X and the subsystems of X. Since the contributing amplitudes depend on the mass, we investigate

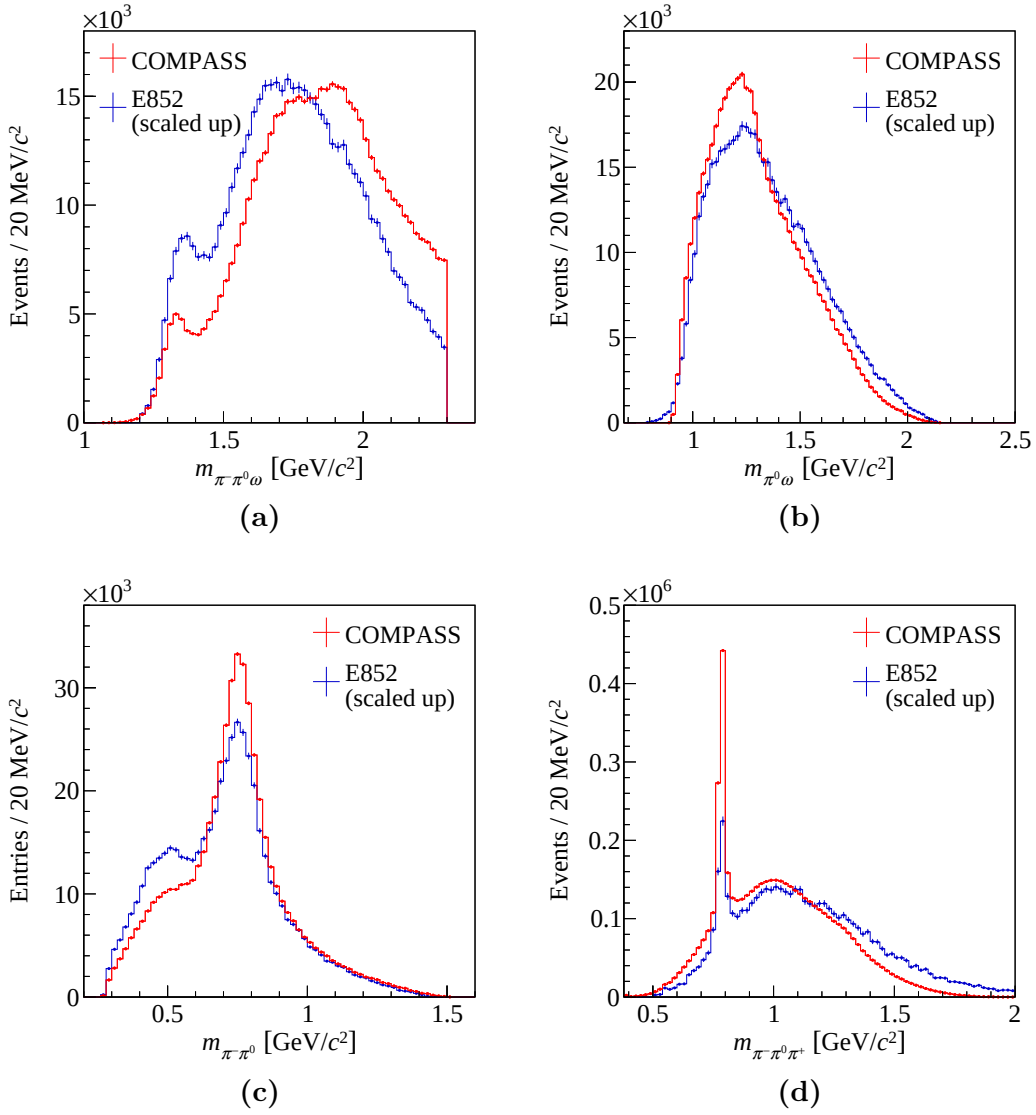

Figure 4.4: Comparison of kinematic distributions obtained by COMPASS (red) and by BNL E852 (blue). (a), (b) and (c) show the invariant mass of the $\pi^-\pi^0\omega$, $\pi^0\omega$, and $\pi^-\pi^0$ systems, respectively. (d) shows the invariant mass for all combinations (4 entries per event) of the $\pi^-\pi^0\pi^+$ subsystem without the $\omega(782)$ cut. The distributions for E852 data are digitized from Ref. [12] and scaled to the number of COMPASS events in the range $m_{\pi^-\pi^0\omega} < 2.3\,\mathrm{GeV}/c^2$.

the correlation between angular distributions and the $m_{\pi^-\pi^0\omega}$ distribution. The kinematics of a three-particle decay is completely defined by six variables. One possible set of variables consists of $m_{\pi^-\pi^0\omega}$, the mass of a two-particle subsystem and four phase-space angles. In the isobar model [36, 37], the decay of X^- is described as a chain of successive two-body decays. The unstable intermediate states within this decay chain are called isobars. Each isobar describes a two-body decay. In the case of the $X^- \to \pi^-\pi^0\omega$ decay only one two-body isobar ξ exists within the decay chain. However, there are three possible two-body subsystems, in which isobar resonances may appear: $\pi^-\pi^0$, $\pi^-\omega$, and $\pi^0\omega$. As discussed in Section 4.1, these two-body subsystems indeed contain resonances, which motivates this approach of factorizing the decay into a chain of two-body decays.

Two right-handed coordinate systems are used to define the four phase-space angles. The first coordinate system is in the rest frame of X and is called Gottfried-Jackson (GJ) frame [38]. The direction of the beam defines z_{GJ}. The y_{GJ} axis is defined as the normal to the production plane, i.e. $\hat{y}_{\text{GJ}} \propto \hat{p}^{\text{lab}}_{\text{beam}} \times \hat{p}^{\text{lab}}_{X}$[e]. Boosting from the GJ frame into the rest frame of ξ defines the second coordinate system called helicity frame (HF). The original direction of ξ defines z_{HF} and $\hat{y}_{\text{HF}} \propto \hat{z}_{\text{GJ}} \times \hat{z}_{\text{HF}}$. Since the GJ and HF frames are rest frames, in both coordinate systems the respective decay products are back-to-back. Therefore, a polar angle ϕ and an azimuthal angle ϑ specify each decay and, in total, four angles describe the phase-space of the three-body decay: (ϕ_{GJ}, ϑ_{GJ}) w.r.t. ξ for the X decay in the GJ frame and (ϕ_{HF}, ϑ_{GJ}) w.r.t. π^- for the decays $\xi \to \pi^-\omega$ and $\xi \to \pi^-\pi^0$ and π^0 for $\xi \to \pi^0\omega$ in the HF frame. Fig. 4.5 illustrates the definition of the Gottfried-Jackson and the helicity frames.

Figs. 4.6 to 4.8 show the correlation between $m_{\pi^-\pi^0\omega}$ and the Gottfried-Jackson angles for $\pi^-\omega$, $\pi^0\omega$, and $\pi^-\pi^0$ isobars, respectively. As expected from isospin symmetry, the $\pi^0\omega$ and $\pi^-\omega$ isobars show similar properties for both angles. Decay amplitudes depend on $e^{iM\phi_{\text{GJ}}}$, where the spin-projection quantum number M is the projection of J onto the z-axis in the GJ frame. We observe two humps in ϕ_{GJ} in most $m_{\pi^-\pi^0\omega}$ regions indicating contributions by amplitudes with $|M| = 1$. This is also true for events with $m_{\pi^-\pi^0\omega} < 1.35$, where we observe the $a_2(1320)$ signal in Fig. 3.33. We expect the value of J to be equivalent to the number of bumps in $\cos\vartheta_{\text{GJ}}$. The measured distributions show complex structures and no single amplitudes are dominant. Large asymmetries between positive and negative values of $\cos\vartheta_{\text{GJ}}$, which correspond to ξ flying along and against the X direction, respectively, are visible over the entire $m_{\pi^-\pi^0\omega}$ range. This indicates interferences between amplitudes with odd and even total angular momentum J. The same is also true in the $a_2(1320)$ mass region for the $\pi^0\omega$ and $\pi^-\omega$ isobars. While $a_2(1320)$ is below the $\omega\rho$ mass threshold,

[e] $\hat{v}$ denotes the unit vector of v.

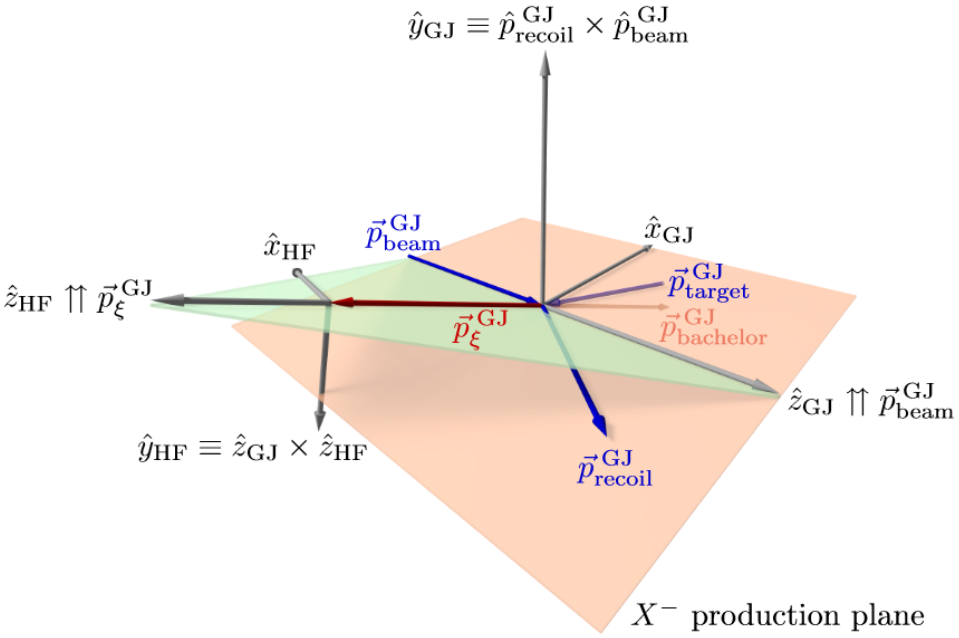

Figure 4.5: Geometry of the Gottfried-Jackson (GJ) and the helicity (HF) frame for the reaction beam + target $\to X$ + recoil and $X \to \xi$ + bachelor [39].

$a_2(1320)$ decays into $\omega\rho$ due to low mass tails of $\rho(770)$ and $\omega(782)$. Therefore, we expect two bumps in the $\cos\vartheta_{\mathrm{GJ}}$ for the $\pi^-\pi^+$ isobar for the $a_2(1320)$ mass region. However, Fig. 4.8d shows a flat distribution. Understanding if this is a result of interferences with other amplitudes requires a partial-wave analysis. For masses above $2.5\,\mathrm{GeV}/c^2$ the $\cos\vartheta_{\mathrm{GJ}}$ spectrum peaks around ±1 indicating dominant contributions from amplitudes with large J [14], which typically contain only small resonances. For the $\pi^-\pi^-\pi^+$ (Fig. A.5.b in Ref. [40]) and the $\eta^{(\prime)}\pi^-$ (Figs. 4.10d and 4.12d in Ref. [28]) channels this feature appears at lower masses around $2.0\,\mathrm{GeV}/c^2$. Therefore, $\pi^-\pi^0\omega$ provides a channel to study the contributions of lower J amplitudes which contain resonances at higher masses in more detail. Overall, studying distributions of different phase-space angles independently is not able to decompose the rich interference patterns. Disentangling the contributing amplitudes requires a partial-wave analysis, which takes into account the correlations between all phase-space variables.

4.3 Dalitz Plot of the $\omega(782)$ Decay

Besides studying highly excited resonances, the COMPASS data on the $\pi^-\pi^0\omega$ channel also allows us to study the three-body kinematics within the $\omega(782)$ decay [41, 42]. As was shown in Section 3.6, the background contributions below the $\omega(782)$ mass peak are still significant in the selected data. Since the background component behaves approximately linearly close to the $\omega(782)$ peak, we apply a linear background subtraction using sidebands in $m_{\pi^-\pi^0\pi^+}$.

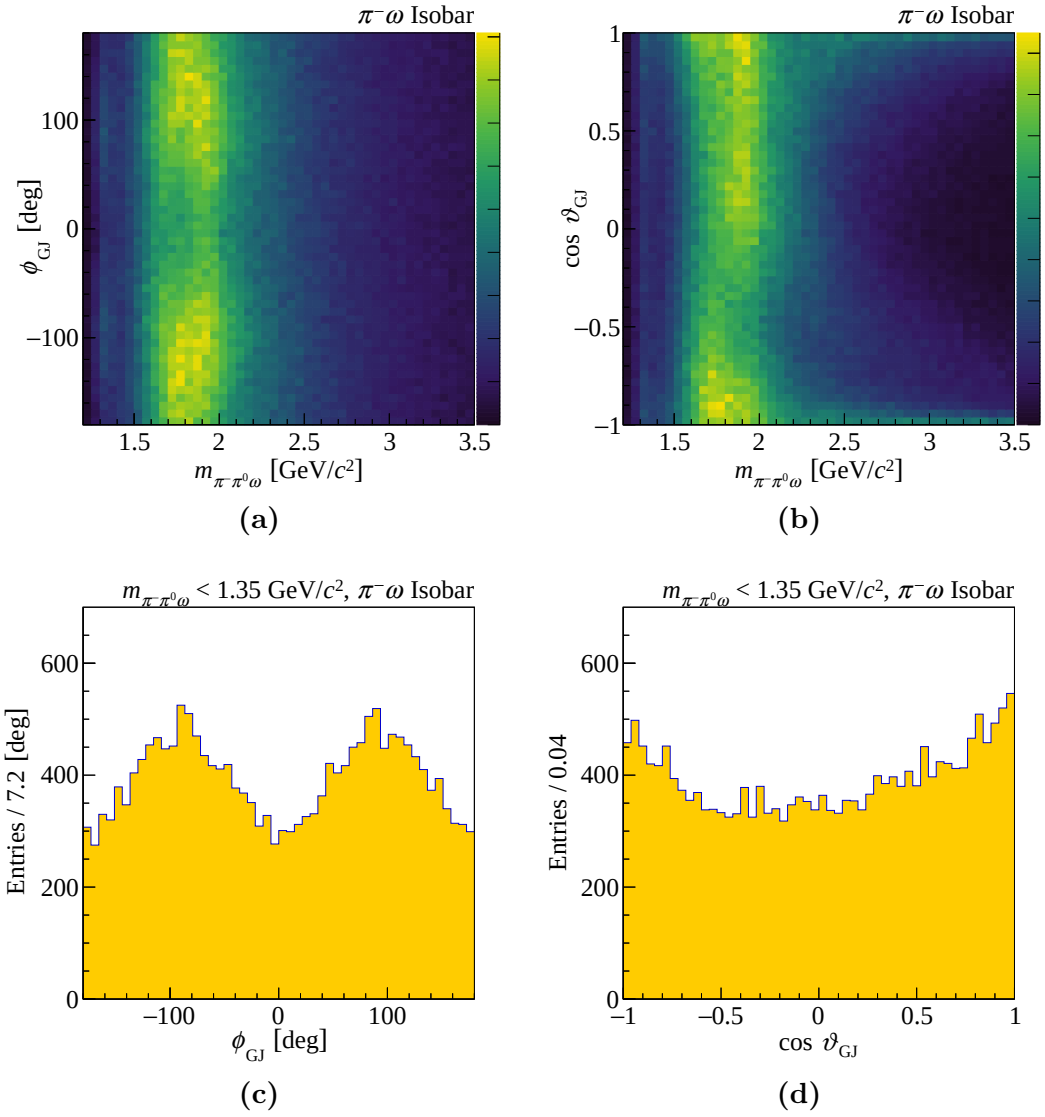

Figure 4.6: (a) and (b) show the distribution of ϕ_{GJ} and $\cos\vartheta_{\mathrm{GJ}}$ vs. $m_{\pi^-\pi^+\omega}$, respectively, for the $\pi^-\omega$ isobar. (c) shows the ϕ_{GJ} and (d) the $\cos\vartheta_{\mathrm{GJ}}$ distribution for events in the $a_2(1320)$ region with $m_{\pi^-\pi^+\omega} < 1.35\,\mathrm{GeV}/c^2$.

Fig. 4.9 shows the $m_{\pi^-\pi^0\pi^+}$ distributions before the $\omega(782)$ cut. In addition to the peak band, which is identical to the cut region in Table 3.11, we define a left and a right sideband for each year. The left sideband is centered $100\,\mathrm{MeV}/c^2$ below and the right sideband is centered $100\,\mathrm{MeV}/c^2$ above the peak position at m_ω. Both sidebands are half as wide as the peak band. In contrast to Section 3.6, events with multiple $\omega(782)$ candidates are not discarded. Instead, each $\pi^-\pi^0\pi^+$ combination within any band is considered. To remove the background contributions from kinematic distributions, we assume a linear $m_{\pi^-\pi^0\pi^+}$ dependence of the kinematic background on the kinematic distribution and subtract the distributions of the $\pi^-\pi^0\pi^+$ combinations within the left and

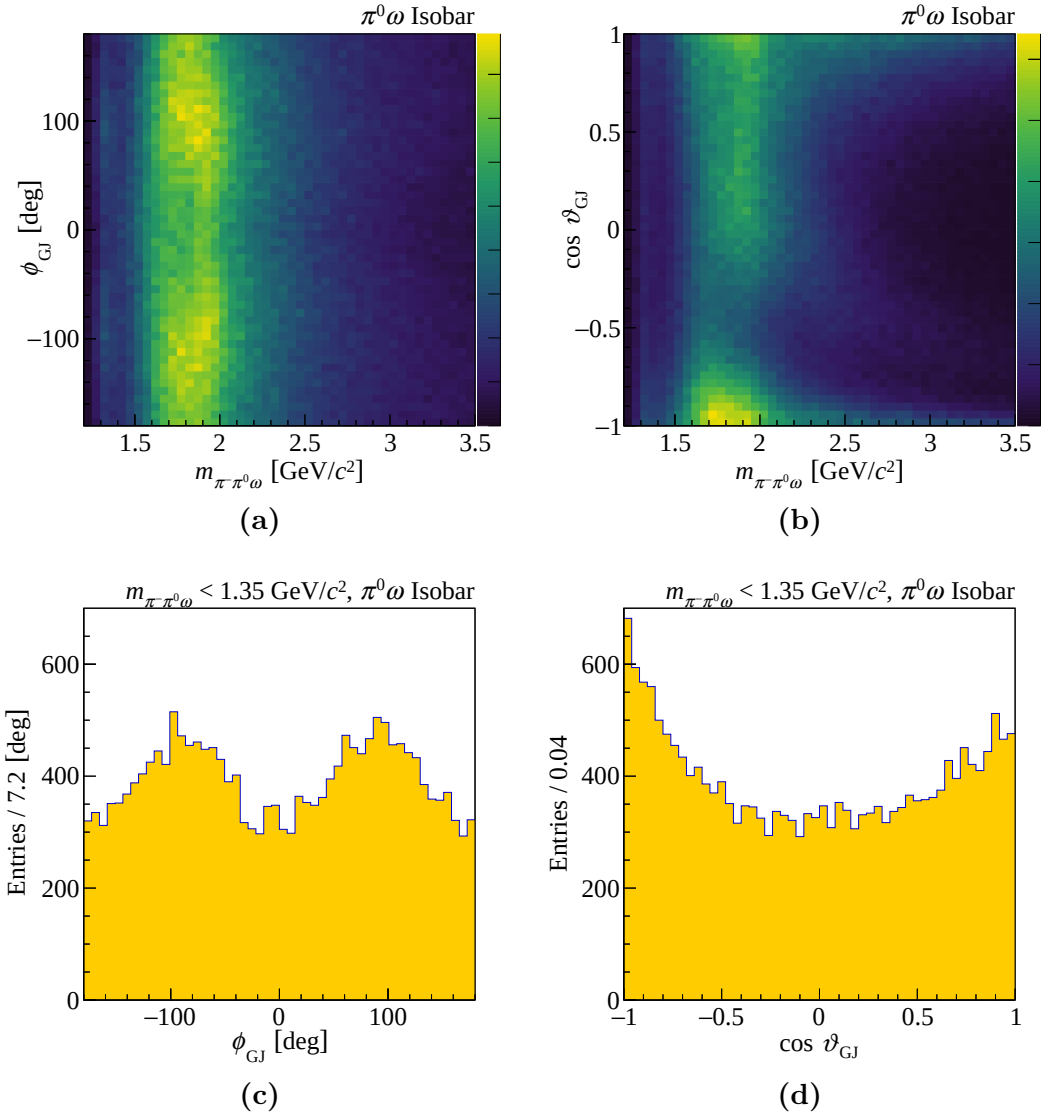

Figure 4.7: Same as Fig. 4.6 but for the $\pi^0\omega$ isobar.

right sidebands from the corresponding distribution of the $\pi^-\pi^0\pi^+$ combinations within the peak band.

To visualize the $\omega(782)$ Dalitz plot, we use the dimensionless variables x and y from Ref. [43], which are defined as

$$x = \frac{t-u}{\sqrt{3}R_\omega}, \quad y = \frac{s_0 - s}{R_\omega} + \frac{2(m_{\pi^\pm} - m_{\pi^0})}{m_\omega - 2m_{\pi^\pm} - m_{\pi^0}}, \tag{4.1}$$

where $R_\omega = 2/3 m_\omega (m_\omega - 2m_{\pi^\pm} - m_{\pi^0})$. The Mandelstam variables s, t, and u are the squared invariant masses of the $\pi^-\pi^+$, $\pi^-\pi^0$, and $\pi^0\pi^+$ subsystems, respectively, within the $\pi^-\pi^0\pi^+$ subsystem selected as $\omega(782)$ and $s_0 = (s + t + u)/3$. Since the three pions are isospin symmetric and the definition of y corrects for the mass difference between $\pi^\pm$ and π^0, we expect the Dalitz plot of the $\omega(782)$ decay in the variables in Eq. (4.1) to be symmetric under 120°

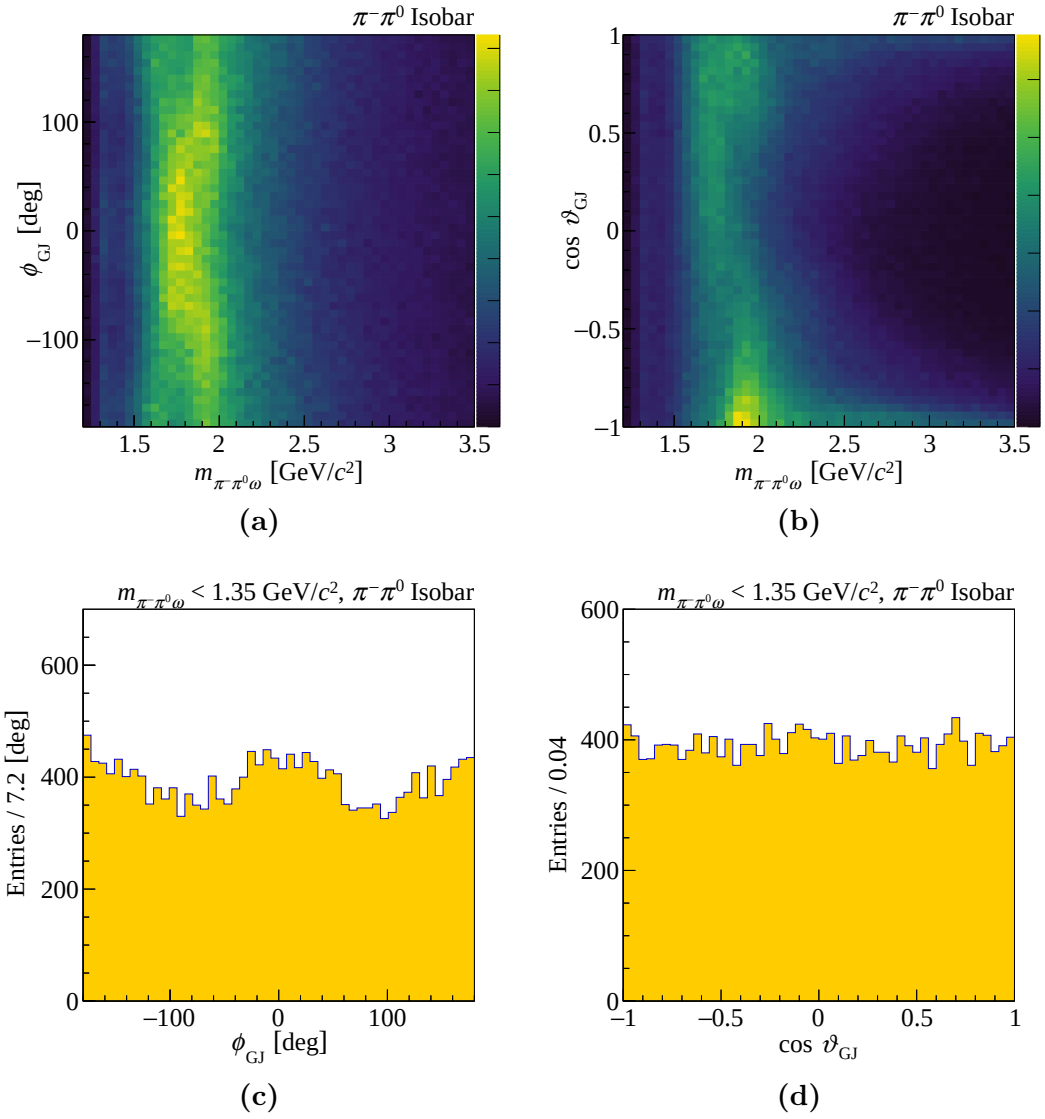

Figure 4.8: Same as Fig. 4.6 but for the $\pi^-\pi^0$ isobar.

rotations about the origin. Fig. 4.10 shows the Dalitz plots for both sidebands, the peak band, and the background subtracted sample. The Dalitz plots for the peak band and the subtracted sample are approximately symmetric, which agrees with the expectation of a dominant $\omega(782)$ contribution. For the left and especially the right sideband, the Dalitz plot shows an asymmetric behavior as they contain background and no $\omega(782)$ decay. Using the background-subtracted Dalitz plot a Dalitz plot analysis of the $\omega(782) \to \pi^-\pi^0\pi^+$ decay is possible. The structure of the Dalitz plot consists of the product of a dominant P-wave phase-space contribution and dynamical effects on a 25% scale [42]. We expect both factors to be symmetric. Fig. 4.11a shows the pure P-wave Dalitz plot simulated based on Ref. [43], which is symmetric. By dividing the measured by the P-wave Dalitz plot we obtain the Dalitz plot of the dynamics containing also the spectrometer acceptance shown in Fig. 4.11b. Bins at

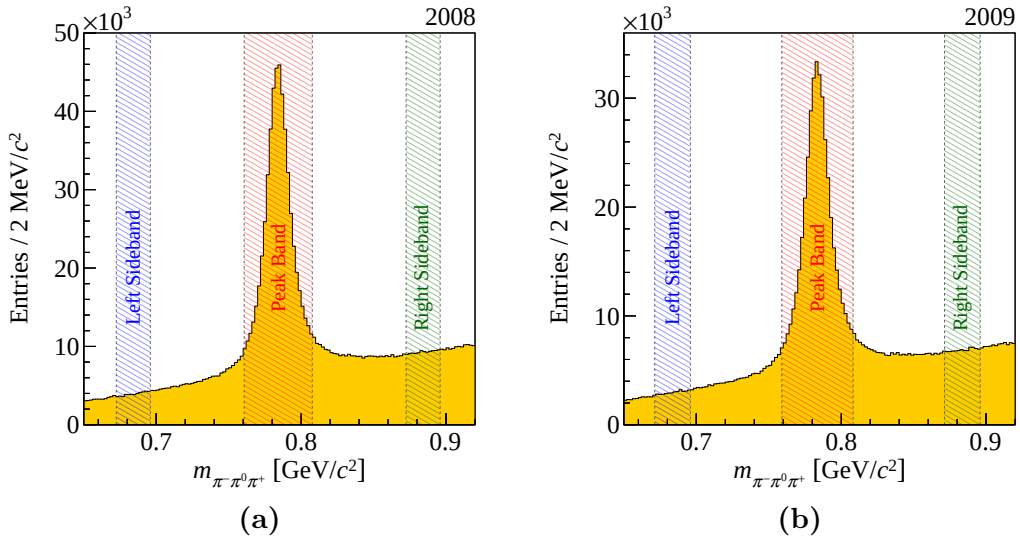

Figure 4.9: $m_{\pi^-\pi^0\pi^+}$ distributions for (a) 2008 and (b) 2009 data. The region hatched in red indicates the peak region. The regions hatched in blue and green are the left and right sidebands, respectively.

the edges contain only few events and are therefore not shown. While the bins in the center show a flat distributions, the bins close to the edges are non-symmetric and disagree with the theoretical prediction for the dynamics from Ref. [42] shown in Fig. 4.11c. We assume the deviations are a result of the acceptance, which is particularly low for $\omega(782)$ decays containing a low-energy π^0. Therefore, performing a precise Dalitz plot analysis for COMPASS data requires simulation of the acceptance to obtain a Dalitz plot containing only dynamics. Up to now the most precise Dalitz plot analysis was done by BESIII in Ref. [43]. While the background component for the $\pi^-\pi^0\omega$ channel in COMPASS data is significantly larger than for the $J/\psi \to \omega\eta$ channel in BESIII data, the COMPASS data set contains about 735 000 events and is therefore about 2.8 larger than the BESIII data set. COMPASS data could contribute in improving the precision of the Dalitz plot analysis of the $\omega(782)$ decay and verify theoretical predictions, e.g. Ref. [42].

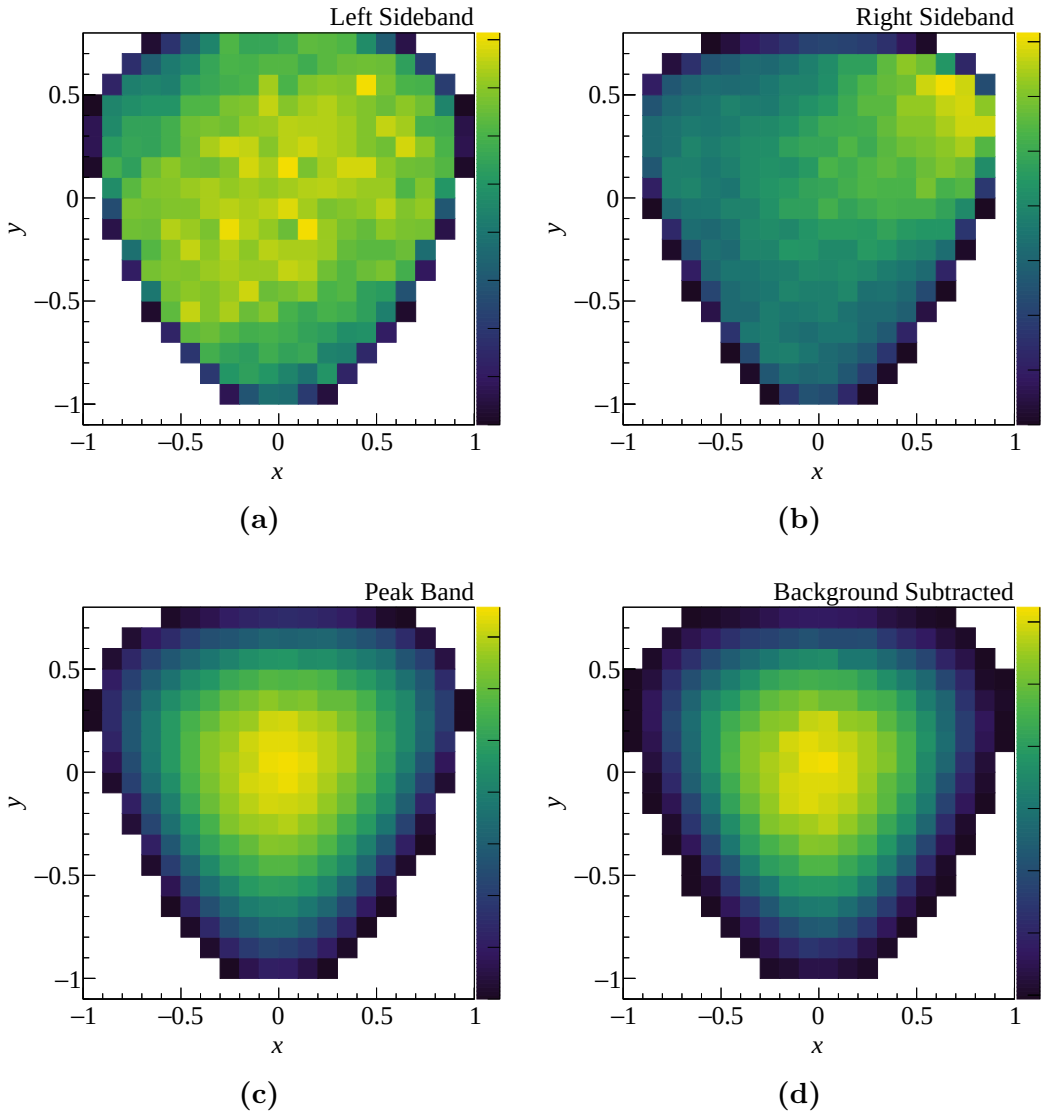

Figure 4.10: Dalitz plots of the $\pi^-\pi^0\pi^+$ subsystem selected as $\omega(782)$ using the variables x and y (see Eq. (4.1)). The Dalitz plots contain $\pi^-\pi^0\pi^+$ combinations within (a) the left sideband, (b) the right sideband, and (c) the peak band. (d) shows the sideband-subtracted Dalitz plot.

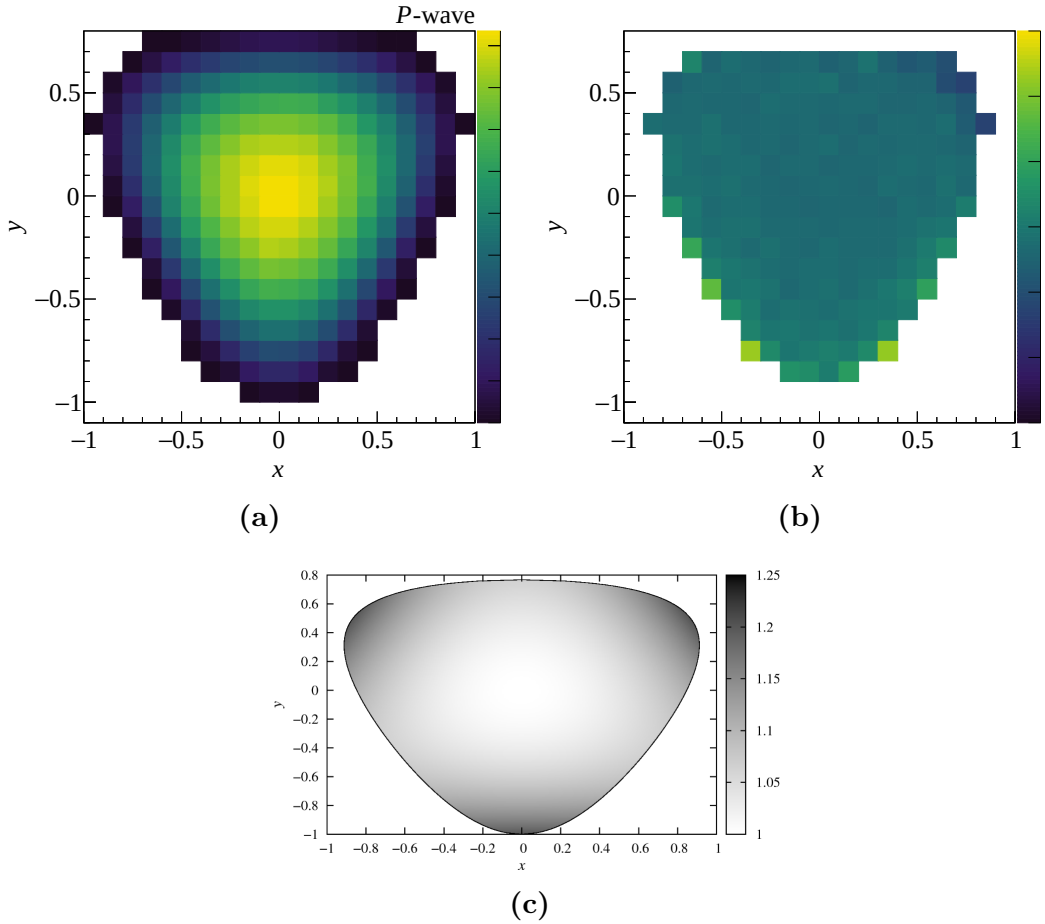

Figure 4.11: Dalitz plot of the $\omega(782)$ for (a) the simulated P-wave decay, (b) the measured dynamics including acceptance effects, and (c) the predicted dynamics (see Fig. 5 in Ref. [42]). The color scale in (b) ranges from 0 to 2.

Chapter 5

Monte Carlo Simulation

Estimating the acceptance and resolutions of the spectrometer requires Monte Carlo simulation. In principle, this needs a realistic model for the reaction, in particular for $X \to \pi\pi\omega \to 5\pi$. Since this model can only be obtained by a partial-wave analysis and phase-space acceptance is a required input for the partial-wave analysis, we here use phase-space distributed 5π events without simulating the $\omega(782)$ resonance. Therefore, the absolute acceptance for $\pi^-\pi^0\omega$ is not accessible but the simulation gives an estimate for the phase-space acceptance of the spectrometer for the 5π final state. This allows us to study uniformity of acceptance in kinematic variables required for a partial-wave analysis. After phase-space generation, each simulated 5π event goes through a detector simulation based on GEANT3. We perform an event reconstruction and selection similar to real data. Since detector simulation is expensive, we increase computational efficiency by requiring at least one $\pi^-\pi^0\pi^+$ combination to have an invariant mass within the range $780 \pm 75\,\mathrm{MeV}/c^2$ during the generation process. Events are generated uniformly in the $m_{5\pi}$ range from $1.2\,\mathrm{GeV}/c^2$ to $3.5\,\mathrm{GeV}/c^2$ and with a double exponential t' distribution given in Eq. (3.26) in the t' range from $0.1\,(\mathrm{GeV}/c)^2$ to $1.0\,(\mathrm{GeV}/c)^2$. The t' distribution is correlated with the $m_{5\pi}$ distribution. This is taken into account by fitting Eq. (3.26) in $400\,\mathrm{MeV}/c^2$ wide $m_{5\pi}$ bins and then interpolating the t' parameters depending on $m_{5\pi}$. Table 5.1 lists the points used for interpolation. Since the lowest and the two highest $m_{5\pi}$ bins contain less events compared to the other bins, a single exponential is sufficient. The decays of π^0 to photon pairs, the propagation of the $\pi^\pm$ and photons through the spectrometer and the interaction with the detectors is simulated to obtain pseudodata, which are similar to real data. The event selection for the 2008 data presented in Chapter 3 is used to analyse the simulated data. Of the 10^8 generated events about 987 000 events pass the event selection.

Table 5.1: List of t' parameters used in Eq. (3.26) for $400\,\mathrm{MeV}/c^2$ wide bins of $m_{5\pi}$ around the listed center values.

$m_{5\pi}$ Bin Center $[\mathrm{GeV}/c^2]$	b_1 $[(\mathrm{GeV}/c)^{-2}]$	r	b_2 $[(\mathrm{GeV}/c)^{-2}]$
1.2	4.567	–	–
1.6	7.143	0.150	3.539
2.0	7.193	0.189	3.604
2.4	6.199	0.076	2.638
2.8	5.609	0.030	1.907
3.2	5.251	–	–
3.6	4.850	–	–

5.1 Resolutions

We estimate the π^0 resolution of the spectrometer by performing a fit of the $m_{\gamma\gamma}$ distribution similar to Section 3.5 but using a single Gaussian distribution to describe the π^0 peak. Fig. 5.1 shows the fit of Eq. (3.22) to the $m_{\gamma\gamma}$ distribution for all photon-pair cases. Table 5.2 lists the obtained relevant fit parameters. Large values of χ^2_{red} indicate a poor quality of the fit. Comparing the fit curve and the data in Fig. 5.1 reveals large discrepancies between the Gaussian distribution used as signal and the shape of the peak in MC data. The peak is asymmetric with enhancements in the lower-mass shoulder. Since using a double-Gaussian distribution instead of a Gaussian as signal would not be able to describe this asymmetry as well, it does not significantly improve the fit and therefore we use only the single Gaussian. The peak position in the distribution containing all photon pairs and in the distribution for the ECAL2 photon-pair case agree with the nominal π^0 mass within $1\,\mathrm{MeV}/c^2$, but the distributions for the ECAL1 and the mixed ECAL photon-pair cases peak at lower masses differing from the nominal π^0 mass by about $2\,\mathrm{MeV}/c^2$. For all photon-pair cases, the peak widths, which are due to the detector resolution, are smaller in the simulated data than in the real data (see Fig. 3.11 and Table 3.5). This could be partly due to the use of a Gaussian signal instead of a double-Gaussian signal, which picks up less contributions from the non-Gaussian tails. The main reason, however, is the disagreement between simulation and real data originating from underestimation of the ECAL resolutions in the detector simulation. The π^0 candidates in simulated data are selected using the parameters listed in Table 5.2 (see Section 3.5).

Besides the π^0 resolution, we estimate the resolution $\delta\chi$ of a measured physical quantity χ by studying the distribution of the corresponding residuum $\Delta\chi$, i.e. the difference of the reconstructed and the true value of the quantity in the simulation. To obtain $\delta\chi$ as a function of χ, we fit Gaussians to the $\Delta\chi$ distribution in slices of χ and estimate the resolution as the width of the

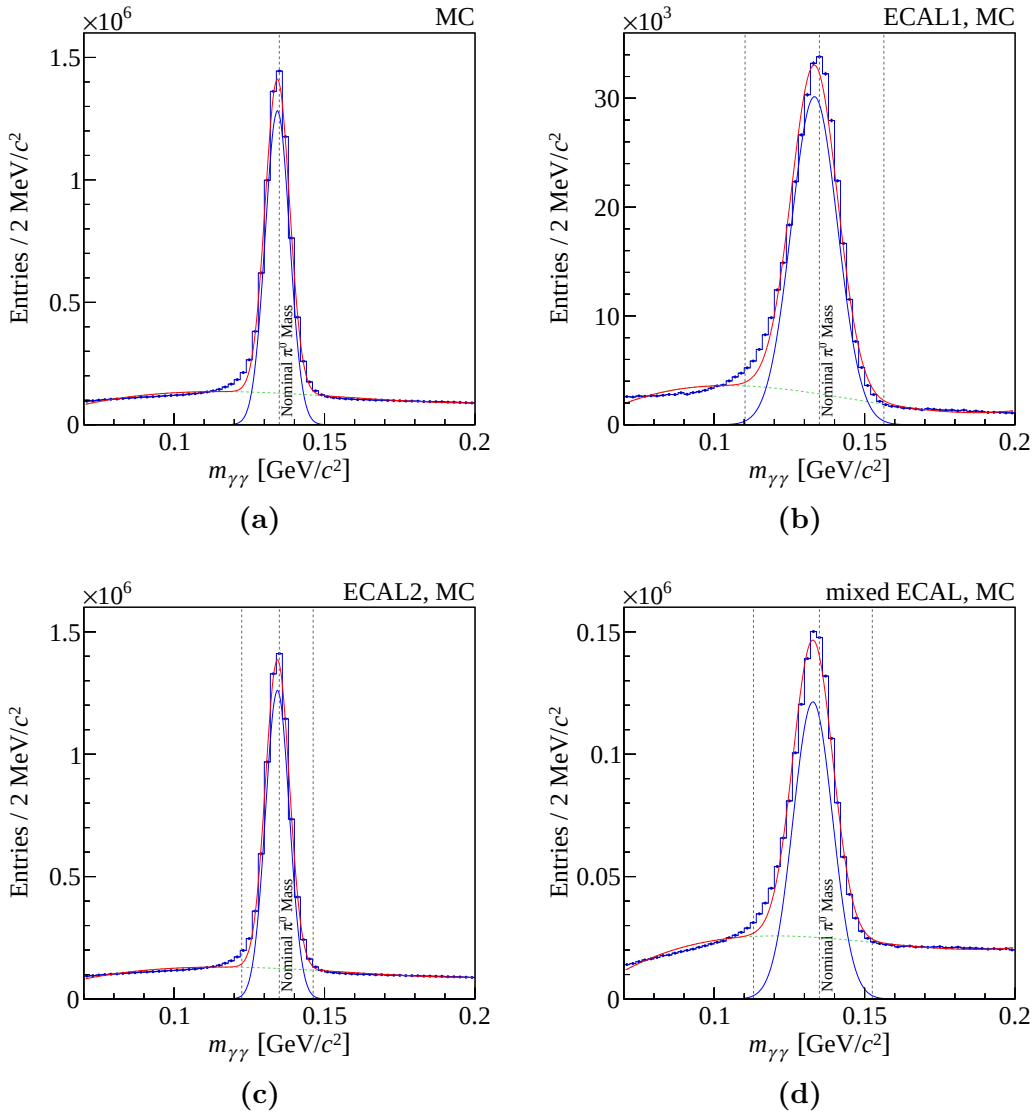

Figure 5.1: Distributions of $m_{\gamma\gamma}$ for (a) all photon pairs, (b) ECAL1 photon pairs, (c) ECAL2 photon pairs, and (d) mixed ECAL photon pairs for simulated data. The applied cuts are discussed in Section 3.5. The red curve represents the result of fitting Eq. (3.22) to the $m_{\gamma\gamma}$ distribution. The blue solid curve shows the Gaussian representing the π^0 signal component. The green dashed curve represents the background component. The central vertical line indicates the nominal π^0 mass, while the outer two vertical lines indicate the selected $m_{\gamma\gamma}$ window.

Table 5.2: Fit parameters obtained by fitting the π^0 peak in the $m_{\gamma\gamma}$ distribution of simulated data for the various photon-pair cases.

Parameters		all	ECAL1	ECAL2	mixed ECAL
$m_{\pi^0,\text{mean}}$	[MeV/c^2]	134.35	133.33	134.36	132.81
σ_mass	[MeV/c^2]	4.04	7.69	3.96	6.58
χ^2_red (NDF)		1100 (58)	79 (58)	880 (58)	160 (58)

Gaussian. Fig. 5.2 shows the resolutions for $m_{\pi^-\pi^0\omega}$, $m_{\pi^-\pi^0}$, $m_{\pi^-\omega}$, $m_{\pi^0\omega}$, and t' as functions of the corresponding quantity. For all quantities the resolution is an almost linear function of the quantity itself. Fig. 5.3 shows the $\Delta m_{\pi^-\pi^0\pi^+}$ distribution around the $\omega(782)$ mass. The peak represents the resolution function. The flat contribution below the peak is combinatorical background from reconstruction. In Fig. 5.3a, the distribution is fitted by the sum of a Gaussian $\mathcal{N}$ and a constant, i.e.

$$\frac{d(\Delta m_{\pi^-\pi^0\pi^+})}{dN} = A_\text{Res}\,\mathcal{N}(\Delta m_{\pi^-\pi^0\pi^+}; \mu_\text{Res}, \sigma_\text{Res}) + C_\text{Res}, \tag{5.1}$$

and in Fig. 5.3b it is fitted by the sum of a double-Gaussian (see Appendix B.1) and a constant, i.e.

$$\frac{d(\Delta m_{\pi^-\pi^0\pi^+})}{dN} = A_\text{Res} D_\text{G}(\Delta m_{\pi^-\pi^0\pi^+}; R_\text{Res}, \mu_\text{Res}, \sigma_{1,\text{Res}}, \sigma_{2,\text{Res}}) + C_\text{Res} \tag{5.2}$$

with D_G from Eq. (B.1). The fit range is from $\Delta m_{\pi^-\pi^0\pi^+} = -30\,\text{MeV}/c^2$ to $\Delta m_{\pi^-\pi^0\pi^+} = 30\,\text{MeV}/c^2$. Table 5.3 lists the relevant peak parameters obtained by these fits. For the Gaussian fit, we obtain a large χ^2_red value because Eq. (5.1) does not describe well the peak region and the wings of the $\Delta m_{\pi^-\pi^0\pi^+}$ distribution. Eq. (5.2) describes the distribution better yielding a smaller χ^2_red values. However, also the double-Gaussian distribution shows slight systematic differences suggesting that the real resolution function is even more complicated. This is also observed in real-data (see Section 3.6). There, due to the systematic differences, the obtained decay width Γ_0 is significantly larger than the nominal value and σ is about a factor of 1.3 smaller compared to simulation.

5.2 Acceptance

We estimate the acceptance by calculating the ratio of selected to generated events for simulated events. Resolution effects are not considered, but for selected as well as generated events the true values of physical quantities are used. Since the $\omega(782)$ decay is not simulated, the obtained acceptance is no measure for the absolute acceptance of the detector for $\pi^-\pi^0\omega$ but for the relative acceptance η_PS for the 5π final state generated in phase space.

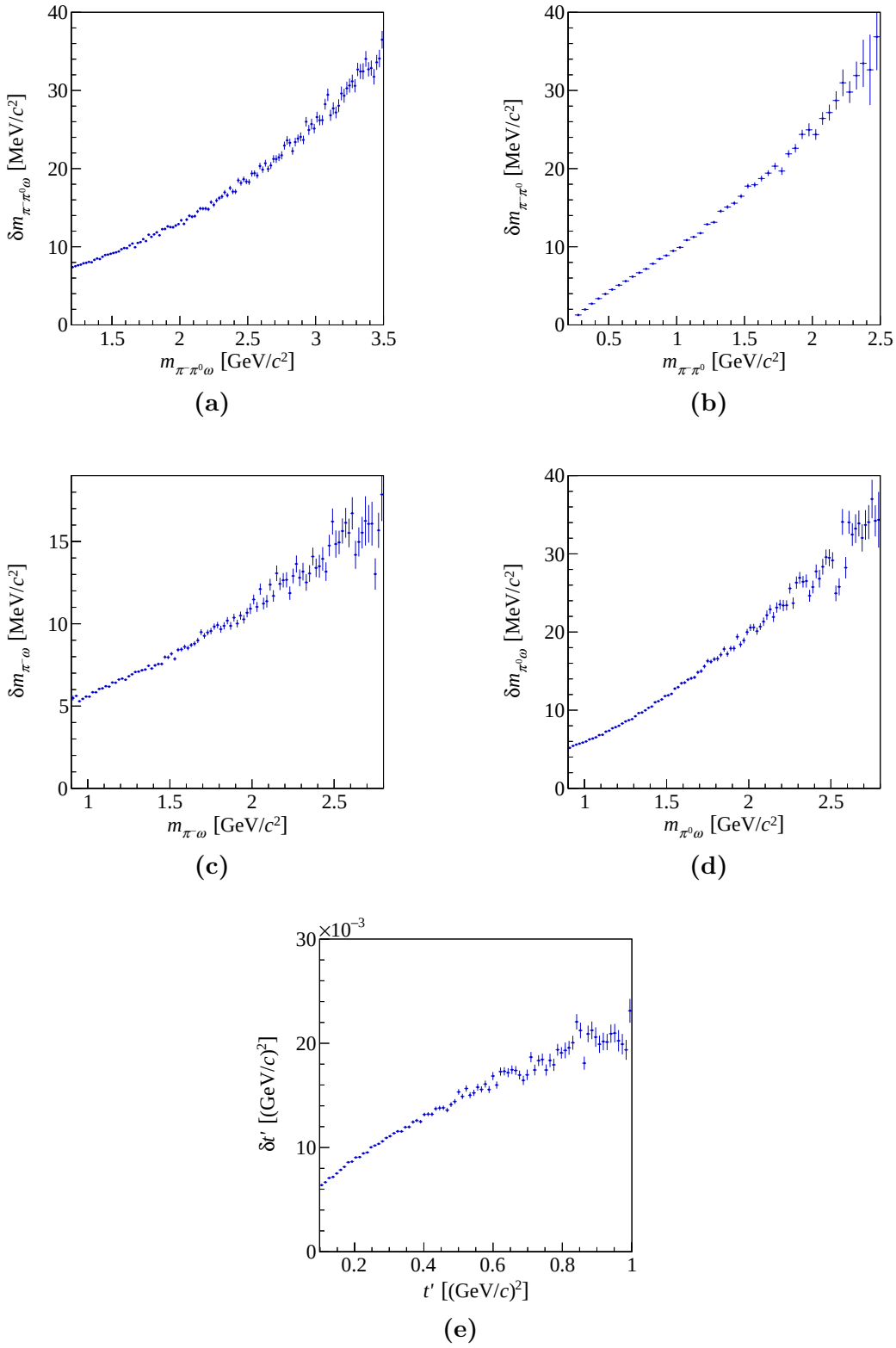

Figure 5.2: Resolutions for (a) $m_{\pi^-\pi^0\omega}$, (b) $m_{\pi^-\pi^0}$, (c) $m_{\pi^-\omega}$, (d) $m_{\pi^0\omega}$, and (e) t' as a function of the corresponding kinematic variable.

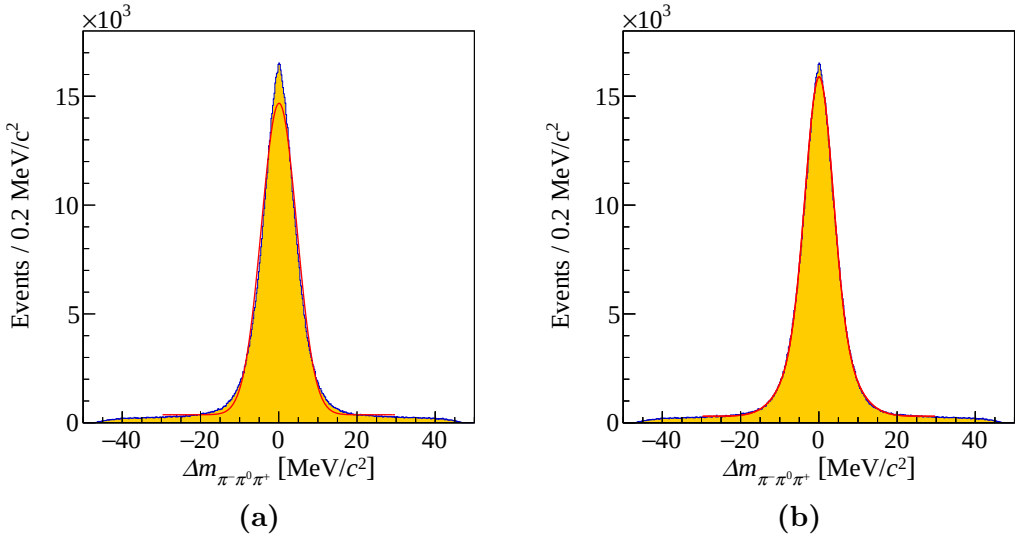

Figure 5.3: Distribution of $\Delta m_{\pi^-\pi^0\pi^+}$ around the $\omega(782)$ mass. The red curve shows a fit to the MC data, which in (a) is Eq. (5.1) and in (b) is Eq. (5.2).

Table 5.3: Parameters obtained by fitting Eqs. (5.1) and (5.2) to the Δm_ω distribution in Fig. 5.3.

Parameters		Eq. (5.1)	Eq. (5.2)
R_{Res}		—	0.41
μ_{Res}	$[\text{MeV}/c^2]$	0.09	0.09
$\sigma_{1,\text{Res}}$	$[\text{MeV}/c^2]$	—	6.72
$\sigma_{2,\text{Res}}$	$[\text{MeV}/c^2]$	—	3.44
σ_{Res}	$[\text{MeV}/c^2]$	4.52	4.79
χ^2_{red} (NDF)		40 (295)	3.0 (294)

5.2.1 Phase-Space Acceptance

Figs. 5.4 to 5.6 show the angular distribution of the phase-space acceptance η_{PS} in the GJ and HF frames (see Section 4.2) for the $\pi^0\omega$, $\pi^-\omega$, and $\pi^-\pi^0$ subsystem, respectively, for different $m_{\pi^-\pi^0\omega}$ ranges. In some kinematic regions, we observe a strong $m_{\pi^-\pi^0\omega}$ dependence of η_{PS}. From the analysis of the $\pi^-\pi^-\pi^+$ channel [40] we know that the acceptance for charged particles is rather uniform in the phase-space variables (see Figs. 7.3 and 7.4 in Ref. [40]). Hence the non-uniformity of the angular acceptances is mainly caused by the photon-detection and π^0 reconstruction efficiency. This can be seen, for example, by comparing the acceptances for the $\pi^0\omega$ and $\pi^-\omega$ isobars, which exhibit distinct distributions. For the $\pi^-\omega$ isobar, two low-acceptance bands around $\cos\vartheta_{\text{GJ}} = \pm 0.5$ and a drop at $\cos\vartheta_{\text{GJ}} = +1$ and $\phi_{\text{GJ}} = 0$ are visible in Fig. 5.4. This is similar to the acceptance for the $\pi^-\pi^0$ isobar in the $\pi^-\pi^0\pi^0$

channel (see Fig. 3.15 in Ref. [26]), where photon absorption in the RICH pipe[f] and the overlap of the two electromagnetic calorimeters were suggested as causes. For the $\pi^0\omega$ isobar, two low-acceptance bands are visible close to $\phi_{\mathrm{HF}} = \pm 180°$ in Fig. 5.5, which is similar to the acceptance for the $\pi^-\pi^0$ isobar in the $\pi^-\pi^0\pi^0$ channel (see Fig. 3.16 in Ref. [26]). For the $\pi^-\pi^0$, two low-acceptance bands are visible at smaller ϕ_{HF} in Fig. 5.6. Due to the different definition of the angles with respect to the π^0 in the isobar helicity frames (see Section 4.2), photons absorbed in a certain region are a possible explanation for the bands observed for both isobars. Ref. [26] suggests the overlap of the ECALs is also reason for this effect. Overall, all low-acceptance effects occur only in two-body subsystems containing π^0, which agrees with the expectation of effects due to the photon-detection efficiencies. However, verifying the suggested effects of the RICH pipe and the overlap of the electromagnetic calorimeters as real causes requires further simulation studies investigating the traversed material of the photons.

[f] A 0.15 mm thick steel pipe at the nominal beam axis separates traversing beam particles from the refractive medium within the RICH-1 detector.

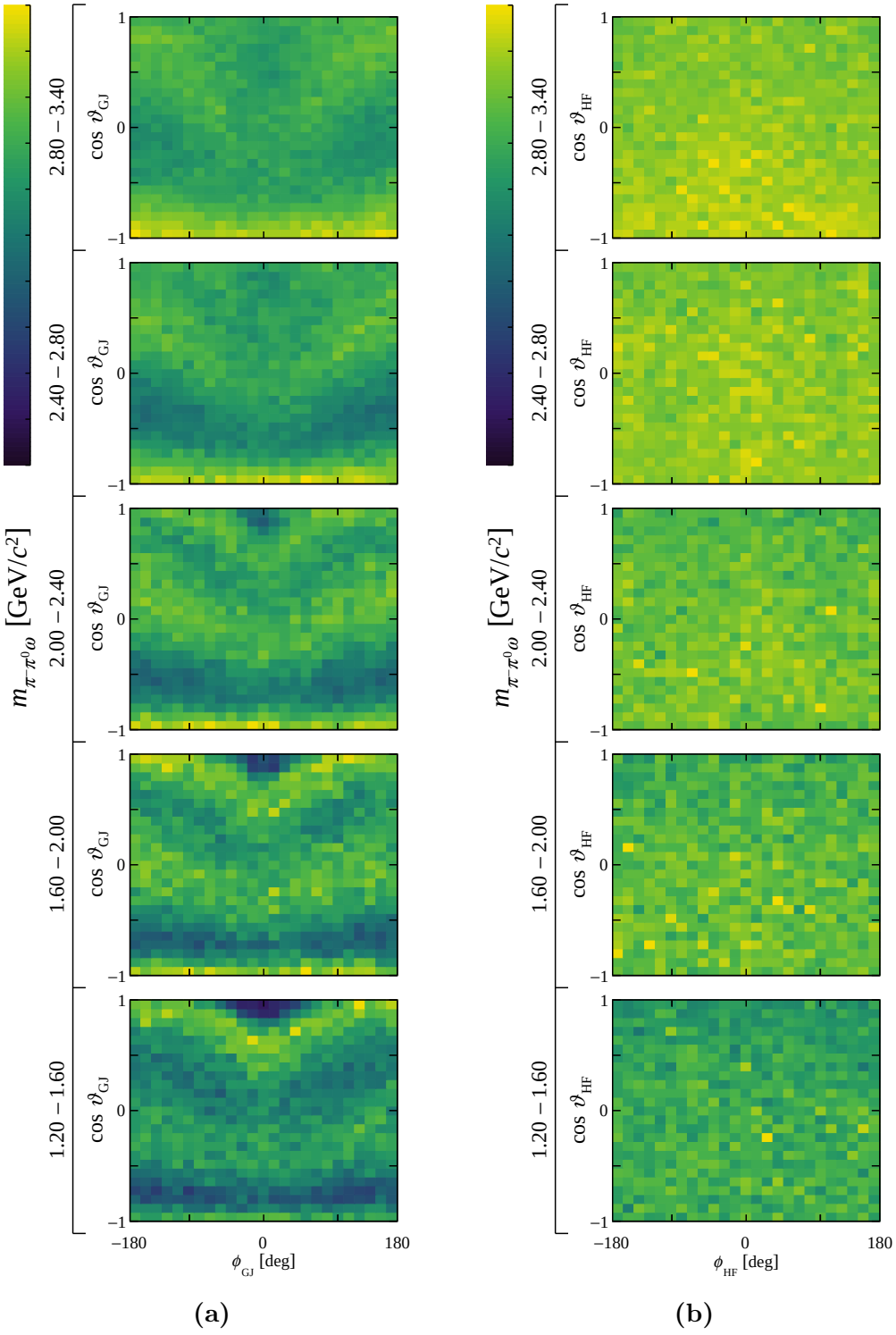

Figure 5.4: Acceptance η_{PS} in the five-pion phase space as a function of (a) the GJ and (b) the HF angles of the $\pi^-\omega$ isobar subsystem for bins in $m_{\pi^-\pi^0\omega}$. The color axis representing η_{PS} ranges from 0 to 1.

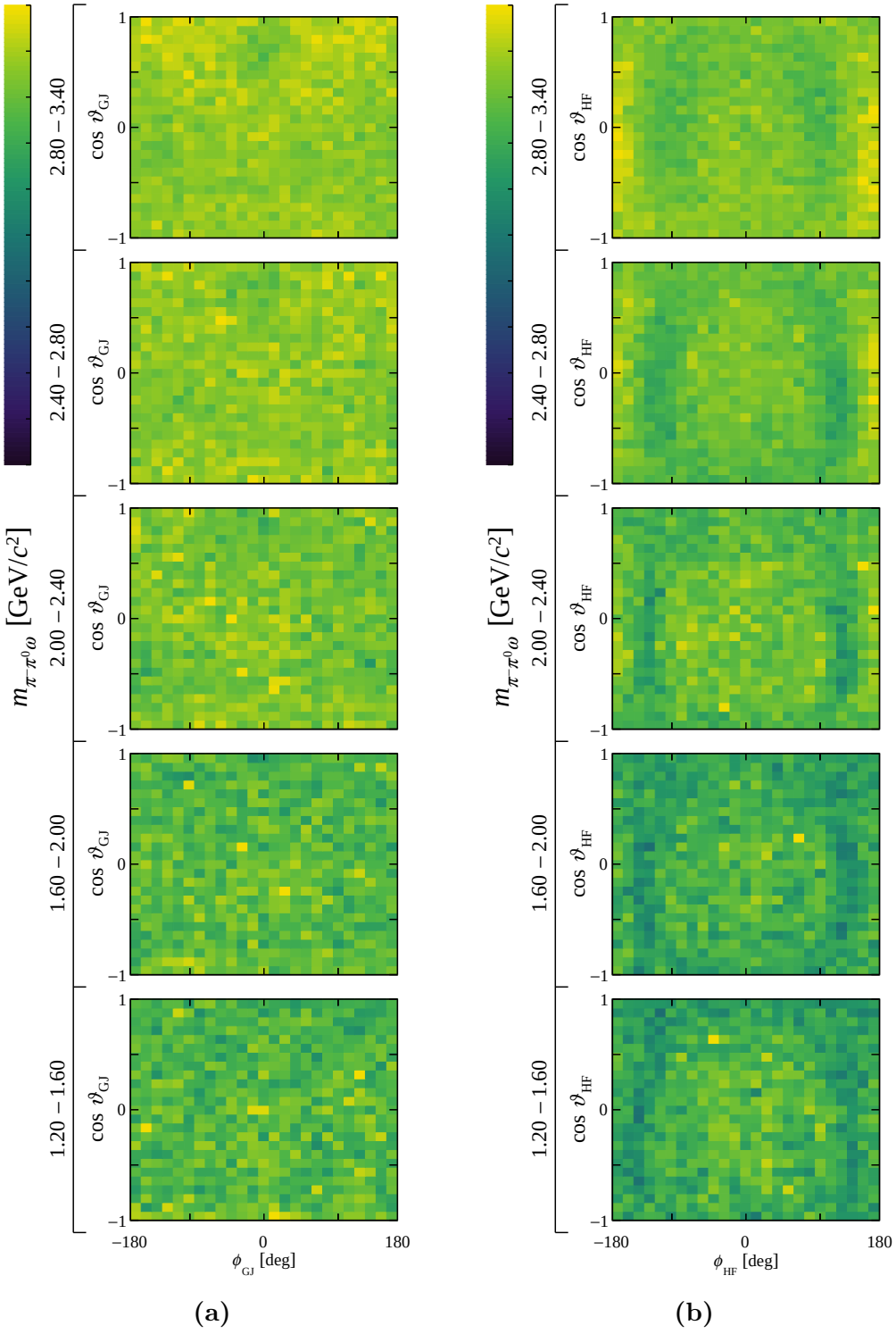

Figure 5.5: Same as Fig. 5.4 but for the $\pi^0\omega$ isobar subsystem.

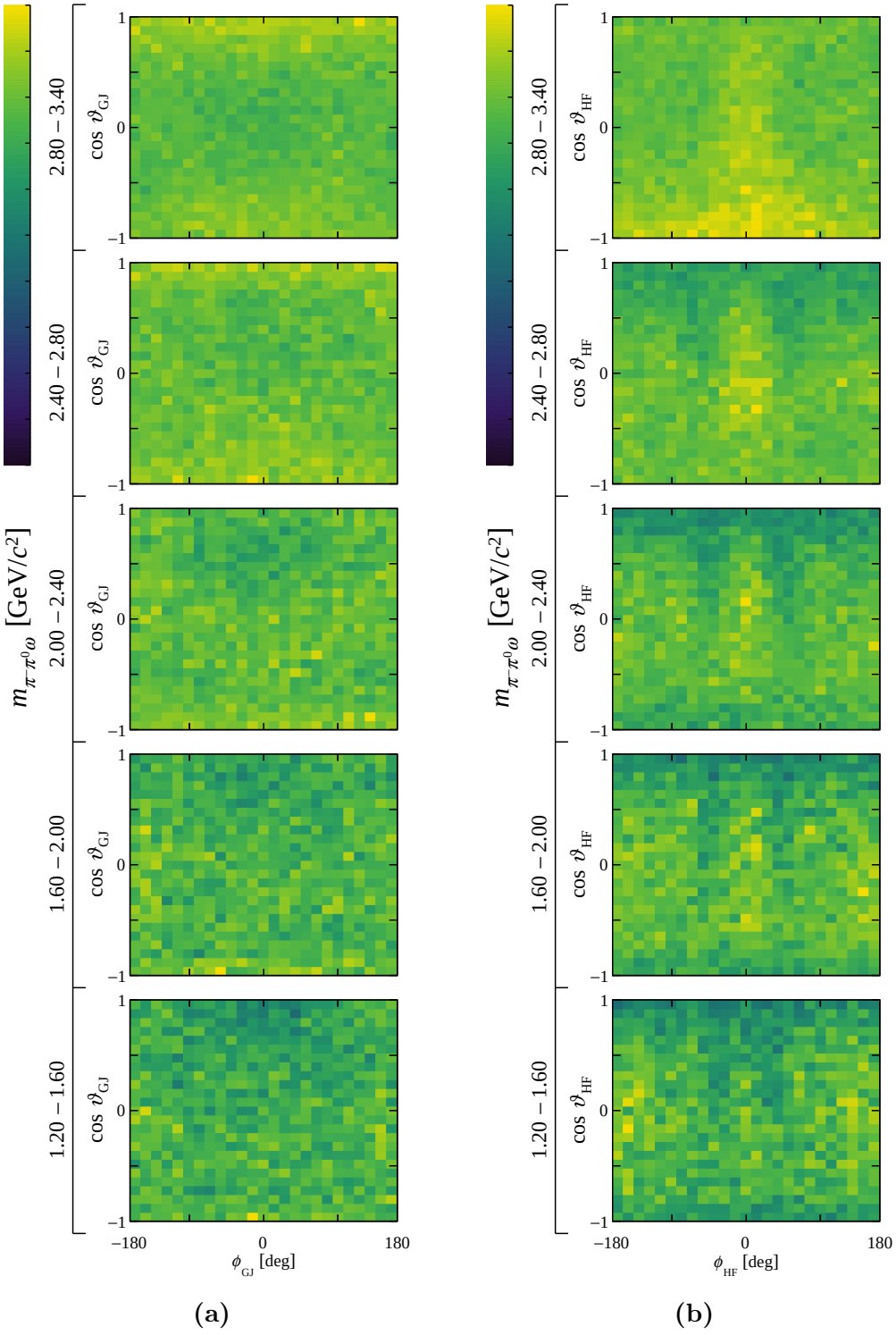

Figure 5.6: Same as Fig. 5.4 but for the $\pi^-\pi^0$ isobar subsystem.

Chapter 6

Conclusion and Outlook

In this thesis, we have performed an event selection for the diffractive scattering process $\pi^- + p \to \pi^-\pi^0\omega(782) + p$ in COMPASS. We reject kaon contaminations in the beam and charged final-state particles based on established methods. We reconstruct $\omega(782)$ from its decay into $\pi^-\pi^0\pi^+$. We reconstruct two π^0 from four photon candidates under consideration of the individual resolutions of the two electromagnetic calorimeters. The energy thresholds of both electromagnetic calorimeters are optimised using the statistical significance of the π^0 and $\omega(782)$ peaks as figure of merit. We perform an investigation on the stability of the observed π^0 and $\omega(782)$ peaks over time. Runs, for which the peak parameters indicate a poor quality of the measurement, are excluded. This accounts for about 2% of the events.

The obtained $\pi^-\pi^0\omega(782)$ sample in COMPASS contains about 730 000 events and is therefore about 5 times larger than the so far largest $\pi^-\pi^0\omega(782)$ sample taken by the BNL E852 experiment. The obtained sample shows dominant $b_1(1235)\pi$ and $\omega\rho(770)$ contributions, which is similar to previous analyses of the channel such as the analysis of E852. The angular distributions show strong interference effects. However, studying the contributing decay amplitudes requires a partial-wave analysis. The acceptance is studied based on simulated phase-space events and shows pronounced angular dependencies of the acceptance in some kinematic ranges. However, it is important that we find no region with zero acceptance. We suggest photon-detection efficiencies as reason for these effects. The selected $\pi^-\pi^0\omega(782)$ sample and the phase-space acceptance are the required inputs to perform a partial-wave analysis in the future. The large data sample is promising for verifying the $\pi_1(2015)$ signal claimed by E852 and for searches for additional states in the 1^{-+} sector. Furthermore, while previous searches in the $\pi\pi\pi$ and $\eta^{(\prime)}\pi$ COMPASS data were sensitive to resonances up to about $2.0\,\mathrm{GeV}/c^2$, a partial-wave analysis in the $\pi\pi\omega$ channel is potentially sensitive for resonances up to $2.5\,\mathrm{GeV}/c^2$. Another advantage is, that many ground sates, which otherwise would dominate the spectrum, are phase-space suppressed.

We further investigate the kinematic distribution of the $\pi^-\pi^0\pi^+$ system

from the selected $\omega(782)$. Performing a sideband subtraction reduces the background contributions. However, we observe considerable acceptance effects within the Dalitz plots, which need further studies. Based on the obtained data, a Dalitz-plot analysis of the $\omega(782)$ decay is possible, which can be compared to theory predictions.

Appendix A

Reconstruction of the Beam Energy

The beam energy is

$$E_{\text{beam}} = \sqrt{m_{\pi^-}^2 + |\vec{p}_{\text{beam}}|^2}. \tag{A.1}$$

There are two different ways to calculate t. The first uses the beam four-momentum $p_{\text{beam}} = (E_{\text{beam}}, \vec{p}_{\text{beam}})$ and the reconstructed p_X of the indermediate state X^-. The second calculation assumes a resting target proton, i.e. $p_{\text{target}} = (m_p, \vec{0})$, and a recoiling proton with four-momentum $p_{\text{recoil}} = (E_{\text{recoil}}, \vec{p}_{\text{recoil}})$. Energy conservation implies $E_{\text{recoil}} - m_p = E_{\text{beam}} - E_X$. We therefore obtain the following equations:

$$\begin{aligned} t &= (p_{\text{beam}} - p_X)^2 && \text{(A.2)} \\ &= m_{\pi^-}^2 + m_X^2 - 2p_{\text{beam}}p_X && \text{(A.3)} \\ &= m_{\pi^-}^2 + m_X^2 - 2E_{\text{beam}}E_X + 2|\vec{p}_{\text{beam}}||\vec{p}_X|\cos\theta && \text{(A.4)} \end{aligned}$$

and

$$\begin{aligned} t &= (p_{\text{recoil}} - p_{\text{target}})^2 && \text{(A.5)} \\ &= 2m_p^2 - 2m_p^2 E_{\text{recoil}} && \text{(A.6)} \\ &= 2m_p^2 - 2m_p(m_p + E_{\text{beam}} - E_X) && \text{(A.7)} \\ &= 2m_p(E_X - E_{\text{beam}}) && \text{(A.8)} \\ &= 2m_p\left(E_X - \sqrt{m_{\pi^-}^2 + |\vec{p}_{\text{beam}}|^2}\right). && \text{(A.9)} \end{aligned}$$

Setting Eqs. (A.4) and (A.9) equal and squaring the hole expression leads to a quadratic equation in $|\vec{p}_{\text{beam}}|$

$$0 = a\,|\vec{p}_{\text{beam}}|^2 + b\,|\vec{p}_{\text{beam}}| + c, \tag{A.10}$$

with

$$a = 4|\vec{p}_X|^2 \cos^2\theta - 4(E_X - m_p)^2, \tag{A.11}$$

$$b = -4|\vec{p}_X| \cos\theta (2m_p E_X - m_{\pi^-}^2 - m_X^2), \tag{A.12}$$

$$c = (2m_p E_X - m_{\pi^-}^2 - m_X^2)^2 - 4\left[m_{\pi^-}(E_X - m_p)\right]^2. \tag{A.13}$$

The positive solution of this quadratic equation is

$$|\vec{p}_{\text{beam}}| = \frac{-b + \sqrt{b^2 - 4ac}}{4a}. \tag{A.14}$$

Inserting this equation into Eq. (A.1) yields E_{beam} from Mandelstam t, the squared four-momentum transfer as defined in Eq. (3.23).

Appendix B

Special Distributions

We discuss different distributions used throughout this thesis. Appendix B.1 explains double-Gaussian distributions. Appendix B.2 discusses the Voigt and the relativistic Voigt distributions and Appendix B.3 discusses the convolution of a double-Gaussian and a Breit-Wigner distribution as an alternative to the Voigt distribution and the convolution of a double-Gaussian and a relativistic Breit-Wigner distribution as an alternative to the relativistic Voigt distribution for the $\omega(782)$ fit in Section 3.6.

B.1 Double-Gaussian Distribution

The double-Gaussian distribution D_{G} is the sum of two Gaussians with the same mean, i.e.

$$\begin{aligned} D_{\mathrm{G}}(x; R_{\mathrm{D}}, \mu_{\mathrm{D}}, \sigma_{1,\mathrm{D}}, \sigma_{2,\mathrm{D}}) = \\ R_{\mathrm{D}}\,\mathcal{N}(x; \mu_{\mathrm{D}}, \sigma_{1,\mathrm{D}}) + (1 - R_{\mathrm{D}})\,\mathcal{N}(x; \mu_{\mathrm{D}}, \sigma_{2,\mathrm{D}}), \end{aligned} \tag{B.1}$$

where R_{D} is the ratio between both Gaussians, μ_{D} is the center and mean of the distribution, and $\sigma_{1/2,\mathrm{D}}$ are the widths of both Gaussians. $\mathcal{N}$ is the normalised Gaussian, i.e.

$$\mathcal{N}(x, \mu, \sigma) = \frac{1}{\sqrt{2\pi}\sigma} \exp\left[-\frac{1}{2} \frac{(x-\mu)^2}{\sigma^2} \right]. \tag{B.2}$$

The total width of D_{G} is estimated as the weighted sum of $\sigma_{1/2,\mathrm{D}}$, i.e.

$$\sigma_{\mathrm{D}} = R_{\mathrm{D}}\sigma_{1,\mathrm{D}} + (1 - R_{\mathrm{D}})\sigma_{2,\mathrm{D}}. \tag{B.3}$$

B.2 Relativistic Voigt Distribution

Particles that have a decay width Γ_0 that is small compared to the mass resolution σ, such as π^0 in COMPASS, its peak in the mass distribution can

be well described by neglecting the decay width, i.e. using only the resolution function. However, this approximation does not work well for the decay of the $\omega(782)$, which has a decay width of $8.68\,\mathrm{MeV}/c^2$ [21] that is similar to the $\pi^-\pi^0\pi^+$ resolution of around $5\,\mathrm{MeV}/c^2$ of COMPASS (see Fig. 5.3). Following Ref. [44], we give a short overview how to describe resonance peaks taking into account both the detector resolution σ and the resonance width Γ_0. In the non-relativistic limit, the peak shape of a resonance is described by a Breit-Wigner distribution, i.e.

$$\frac{dN}{dm}(m; m_0, \Gamma_0^{\mathrm{nr}}) = \frac{\Gamma_0^{\mathrm{nr}}}{2\pi} \frac{1}{(m-m_0)^2 + (\Gamma_0^{\mathrm{nr}})^2/4}, \tag{B.4}$$

where N is the number of events measured at mass m, m_0 is the resonance mass (i.e. the mean of the distribution), and Γ_0^{nr} the full width of the peak at half maximum. For relativistic particles, Eq. (B.4) needs to be modified leading to the relativistic Breit-Wigner distribution

$$\frac{dN}{dm}(m; m_0, \Gamma_0^{\mathrm{rel}}) = \frac{m_0 \Gamma_0^{\mathrm{rel}}}{\pi} \frac{1}{(m^2 - m_0^2)^2 + (m_0 \Gamma_0^{\mathrm{rel}})^2}. \tag{B.5}$$

Here, m is the measured mass, m_0 is the nominal rest mass of the resonance and Γ_0^{rel} is the total decay width, which is related to the mean lifetime of the particle according to $\tau = \hbar/\Gamma_0^{\mathrm{rel}}$. The resolution of the detector is described by the resolution function $G(m; m')$ which describes how the measured value m is distributed for a given true value m'. The detector resolution results in a broadening of the Breit-Wigner distribution that is described by a convolution of the resonance peak shape and the resolution function. In the simplest case we approximate the resolution function by a Gaussian $\mathcal{N}$, i.e.

$$G(m; m', \sigma) = \mathcal{N}(m; m', \sigma), \tag{B.6}$$

where σ describes the width of the Gaussian. We end up with the Voigt distribution

$$V(m; \sigma, m_0, \Gamma_0^{\mathrm{nr}}) = \int_{-\infty}^{\infty} G(m; m', \sigma) \frac{dN}{dm'}(m'; m_0, \Gamma_0^{\mathrm{nr}}) dm' \tag{B.7}$$

for the non-relativistic case and the relativistic Voigt distribution

$$V_{\mathrm{rel}}(m; \sigma, m_0, \Gamma_0^{\mathrm{rel}}) = \int_{-\infty}^{\infty} G(m; m', \sigma) \frac{dN}{dm'}(m'; m_0, \Gamma_0^{\mathrm{rel}}) dm' \tag{B.8}$$

for the relativistic case. To obtain the full width at half maximum Γ_V^{nr} of Eq. (B.7), we use the approximation

$$\Gamma_V^{\mathrm{nr}} \approx 0.5346 \Gamma_G + \sqrt{0.2166 \Gamma_G^2 + (\Gamma_0^{\mathrm{nr}})^2}, \tag{B.9}$$

where Γ_0^{nr} is the full decay width and Γ_G is the full width at half maximum of the Gaussian defined as

$$\Gamma_G = \sigma 2\sqrt{2 \ln 2}, \tag{B.10}$$

where σ is the Gaussian width. For Eq. (B.8) we obtain the full width at half maximum Γ_V^{rel} by numerically finding the two values $m_\pm$ fulfilling

$$V_{\text{rel}}(m_\pm; \sigma, m_0, \Gamma_0^{\text{rel}}) = \frac{1}{2} V_{\text{rel}}(m_0; \sigma, m_0, \Gamma_0^{\text{rel}}) \tag{B.11}$$

and calculating $\Gamma_V^{\text{rel}} = |m_+ - m_-|$. We use Eq. (B.10) to estimate the width σ_V of a Voigt distribution as

$$\sigma_V^{\text{nr/rel}} = \frac{1}{2\sqrt{2\ln 2}} \Gamma_V^{\text{nr/rel}}. \tag{B.12}$$

This does not correspond to the standard deviation of the Voigt distribution.

B.3 $\omega(782)$ Peak with non-Gaussian Resolution

While the decay width Γ_0 in Appendix B.2 is a natural feature of a resonance peak, the Gaussian resolution function is an assumption. For the COMPASS spectrometer simulation favors a double-Gaussian (see Eq. (B.1)) rather than a Gaussian distribution as resolution function for the $\omega(782)$ peak as shown in Section 5.1. We therefore define the distribution $D_{\text{DG}}^{\text{BW}}$ as the convolution of a double-Gaussian and a Breit-Wigner (see Eq. (B.4)) distribution, i.e.

$$\begin{aligned} &D_{\text{DG}}^{\text{BW}}(m; m', R_{\text{DG}}, \sigma_{1,\text{DG}}, \sigma_{2,\text{DG}}, m_0, \Gamma_0^{\text{nr}}) \\ &\quad = \int_{-\infty}^{\infty} D_{\text{G}}(m; R_{\text{DG}}, m', \sigma_{1,\text{DG}}, \sigma_{2,\text{DG}}) \frac{dN}{dm}(m'; m_0, \Gamma_0^{\text{nr}}) dm' \end{aligned} \tag{B.13}$$

and the distribution $D_{\text{DG}}^{\text{BW,rel}}$ as the convolution of a double-Gaussian and a relativistic Breit-Wigner (see Eq. (B.5)) distribution, i.e.

$$\begin{aligned} &D_{\text{DG}}^{\text{BW,rel}}(m; m', R_{\text{DG}}, \sigma_{1,\text{DG}}, \sigma_{2,\text{DG}}, m_0, \Gamma_0^{\text{rel}}) \\ &\quad = \int_{-\infty}^{\infty} D_{\text{G}}(m'; R_{\text{DG}}, m', \sigma_{1,\text{DG}}, \sigma_{2,\text{DG}}) \frac{dN}{dm}(m'; m_0, \Gamma_0^{\text{rel}}) dm'. \end{aligned} \tag{B.14}$$

Appendix C

Study of the Energy-Dependence of π^0 and $\omega(782)$

C.1 Dependence of the π^0 Peak on the $\gamma\gamma$ Energy

Similar to the studies of the time stability of the π^0 peak in Section 3.8.1, also dependence on the energy of the photon pair, from which the π^0 is reconstructed, is studied. If the spectrometer has a uniform response over the full range of the photon energy, we expect a constant π^0 peak position in the $m_{\gamma\gamma}$ spectra for different values of the photon pair energy $E_{\gamma\gamma}$. To this end, we fit the π^0 peak in 1 GeV wide slices in $E_{\gamma\gamma}$. We use the same fit function and the same fit range as in Section 3.8.1. The obtained π^0 masses for all photon-pair cases and both years are shown in Fig. C.1. In all plots m_{π^0} drops significantly below $130\,\mathrm{GeV}/c^2$ for $E_{\gamma\gamma}$ below 10 GeV. Each photon-pair case shows a similar dependence for the data of both years. In the ECAL2 case m_{π^0} is almost constant around $135\,\mathrm{GeV}/c^2$ for energies up to $150\,\mathrm{GeV}/c^2$, while both other photon-pair cases show a significant slope for increasing energies. In principle, a correction for these effects is possible, however the amount of data is not sufficient to do the run-wise post correction described in Section 3.4 and a correction for the energy dependence of the π^0 peak position. Therefore, no correction is applied.

C.2 Dependence of the $\omega(782)$ Peak on the π^0 Energy

To study possible consequences of the observed energy dependence of the π^0 peak position (see Appendix C.1), the $\omega(782)$ peak is fitted in 1 GeV wide slices of the energy of the π^0 assigned as the decay daughter of the $\omega(782)$

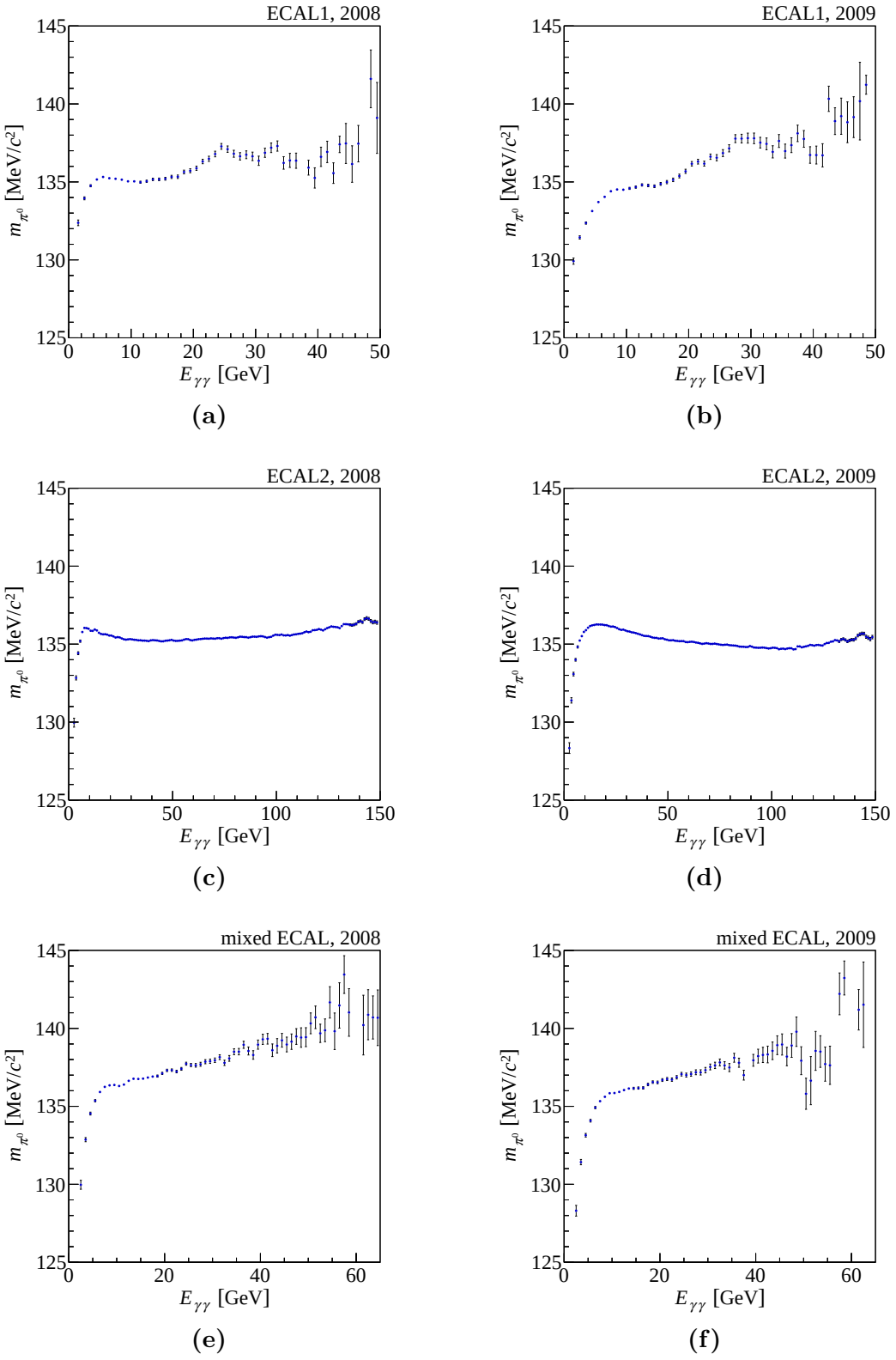

Figure C.1: Fitted π^0 mass as a function of $E_{\gamma\gamma}$. (a) and (b) show ECAL1 photon pairs, (c) and (d) ECAL2 photon pairs, and (e) and (f) mixed ECAL photon pairs. The left column shows the 2008 data, the right one the 2009 data.

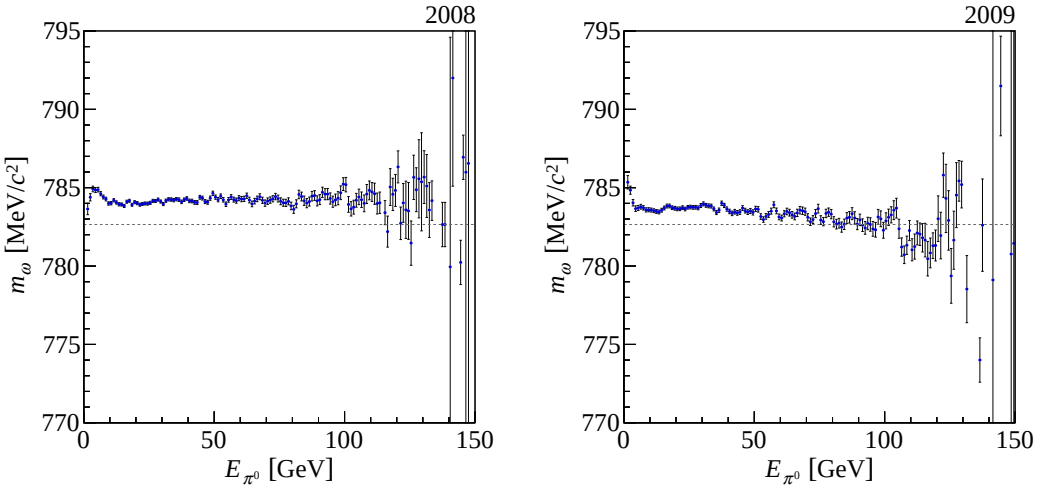

Figure C.2: Fitted $\omega(782)$ mass as a function of the π^0 energy for (a) the 2008 and (b) the 2009 data set.

candidate. The fitting procedure is the same as the one used in Section 3.8.2. The extracted $\omega(782)$ masses are shown as a function of E_{π^0} in Fig. C.2. For the 2008 data m_ω is nearly constant around $784\,\mathrm{GeV}/c^2$, while there is a small decrease of around $2\,\mathrm{MeV}/c^2$ for increasing π^0 energies E_{π^0} for the 2009 data. Both plots show a small increase reaching to $m_\omega = 785\,\mathrm{GeV}/c^2$ at decreasing values of E_{π^0} below 10 GeV. Therefore, the energy-dependence of m_{π^0} has only a minor effect on the fitted $\omega(782)$ mass as a function of E_{π^0}.

Appendix D

Excluded Runs

Table D.1: Excluded runs based on studies of the π^0 and $\omega(782)$ peak parameters discussed in Section 3.8.

Excluded runs		
2008		2009
69 616	70 120	75 884
69 623	70 143	75 888
69 625	70 172	75 911
69 643	70 231	75 939
69 667	70 236	75 940
69 669	70 239	75 949
69 679	70 298	75 976
69 686	70 308	75 990
69 688	70 311	75 997
69 689	70 386	76 218
69 701	70 414	76 235
69 752	70 435	76 338
69 755	70 448	78 632
69 759	70 454	78 921
69 765	70 478	79 064
69 787	70 522	79 104
69 807	70 533	
69 816	70 540	
69 908	70 559	
69 909	70 584	
69 910	70 594	
69 970	70 605	
69 985	70 650	
70 095	70 725	
70 101	70 822	
70 105	70 919	

Bibliography

[1] M. Gell-Mann, "A Schematic Model of Baryons and Mesons," *Phys. Lett.* **8** (1964) 214–215.

[2] G. Zweig, "An SU_3 model for strong interaction symmetry and its breaking," CERN-TH-401, 1964. https://cds.cern.ch/record/352337.

[3] M. E. Peskin and D. V. Schroeder, *An Introduction to Quantum Field Theory*. Addison-Wesley, Reading, 1995.

[4] R. Aaij *et al.*, [LHCb], "Observation of Structure in the J/ψ -Pair Mass Spectrum," *Sci. Bull.* **65** no. 23, (2020) 1983–1993, arXiv:2006.16957 [hep-ex].

[5] K. G. Wilson, "Confinement of Quarks," *Phys. Rev. D* **10** (1974) 2445–2459.

[6] C. Gattringer and C. B. Lang, *Quantum chromodynamics on the lattice*, vol. 788 of *Lect.Notes Phys.* Springer, Berlin, 2010.

[7] S. Weinberg, "Phenomenological Lagrangians," *Physica A* **96** no. 1-2, (1979) 327–340.

[8] V. Barone and E. Predazzi, *High-Energy Particle Diffraction*, vol. 565 of *Texts and Monographs in Physics*. Springer-Verlag, Berlin Heidelberg, 2002.

[9] J. J. Dudek, R. G. Edwards, P. Guo, and C. E. Thomas, [Hadron Spectrum], "Toward the Excited Isoscalar Meson Spectrum from Lattice QCD," *Phys. Rev. D* **88** no. 9, (2013) 094505, arXiv:1309.2608 [hep-lat].

[10] G. M. Beladidze *et al.*, [VES], "Study of $\pi^- N \to \eta\pi^- N$ and $\pi^- N \to \eta'\pi^- N$ Reactions at 37 GeV/c," *Phys. Lett. B* **313** (1993) 276–282.

[11] J. Kuhn *et al.*, [E852], "Exotic Meson Production in the $f_1(1285)\pi^-$ System observed in the Reaction $\pi^- p \to \eta\pi^+\pi^-\pi^- p$ at 18 GeV/c," *Phys. Lett. B* **595** (2004) 109–117, arXiv:hep-ex/0401004.

[12] M. Lu *et al.*, [E852], "Exotic Meson Decay to $\omega\pi^0\pi^-$," *Phys. Rev. Lett.* **94** (2005) 032002, arXiv:hep-ex/0405044.

[13] M. Alekseev *et al.*, [COMPASS], "Observation of a $J^{PC} = 1^{+-}$ Exotic Resonance in Diffractive Dissociation of 190 GeV/c π^- into $\pi^-\pi^-\pi^+$," *Phys. Rev. Lett.* **104** (2010) 241803, arXiv:0910.5842 [hep-ex].

[14] C. Adolph *et al.*, [COMPASS], "Odd and Even Partial Waves of $\eta\pi^-$ and $\eta'\pi^-$ in $\pi^-p \to \eta^{(\prime)}\pi^-p$ at 191 GeV/c," *Phys. Lett. B* **740** (2015) 303–311, arXiv:1408.4286 [hep-ex]. [Erratum: Phys.Lett.B 811, 135913 (2020)].

[15] A. Rodas *et al.*, [JPAC], "Determination of the Pole Position of the Lightest Hybrid Meson Candidate," *Phys. Rev. Lett.* **122** no. 4, (2019) 042002, arXiv:1810.04171 [hep-ph].

[16] A. J. Woss, J. J. Dudek, R. G. Edwards, C. E. Thomas, and D. J. Wilson, [Hadron Spectrum], "Decays of an Exotic 1^{-+} Hybrid Meson Resonance in QCD," *Phys. Rev. D* **103** no. 5, (2021) 054502, arXiv:2009.10034 [hep-lat].

[17] M. Ebert, "Analysis of the $b_1(1235)\pi$ Final State in COMPASS Data," bachelor thesis, Technische Universität München, 2011. https://wwwcompass.cern.ch/compass/publications/theses/2011_bac_ebert.pdf.

[18] C. Dreisbach, *Private Communication.* 2021.

[19] J. Seguinot and T. Ypsilantis, "Photoionization and Cherenkov Ring Imaging," *Nucl. Instrum. Meth.* **142** (1977) 377.

[20] P. Abbon *et al.*, [COMPASS], "The COMPASS Setup for Physics with Hadron Beams," *Nucl. Instrum. Meth. A* **779** (2015) 69–115, arXiv:1410.1797 [physics.ins-det].

[21] P. A. Zyla *et al.*, [Particle Data Group], "Review of Particle Physics," *PTEP* **2020** (2020) 083C01.

[22] A. De Angelis and M. Pimenta, *Introduction to Particle and Astroparticle Physics.* Undergraduate Lecture Notes in Physics. Springer Milan, 2015.

[23] S. Wallner *et al.*, "CEDAR PID using the Likelihood Approach for the Hadron-Beam," *COMPASS note* (2017) . https://wwwcompass.cern.ch/compass/notes/2017-1/2017-1.pdf.

[24] S. Wallner, S. Huber, and C. Dreisbach, "CEDAR Likelihood Helper," 2019. https://gitlab.cern.ch/compass/hadron/cedar-likelihood/-/tree/master/CEDAR_SC.

[25] S. Wallner *et al.*, "Event Selection of the Reaction $K^- + p \to K^-\pi^-\pi^+ + p$: 2008 and 2009 Data Set," *COMPASS release note* (2019) . https://wwwcompass.cern.ch/compass/results/2019/august_Kpipi_Data/Release_note_Kpipi-Data.pdf.

[26] S. Uhl, "Photon Reconstruction and Partial-Wave Analysis of Three-Body Final States with Neutral Particles at COMPASS," PhD thesis, Technische Universität München, 2016. https://wwwcompass.cern.ch/compass/publications/theses/2016_phd_uhl.pdf.

[27] S. Gerassimov, "ECAL π^0 Post-Correction," 2020. https://twiki.cern.ch/twiki/bin/view/Compass/HadronAnalysis/ECALPostCorrection#RefAnchor2.

[28] T. Schlüter, "The $\pi^-\eta$ and $\pi^-\eta'$ Systems in Exclusive 190 GeVπ^-p Reactions at COMPASS (CERN)," PhD thesis, Ludwig-Maximilians-Universität München, 2012. https://wwwcompass.cern.ch/compass/publications/theses/2012_phd_schlueter.pdf.

[29] T. Schlüter, "A Code for Kinematic Fitting with Constraints from Intermediate Particle Masses," *COMPASS note* (2007) . https://wwwcompass.cern.ch/compass/notes/2007-10/2007-10.pdf.

[30] D. Spühlbeck, *Private Communication*. 2021.

[31] G. Cowan, *Statistical Data Analysis*. Oxford science publications. Clarendon Press, 1998.

[32] G. D. Alexeev *et al.*, [COMPASS], "Spin Density Matrix Elements in Exclusive ω Meson Muoproduction," *Eur. Phys. J. C* **81** no. 2, (2021) 126, arXiv:2009.03271 [hep-ex].

[33] K. A. Bicker, "Model Selection for and Partial-Wave Analysis of a Five-Pion Final State at the COMPASS Experiment at CERN," PhD thesis, Technische Universität München, 2016. http://cds.cern.ch/record/2215512.

[34] J. J. Sakurai and J. Napolitano, *Modern Quantum Mechanics*. Cambridge University Press, 2020.

[35] R. H. Dalitz, "On the Analysis of tau-Meson Data and the Nature of the tau-Meson," *Phil. Mag. Ser. 7* **44** (1953) 1068–1080.

[36] M. Jacob and G. C. Wick, "On the General Theory of Collisions for Particles with Spin," *Annals Phys.* **7** (1959) 404–428.

[37] Herndon, D. and Söding, P. and Cashmore, R. J., "A Generalized Isobar Model Formalism," *Phys. Rev. D* **11** (1975) 3165.

[38] K. Gottfried and J. D. Jackson, "On the Connection between Production Mechanism and Decay of Resonances at High-Energies," *Nuovo Cim.* **33** (1964) 309–330.

[39] C. Adolph *et al.*, [COMPASS], "Resonance Production and $\pi\pi$ S-wave in $\pi^- + p \to \pi^-\pi^-\pi^+ + p_{\text{recoil}}$ at 190 GeV/c," *Phys. Rev. D* **95** (2017) 032004, arXiv:1509.00992 [hep-ex].

[40] F. Haas, "Two-Dimensional Partial-Wave Analysis of Exclusive 190 GeV$\pi^- p$ Scattering into the $\pi^-\pi^-\pi^+$ Final State at COMPASS (CERN)," PhD thesis, Technische Universität München, 2013.

[41] I. J. R. Aitchison and R. J. A. Golding, "Relativistic Three Pion Dynamics in the ω Channel," *J. Phys. G* **4** (1978) 43.

[42] F. Niecknig, B. Kubis, and S. P. Schneider, "Dispersive Analysis of $\omega \to 3\pi$ and $\phi \to 3\pi$ Decays," *Eur. Phys. J. C* **72** (2012) 2014, arXiv:1203.2501 [hep-ph].

[43] M. Ablikim *et al.*, [BESIII], "Dalitz Plot Analysis of the Decay $\omega \to \pi^+\pi^-\pi^0$," *Phys. Rev. D* **98** (2018) 112007, arXiv:1811.03817 [hep-ex].

[44] R. A. Kycia and S. Jadach, "Relativistic Voigt Profile for Unstable Particles in High Energy Physics," *J. Math. Anal. Appl.* **463** no. 2, (2018) 1040–1051, arXiv:1711.09304 [math-ph].

Own Contributions

The event selection presented in this thesis is an extension of the work done by Christian Dreisbach. With the help of Boris Grube, I revisited the event selection implemented in the C++ analysis frameworks PHAST and Antok. I improved existing cuts and added further ones, i.e. the CEDAR and RICH vetos based on methods established by Stefan Wallner, and the beam time cut. I extended the event selection to include not only 2008 but also 2009 COMPASS data and verified consistency between both. Based on the statistical significance of the π^0 and the $\omega(782)$ peak I optimised the energy thresholds for both electromagnetic calorimeters. Studies on including an electron veto for final-state particles based on a cut on the ratio of a charged particles energy over momentum proved unsuccessful. By studying the stability of the π^0 and $\omega(782)$ peak I introduced a bad run list for the investigated channel to remove runs with deviating peak parameters.

I performed studies on several subsystems of the $\pi^-\pi^0\omega$ system and the $\pi^-\pi^-\pi^0\pi^0\pi^+$ final-state. Further, I investigated the angular distributions of $\pi^-\pi^0\omega$ and the Dalitz plot of $\omega(782)$. For the later, I introduced a simple sideband subtraction. I implemented the event selection for the simulated $\pi^-\pi^-\pi^0\pi^0\pi^+$ phase-space events and studied the resolutions and acceptances for the simulation.

After providing the $\pi^-\pi^0\omega$ sample and the phase-space acceptances as the two required inputs for a partial-wave analysis, I started extending the ROOTPWA framework to include $\omega(782) \to \pi^-\pi^0\pi^+$ decays. This is the first step towards performing the first partial-wave analysis in the $\pi^-\pi^0\omega$ channel for COMPASS data.

Acknowledgements

First and foremost I want to thank Prof. Stephan Paul for giving me the opportunity to be part of his group and the COMPASS community. Thanks to this opportunity I was able to work on the physics presented in and beyond this thesis.

I am very grateful for the support of Boris Grube. His seemingly endless patience and knowledge improved not only my understanding of physics, but also my skills in writing and programming. He always had time for my questions and the many discussions with him brought up many ideas for my work. Big thanks go to him for his comments and proofreading.

It was a pleasure to be part of the E18 COMPASS group. Suggestions and constructive criticism from the group were helping to improve the analysis. Special thanks go to Stefan Wallner for settling the many disputes between software and me. He was a great help to get the analysis running and also took care of simulating 10^8 MC events. I thank Christian Dreisbach for his previous work and code, which are the foundation of the analysis.

Furthermore, many thanks to all other E18 members for creating a friendly and productive environment. I enjoyed the time there very much. I am also very grateful to Karin Frank for her great support in getting paperwork done.

Many thanks to the COMPASS collaboration. Suggestions from the hadron subgroup were meaningful feedback. I want to thank Lukas Bayer for the discussions concerning the event selection.

Zu guter Letzt möchte ich meinen Eltern Alfred und Maria, sowie meinen beiden Brüdern Christian und Simon danken. Auf ihre Unterstützung war stets Verlass und sie boten mir immer ein chaotisches, aber herzliches Zuhause, wenn ich es brauchte.